Large Amplitude Lee Waves and Chinook Winds
Report No. 4

By
Donald W. Beran

E.R. Reiter, Project Director
Grant WBG-59

Under Contract with Department of Commerce U.S. Weather Bureau

Technical Paper No. 75
Department of Atmospheric Science
Colorado State University
Fort Collins, Colorado

March 1966

Colorado State University

Department of Atmospheric Science

Paper No. 75

LARGE AMPLITUDE LEE WAVES AND CHINOOK WINDS

by
Donald W. Beran

WISP Report No. 4
Grant WBG-59
With United States Department of Commerce
Environmental Sciences Service Administration
National Environmental Satellite Center

Project Leader: Elmar R. Reiter
Professor, Department of Atmospheric Science
Colorado State University
Fort Collins, Colorado

Atmospheric Science Technical Paper No. 75

March 1966

ABSTRACT

Four types of chinooks are described: (1) warming of parcel due to subsidence, (2) warming due to latent heat gain on windward side of mountains, (3) wave action at interface of cold surface air and warmer air aloft, and (4) nocturnal chinooks.

The suggestion made by Scorer and Klieforth (1959) that large amplitude lee waves could be a possible driving mechanism for chinook or foehn winds is investigated for two cases which occurred in the Rocky Mountains. It is shown that there is a relation between the stability of the surface inversion layer on the windward side of the mountains, and the area under the influence of chinook winds on the leeward side.

Flow patterns at 250 mb and 700 mb were analyzed along with the moisture flux at 700 mb. The analyses of wind field, mass divergence, vorticity, and divergence of moisture were compared with TIROS photographs over the mountains.

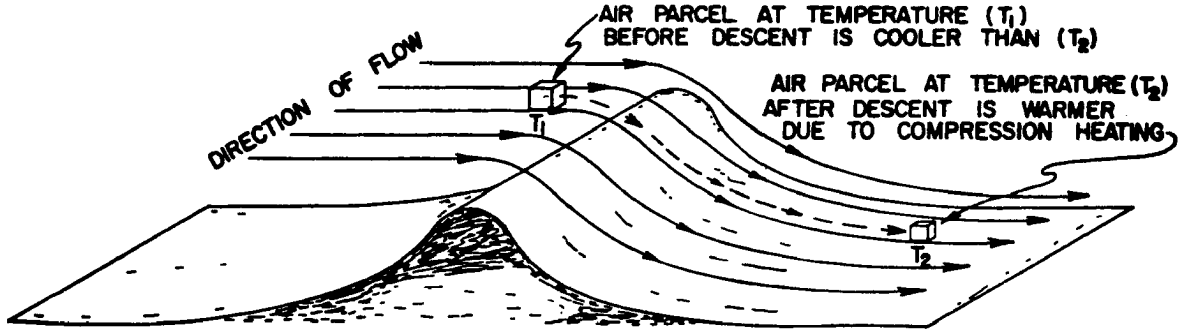

Figure 1. Cross section through ridge showing descent of air parcel on leeward side. Temperature of air parcel at T_2 is greater than temperature of air parcel at T_1 due to compression heating caused by the descent.

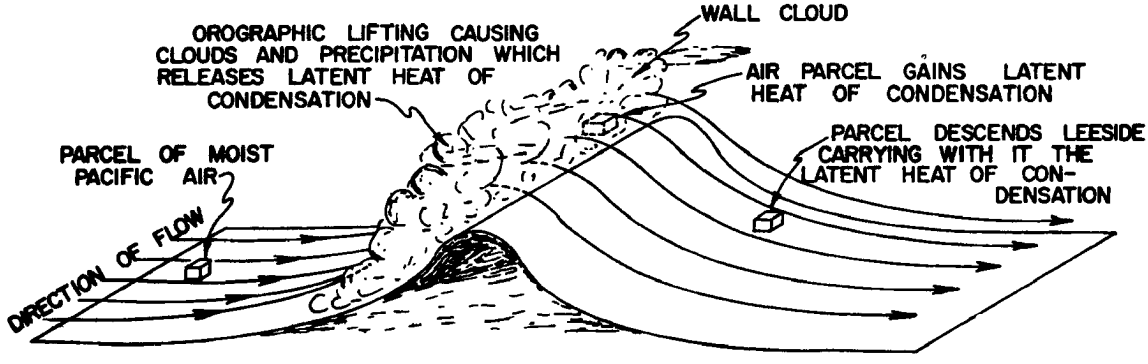

Figure 2. Cross section through ridge showing moist Pacific air being lifted on windward side. This lifting causes condensation and the release of latent heat. The air parcel then descends the leeward side and heat gained from the condensation process is realized as warming at stations on the leeward slope.

ACKNOWLEDGEMENTS

The author is especially grateful to Dr. Elmar R. Reiter for his patient guidance and counsel during the preparation of this report. He also wishes to give special thanks to Mrs. Sandra Olson who typed the manuscript, to Mr. James White who drafted the diagrams, and to Mr. and Mrs. Don Davidson who helped in data preparation.

This research was conducted under U. S. Weather Bureau Grant WBG-59. The data used for analysis was made available by the National Weather Records Center in Asheville, North Carolina.

TABLE OF CONTENTS

LIST OF TABLES

LIST OF ILLUSTRATIONS

LIST OF ILLUSTRATIONS CONTINUED

CHAPTER I

INTRODUCTION

In a previous study of mountain effects on atmospheric flow patterns, as seen from meteorological satellites (Reiter, 1965 a), it was realized that many types of flow and associated cloud patterns could not be fully explained with present knowledge. To gain a better understanding of the patterns identified on the TIROS pictures, separate and more detailed investigations of individual phenomena were undertaken.

Purpose

The primary purpose of this study was to examine the dynamics of chinook winds. A secondary objective was to determine the usefulness of meteorological satellite pictures in research of this type.

Review of Literature

Chinook, a name borrowed by narrators of folklore from an Oregon Indian tribe, is an unusually strong, warm westerly wind which descends the eastern slope of the Rocky Mountains (Cook and Topil, 1952; Glenn, 1961). The chinook is the North American counterpart of Europe's foehn which has received attention from many Europen meteorologists. The general nature of the two winds is similar, the main differences probably being due to orientation of the controlling mountain ranges and size of the area effected.

The major chinook region in western North America extends along a strip two to three hundred miles wide from Alberta, Canada, southward to northeastern New Mexico. This chinook belt follows

the Continental Divide and affects the high plains region along the eastern side of the Rocky Mountains (Glenn, 1961).

European scientists gave the first tenable thermodynamic explanation of the warm, downslope foehn winds which occur in the Alps. In 1866 the now classic thermodynamic foehn principle was proposed by Hann (1903), when he stated that air traversing a mountain range precipitates moisture and gains the latent heat of condensation while ascending the windward slopes; subsequent descent of the air along the leeward slopes takes place dry-adiabatically and the air arrives at lower altitudes dryer and warmer than it was at corresponding elevations during the ascent. Hann later concluded that it was actually unnecessary to postulate ascent with precipitation on the windward slopes since replacement of air on the leeward slopes, having the usual wintertime lapse rate, by descending air warming at the dry-adiabatic rate, could account for the observed temperature rises.

Subsequent investigations (Cook and Topil, 1952; McClain, 1952; Glenn, 1957; Burman, 1958; and Gutmann and Tebuev, 1961) have led to a good understanding of the important processes occurring during a chinook. These processes, acting either alone or together, have been subdivided into four types by Glenn (1961).

The first type occurs when air is brought from higher to lower levels in the atmosphere. The lowering of an air parcel causes it to be warmed by compression at the dry-adiabatic lapse rate. Figure 1 shows a schematic representation of this process.

The second process (see Figure 2), which is important during and before a chinook, is the original concept envisioned by Hann in 1866. If moisture is condensed and removed from Pacific air as it is lifted up the western slope of the Rocky Mountains, latent heat of condensation will be added to the air mass. The heat gained by this process will be realized as warming at leeward stations when the air descends the eastern slope.

The third type, which explains the spectacular temperature rises often associated with a chinook, will occur if a cold shallow mass of polar or arctic air is lying against the eastern slope of the Rockies. With the cold air mass in this position, perturbations might form on the interface between the cold surface air and the warmer air aloft (see Figure 3). If one thinks of the top of the cold air mass as the surface of a lake and a leeward station as a point on the shore near the water line, it is clear that when waves intersect the shore line, the point near the water surface will be periodically submerged. An analogous situation exists when the perturbations (waves) form on the interface of warm and cold air, that is, the leeward station is periodically submerged in the cold air causing drastic temperature changes in short periods of time.

Glenn (1961) described an extreme case of this type of "chinook" which occurred near the Black Hills of South Dakota in mid-January of 1943.

> On 15 January 1943, an outbreak of extremely cold arctic air moved into the Great Plains, covering the Black Hills area and producing in many places record low temperatures. Starting on January 20th, the cold air became shallow enough that some of the mining towns at the higher elevations in the Black Hills began breaking through into much warmer air. During the day of January 20th, warming occurred at all points above 4500 feet, and during the next two days, warm air aloft scoured out another thousand feet of cold air, at least in the southern hills, but left places below 3500 feet still in the grip of some of the coldest weather on record. The change in temperature was really extreme, ranging from readings below zero in the cold air to as high as +60° F in the warm air. On January 22nd some minor pressure disturbances moving through the area caused the cold air to undulate up and down like waves against a wharf after a speedboat passes. The phenomenon was first noted at Spearfish, South Dakota, at 0732 when the mercury skyrocketed from -4° to 45° F within a period of only two minutes. This was only the beginning of a series of sharp dips and rises that continued for an hour or two.

Eventually a low will move over the mountains from the west or will form on the leeward side due to conservation of potential vorticity in the westerly air stream. This low pressure system will help remove the cold air from the eastern slope of the Rocky Mountains and bring warmer air to the stations which have been under the influence of the arctic air mass.

The fourth factor outlined by Glenn (1961) involves the nocturnal warming associated with many chinooks. A nocturnal chinook will prevent radiation cooling at the surface, due to mixing and advection at lower levels, thus causing an apparent warming. Figure 4 shows schematically how the advection of warmer air and low level turbulence could prevent normal nocturnal cooling.

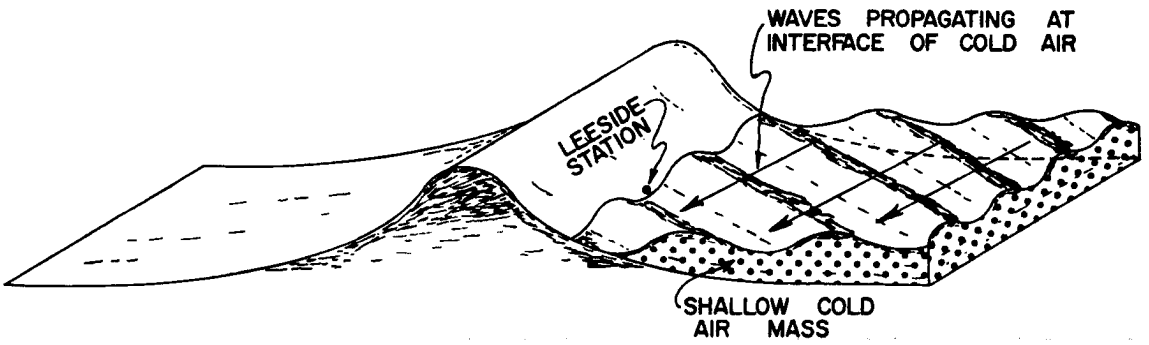

Figure 3. Cross section through ridge with cold arctic or polar air banked against the side of the ridge. Waves are shown forming at top of cold air and periodically submerging stations located near the interface of cold and warm air. This action has been known to cause drastic temperature changes at leeside stations.

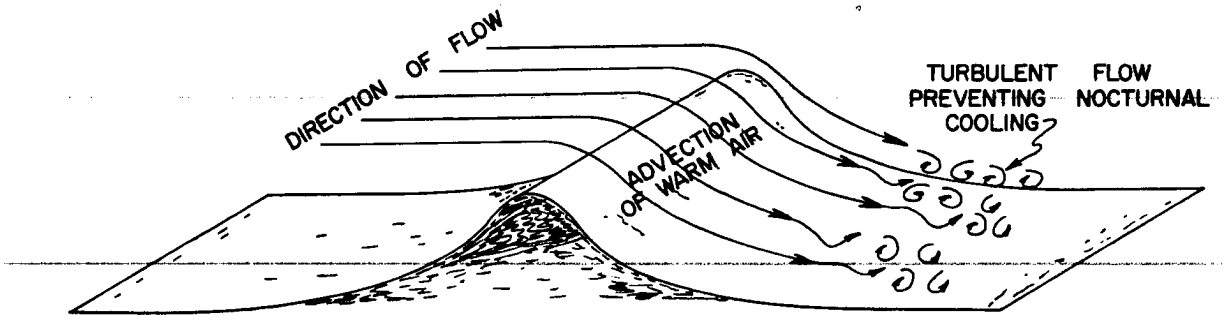

Figure 4. Cross section through ridge showing advection of warm air and turbulence to the leeward side. When this process acts during nighttime, it prevents normal radiation cooling of the surface layer and leeward stations stay relatively warm.

CHAPTER II

THEORETICAL DEVELOPMENT

Most investigators of the chinook have been content to deal with its thermodynamic structure and its effect, giving only passing mention to possible driving mechanisms. Recent theoretical studies have suggested that large amplitude lee waves could be responsible for the generation of chinook winds (Queney, 1947; Scorer and Klieforth, 1959).

Following the theoretical development of Scorer and Klieforth, it is possible to show a connection between the theory of large amplitude lee waves and chinook winds.

The following symbols will be used in this development:

c = velocity of sound

g = gravity (0, 0, g)

k = wave number

ℓ^2 = Scorer's parameter $= \frac{g\beta}{U^2} - \frac{1}{U}\frac{\partial^2 U}{\partial z^2}$. Last term is usually neglected when shear is small.

U, V = horizontal velocity components in undisturbed stream, U is normal and V is parallel to ridge.

x, y, z = Cartesian coordinates, x is along streamline, y is normal to streamline, and z is vertical.

β = Static stability $= \frac{1}{\theta}\frac{\partial \theta}{\partial z}$

$\epsilon = \frac{g\zeta}{c^2}$ is a non-dimensional parameter representing particle displacement with $\zeta = z - z_o$. Scorer used this parameter because it incorporated the elasticity of the atmosphere through c, the speed of sound.

ζ = vertical displacement of a particle from its original level = $(z - z_o) = Z + \int \frac{d\psi}{U}$, U being a function of ψ only.

θ = potential temperature

ψ is defined by $\frac{\partial \psi}{\partial z_o} = -U$

prime denotes $\frac{\partial}{\partial z_o}$ where z_o is level from which the particle at a point originated.

Scorer (1955) proved that, provided the displacement of a particle from its original level was such that

$$\epsilon \ll 1 , \tag{1}$$

the displacement ζ in two-dimensional motion in the x-z plane satisfies

$$\nabla^2 \zeta + \left[\frac{\beta_o}{2} + \frac{g}{c^2} - \frac{U'}{U}\right] (\nabla \zeta)^2 + \left[\frac{2U'}{U} - \beta_o - \frac{g}{c^2}\right] \frac{\partial \zeta}{\partial z} + \frac{g\beta_o}{U^2} \zeta = 0 . \tag{2}$$

If $\epsilon \ll 1$, it follows that $\zeta = z - z_o$ must also be very small; that is, only waves with very small vertical displacement are considered.

Since β_o and U, the static stability and wind speed in the stream when undisturbed, are constant along a streamline, they are functions of x and z which depend upon ζ . If β_o and U are functions of z, and ζ is a function of z, the equation is nonlinear in all terms except the first. However, if β_o and U are independent of z, the equation will only be nonlinear in the second term. By choosing special cases in which the equation could be linearized, Scorer and Klieforth were able to find solutions to equation (2) which described some interesting properties of waves.

In the simplest case considered the lee waves were periodic in the horizontal direction with wave length $\frac{2\pi}{k}$. In general, solutions of equation (2) cannot be periodic in x unless the equation

is linear in ζ . This means that if a term is not negligible, its coefficient must be independent of z . To linearize the equation Scorer and Klieforth selected a model airstream composed of layers in each of which

$$\frac{g\beta_o}{U^2} = \ell^2 = \text{constant}$$

$$\frac{U'}{U} = S = \text{constant}$$

and either (i) $\frac{U'}{U} >> \frac{g}{c^2}$, β

or (ii) the $\frac{\partial \zeta}{\partial z}$ term is negligible.

The latter conditions imply that if (i) holds, the coefficient of $\frac{\partial \zeta}{\partial z}$ can be regarded as independent of z because its major component $\frac{U'}{U}$ is constant and independent of z . If (i) does not hold, then in order to make equation (2) linear, the $\frac{\partial \zeta}{\partial z}$ term must be negligible in comparison with the other terms. This is true if $U' = 0$ and β_o and g/c^2 are negligible. Scorer (1955) showed that $\beta \simeq 2 \times 10^{-7} \text{cm}^{-1}$ and $g/c^2 \simeq 10^{-6} \text{cm}^{-1}$ and are, therefore, negligible in comparison to the other term.

If the proper conditions are selected, the nonlinear term $(\nabla \zeta)^2$ can be made negligible. This can be accomplished either by assuming the $\frac{\partial \zeta}{\partial z}$ term to be so small that it dominates the $(\nabla \zeta)^2$ term, or by assuming the coefficient of $(\nabla \zeta)^2$ to be negligible.

To achieve this Scorer and Klieforth selected a case where $\frac{\partial \zeta}{\partial z}$ is comparable with unity only in the regions where $U' = 0$. The terms in β_o and g/c^2 were again neglected. Under these conditions, the equation becomes

$$\frac{\partial^2 \zeta}{\partial z^2} + 2S \frac{\partial \zeta}{\partial z} + (\ell^2 - k^2)\zeta = 0 . \qquad (3)$$

For $U' = 0$ the second term will vanish and equation (3) reduces to

$$\frac{\partial^2 \zeta}{\partial z^2} + (\ell^2 - k^2) = 0 \ . \qquad (4)$$

If the mountain shape is given by $\zeta = \zeta_1(x)$ at $z = 0$, the airstream will have a value of ℓ independent of height and Scorer and Klieforth's solution is

$$\zeta = \zeta_1(x) \cos \ell z + \text{lee waves} \qquad (5)$$

where the "lee waves" term represents second order terms. In a uniform airstream without lee waves, the general solution would be

$$\zeta = \zeta_1(x) \cos \ell z + f(x) \sin \ell z \qquad (6)$$

where $f(x)$ is either 0 or $f(x) = \zeta_1(x)$ where ζ_1 is a function derived from ζ_1 by the application of a boundary condition.

With any of the solutions of equation (6) there are values of z which will make $\zeta = 0$. A nodal surface is defined as $\zeta = 0$ and if the mountain is higher than this nodal surface, theoretically, flow cannot occur. With solutions to equation (5) the maximum vertical distance between successive nodal surfaces is π/ℓ; therefore, flow will be impossible if the height of the mountain is greater than π/ℓ. In other words, the stability of the windward inversion can reach a critical value which will cause a ridge to block this flow.

Long (1955) conducted experiments in a closed channel with layers of fluids having different densities. He obtained the density gradients by first putting a layer of fresh water in the channel, then a layer of salt water was inserted at the bottom. Initially a very sharp discontinuity of density existed in the interior. This was destroyed by repeated motions of an abstacle along the bottom. An intermediate situation involving a general gradient interrupted by one

or more inversions, near discontinuities, was produced. This corresponded to a common situation in the real atmosphere where temperature inversions occur. When Long confronted the stream in his model experiment with an "impossible" or "nearly impossible" obstacle (mountain), he noted some interesting consequences. The stream over the "mountain" could be modified by the passage of a wave (front) upstream from the obstacle. This wave passage affected the density gradient in such a way as to increase the value of ℓ . An analogous situation occurs in the real atmosphere when a synoptic scale pressure wave passes over a low level inversion layer to the windward side of the mountain; the magnitude of π/ℓ (inversely proportional to the stability) could be reduced to a value at which the mountain heights downstream would become effective in producing large amplitude lee waves. Another feature in Long's experiment occurred when the lower layers were blocked by the obstacle and the upper layers descended to the surface on the leeward side. This situation may also occur in the real atmosphere if a low level inversion to the windward side of the mountains is blocked and the upper layers then descend to the ground on the leeside.

Scorer and Klieforth speculate that in the real atmosphere this same sequence of events could lead to a chinook or foehn wind. They state: "The obvious suggestion is that foehn (chinook) winds will occur if an airstream reaches a mountain, say on the arrival of a cold front, whose height exceeds π/ℓ ."

This hypothesis is directly applicable to the subsidence (first type mentioned earlier) chinook. Convective activity associated with the second type of foehn would destroy the windward surface inversion, and therefore, $\ell \to 0$. This would cause π/ℓ to be much greater than any mountain height. The wave formation at the cold air interface leading to quasi-periodic submersion of a station requires the action of vertical wind shears across the leeside inversion

and has nothing to do with Scorer and Klieforth's hypothesis. The inhibiting of nocturnal cooling by low level mixing, characteristic of the fourth type of chinook, might be explained by this model because strong chinook winds are required to feed the turbulent motion throughout the night.

Scorer's hypothesis was checked by Lockwood (1962) in a study of foehn winds over the British Isles. The model used in Lockwood's study was similar to that shown in Figure 5. His observations confirmed that the winds had two main driving forces conforming to those suggested by Scorer and Klieforth. These were: leeward subsidence caused by blocking action of the mountains on lower layers of the airstream, and magnification of the downslope motion by large amplitude lee waves forming in the low level inversion layer. By calculating Scorer's parameter for radiosonde ascents near the area of foehn winds and, when possible, upwind of the mountains, Lockwood found in each of six cases studied that values of π/ℓ were approximately equal to, or slightly greater than, the height of generating mountains. The wind speed throughout approximately the first 3,000 meters was at least 7.5 mps. Maximum temperatures on the leeward side of the mountain were usually about equal to the potential temperature near the top of the stable surface layer on the windward side. It is interesting to note that in a study of Montana chinooks McClain (1952) observed that quite stable air was present in the lower troposphere west of the Rockies, particularly in the lowest 1500 meters or so, and that winds in the same layer had components normal to the mountain ranges of less than 15 mps. In order to obtain values of π/ℓ which will be approximately equal to the height of an obstructing mountain, a very stable layer with fairly light winds has to be present. McClain's observations during the Montana chinook appear to meet the above criteria. This assumption has not been checked for McClain's study. It does seem, however, that Scorer and Klieforth's (1959) conditions are met.

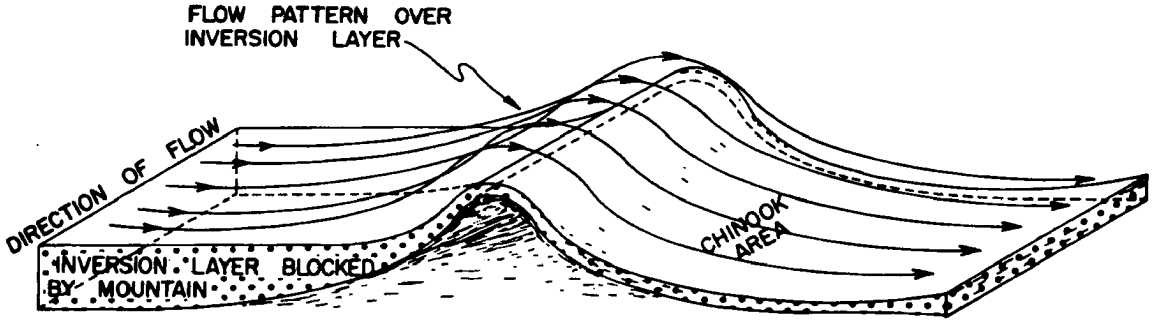

Figure 5. Cross section through ridge showing blocking action on lower inversion layer to the windward side and the subsidence of the air to the leeward side.

CHAPTER III

SELECTION OF CASE STUDIES

Two cases were selected for the purpose of testing Scorer and Klieforth's hypothesis that large amplitude lee waves could be responsible for driving chinook winds. The periods both contained well documented chinook occurrences to the lee of the Rocky Mountains. Mid-April 1963 was selected for the first period on the basis of wall cloud formations appearing on a TIROS photograph (see Figure 6) of northern Colorado. Later analysis (Reiter, 1965 a) confirmed that chinook winds occurred periodically from 14 April to 19 April 1963.

Very intense chinooks in December 1964 led to the choice of the period 12 through 17 December 1964 as the second case. The intensity of the chinook winds and the associated dust storms during this period completely disrupted highway travel in northern Colorado.

Synoptic Pattern for April Case

The surface pattern over the western United States was dominated by a disturbance which moved in from the Pacific Ocean on 13 April 1963. The storm system crossed the plateau region on 14 April and by 15 April the associated cold front was over the Rocky Mountains (see Figures 7 a and 7 b). Between 0600 GMT, 15 April and 0600 GMT, 16 April (see Figures 7 b and 7 c), the front moved rapidly away from the Rocky Mountains and into a position over the Midwest. After this rapid movement, the system consolidated into an intense low on the North Dakota-Manitoba border with a central pressure of 978 mb. This low center then moved in a northeastward direction toward Hudson Bay leaving a nearly stationary front

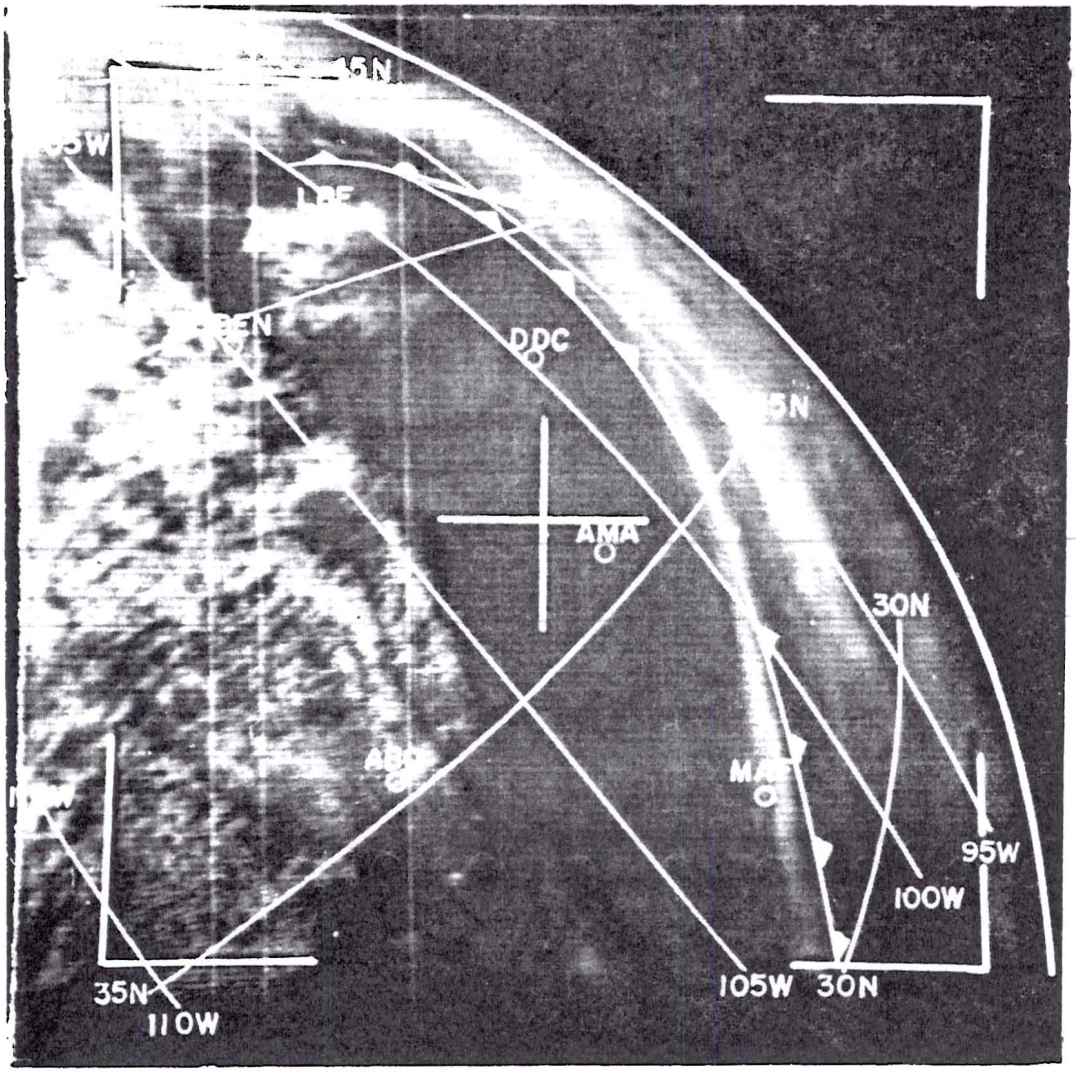

Figure 6. Cloud photograph, TIROS V orbit 4349 (tape) frame 14, 18 April, 1963, 1955 GMT, showing cloud formations over Rocky Mountains. (DEN = Denver, Colorado; LBF = North Platte, Nebraska; DDC = Dodge City, Kansas; AMA = Amarillo, Texas; ABQ = Albuquerque, New Mexico; MAF = Midland, Texas) Line of clouds north of Denver along 105° W longitude is chinook wall cloud forming on Continental Divide.

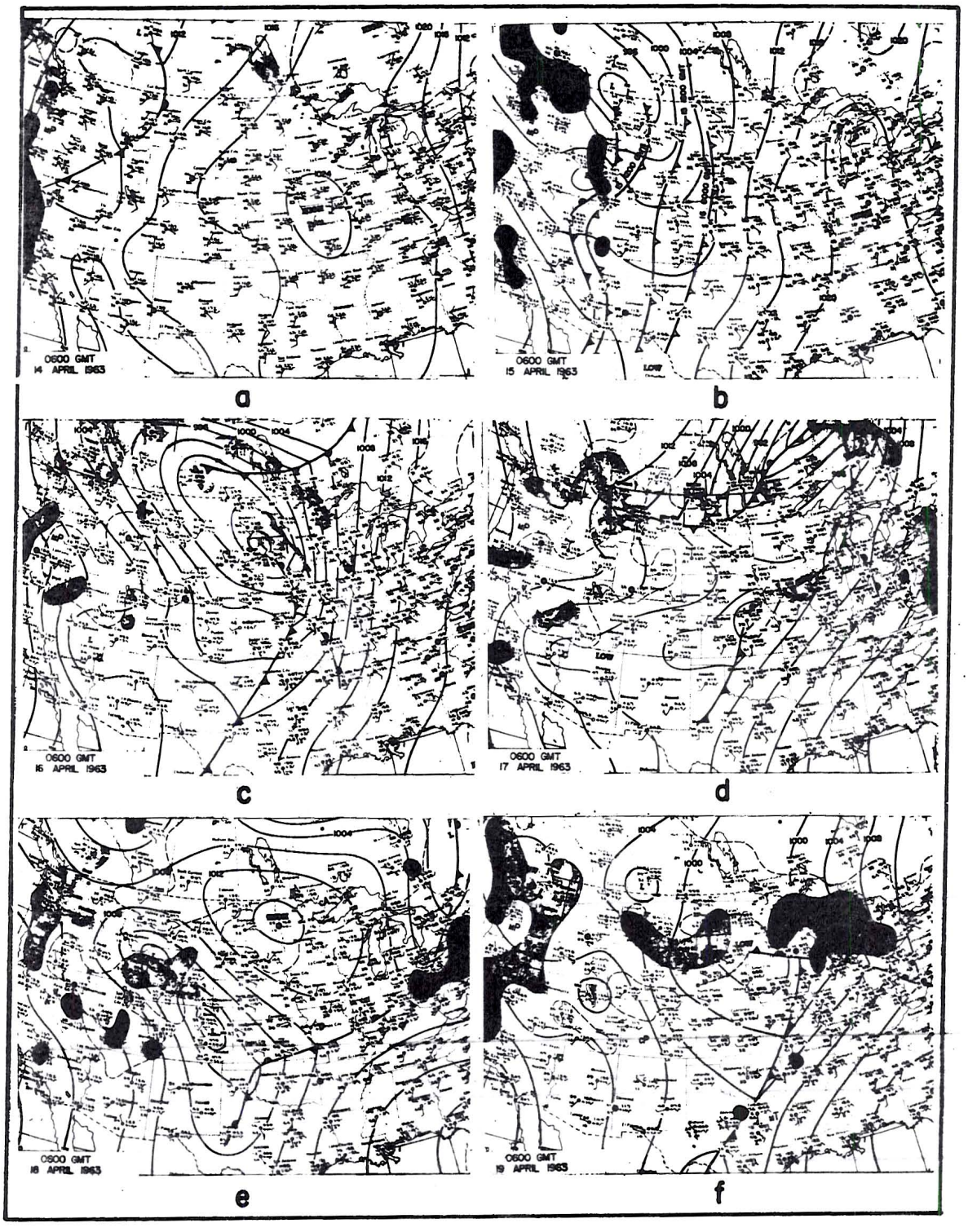

Figure 7. Surface maps for times shown. Solid lines represent isobars (mb), areas with precipitation are shaded. Frontal positions are valid at map time except on chart "b" where the frontal positions for six-hour intervals following the map time are also shown. (Reproduced from U.S. Weather Bureau daily weather map series)

over the central United States. Pressure falls along the leeside of the Rocky Mountains occurred along with a frontal wave development on 18 April (see Figure 7 e), and by 19 April (see Figure 7 f) this frontal wave had deepened and moved northeastward to the Dakotas.

The 500 mb pattern during the April case is shown in Figure 8. On 14 and 15 April (see Figures 8 a and 8 b) the pattern was dominated by a strong ridge over the eastern part of the Rockies. On 16 April (see Figure 8 c) a strongly baroclinic trough, associated with the surface storm, crossed the Rocky Mountains and a small low developed over eastern Wyoming. This depression was probably associated with the surface frontal wave mentioned above. By 17 April (see Figure 8 d) the low pressure system had elongated and extended from northern California to Hudson Bay. South of this low the 500 mb flow pattern was dominated by a strong jet stream from southern California to the Great Lakes region. For the remainder of the period (see Figures 8 e and 8 f), this very strong southwesterly current remained over the Rocky Mountains between Wyoming and New Mexico.

The effect of the synoptic scale pattern on a leeside station is shown in Figure 9 by the time section for Denver, Colorado, from 14 April 1963 to 19 April 1963. Periods of possible chinook conditions are shown in this diagram by horizontal arrows between the dry bulb temperature and the dew point temperature lines. It is realized that there is some ambiguity in chinook definitions. European meteorologists have considered this problem and defined three intensities of foehns (Reiter, 1958). They are: "0", indicating a condition called "foehnig" which is characterized by no appreciable downslope winds measured at the surface, visibility exceeding 50 miles, and unseasonably warm temperatures with large dew point spread. Stage "1" describing a "light foehn" appears as light, intermittent downslope wind measured at surface with additional criteria

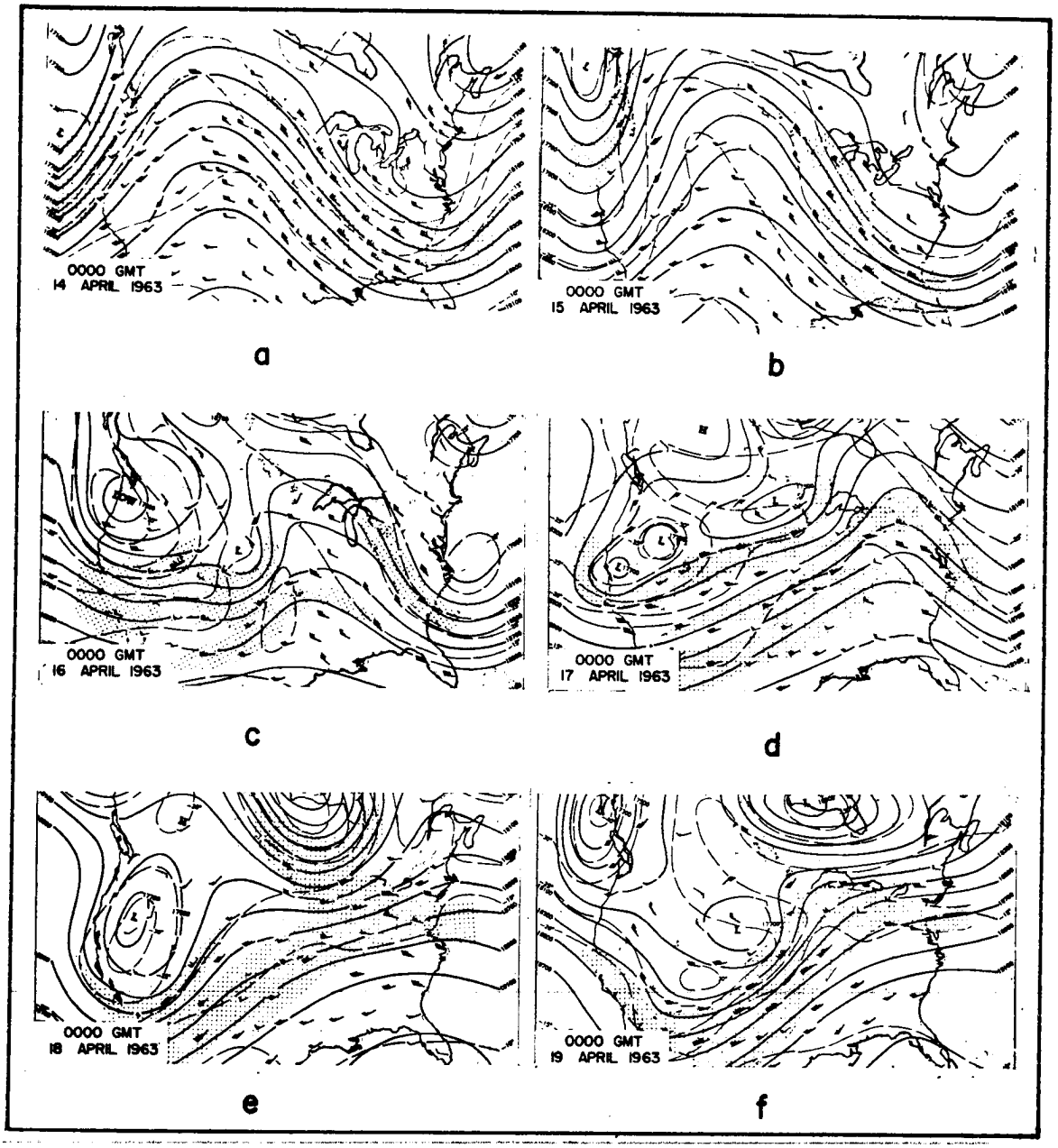

Figure 8. 500-mb height contours (solid lines, ft) for times shown. Dashed lines are isotherms (°C). Arrows show wind direction and speed. Shaded portions denote wind speeds greater than 50 knots. (Reproduced from U.S. Weather Bureau daily weather map series)

as above. Stage "2" representing a "strong foehn" calls for strong, gusty winds blowing for several hours with other phenomena as shown above. In statistical studies on foehn frequency, only foehn stages "1" and "2" are counted. Unfortunately, no such classification exists for the Rocky Mountain region.

The first chinook shown in Figure 9, probably of intensity "0", occurred at about 1800 GMT, 14 April. It was considered as such, despite the light and variable wind, because of the greater-than-normal temperature rise and the sharp drop in dew point temperature. A much more pronounced chinook occurred between 1500 GMT, 15 April and 1400 GMT, 16 April. On these days the wind shifted to a westerly direction, and its speed increased sharply as the dew point temperature dropped. It was during this period that the surface front, as analyzed by the U. S. Weather Bureau, passed Denver, Colorado (see Figure 7 b). The chinook conditions, which caused a marked trough to the lee of the mountains, and the flat temperature field made it very difficult to locate the frontal position accurately. Therefore, it was necessary to rely on the thermal structure aloft to interpolate the frontal motion. Examination of the surface charts (see Figure 7 b) shows the front passing Denver at approximately 2100 GMT, 15 April. However, from the time section shown in Figure 9 this passage is not immediately apparent. The chinook conditions effectively masked the passage of the weak Pacific front. Lower temperatures on the following days do, however, indicate that there was an air mass change associated with the frontal passage.

Following the strong chinook of 15 April, there was a slight depression of the dew point temperature with no marked increase of dry bulb temperature and light variable winds. This period was included in the study as a possible case of chinook with intensity "0".

The next well-pronounced foehn did not occur until 0800 GMT, 18 April (see Figure 9). The records of surface wind speed, wind direction, and dew point temperature fulfill the criteria of a chinook listed above. The weaker rise in surface temperature is probably due to the cold frontal passage and associated air mass change mentioned earlier.

The last chinook of the period under consideration occurred at 2000 GMT, 19 April, and was almost as weak as the chinook of "0" intensity on 16 April. However, it does have slightly stronger west winds, together with a sharp drop in dew point temperature.

An interesting feature of the chinooks shown on the Denver time section is their quasi-periodic occurrence. They were experienced daily with the exception of the 17th. This seems to imply diurnal control of their onset and cessation. More will be said about this possible diurnal control and about the lack of a chinook on 17 April later in this paper.

It was mentioned earlier that the occurrence of the strongest chinook coincided with the cold front passage. This fact lends support to Scorer and Klieforth's suggestion that if the proper values of π/ℓ are found to the windward side of the mountains, a chinook wind should occur with the approach of a cold front. The relation between the height of the mountain and the π/ℓ criteria will also be established later.

Synoptic Pattern for December Case

The dominant and most important feature on the surface maps between 11 December 1964 and 17 December 1964 was an intense high pressure cell which formed over the Great Basin. The sequence of events during this period are shown in Figure 10.

At the beginning of the period, there was a low center over the Montana-Canada border with an occlusion and cold front extending

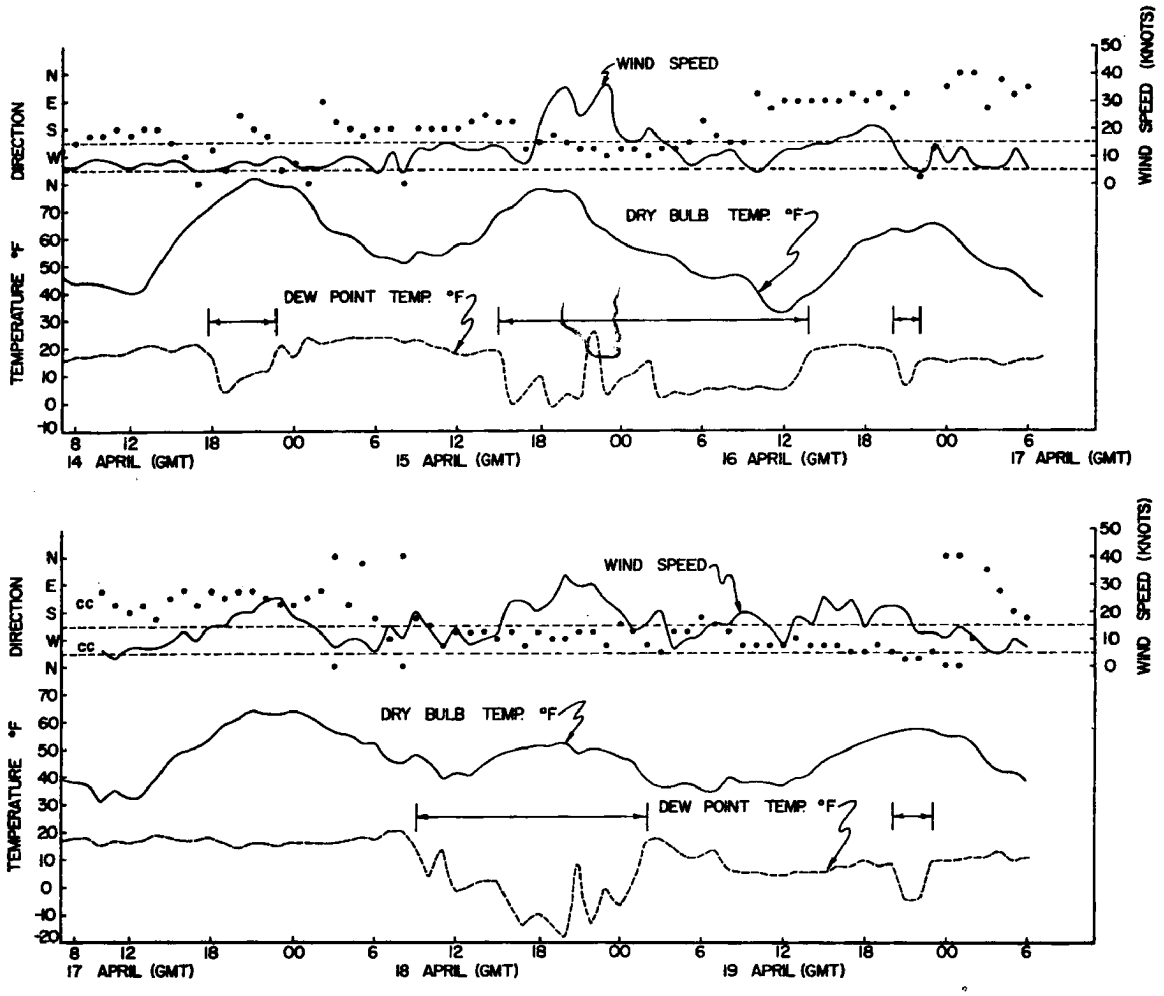

Figure 9. Time section of hourly surface observations at Denver, Colorado, from 14 April 1963 to 19 April 1963. Upper solid line is surface wind speed (knots), lower solid line is dry bulb temperature (°F). Dashed line is dew point temperature (°F) and dots indicate wind direction. All dots between the two horizontal lines are for winds having a predominately westerly component. Periods when suspected chinooks occurred are shown by the brackets between the dry bulb temperature curve and the dew point temperature curve.

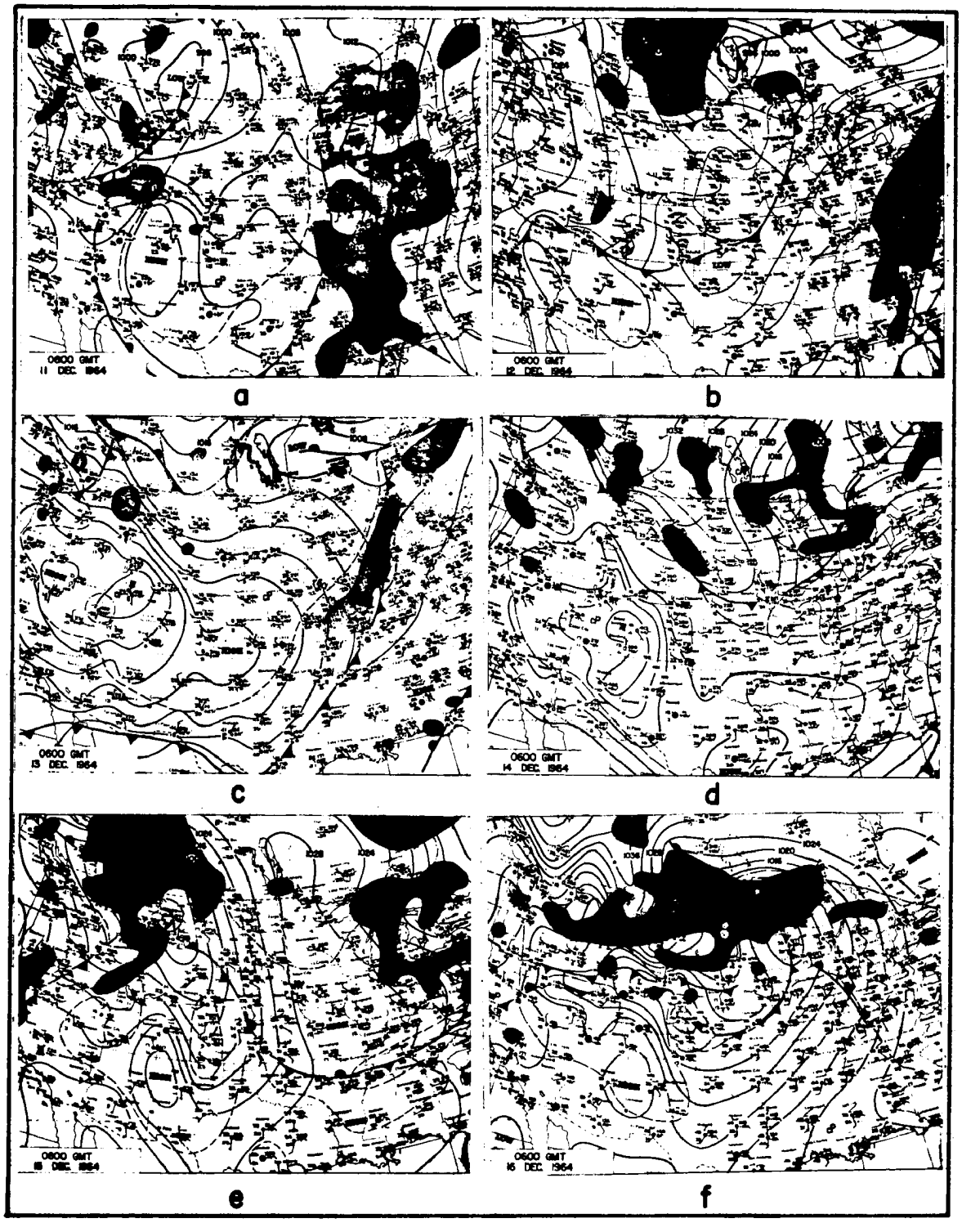

Figure 10. Surface maps for times shown. Solid lines represent isobars (mb), areas with precipitation are shaded. Frontal positions are valid at map time. (Reproduced from U.S. Weather Bureau daily weather map series)

to northern California (see Figure 10 a). By 12 December (see Figure 10 b) this depression had moved eastward and the associated frontal system progressed to a position along the southern border of Utah and Colorado, and then northward to the Great Lakes region. As the cold front continued its southward progress, a high developed over the Great Basin. By 0600 GMT, 13 December this anticyclone carried a closed 1040 mb isobar. Figure 10 c shows this high cell over Salt Lake City and smaller storm systems moving to the north of the high pressure area. The juxtaposition of these lows and the Great Basin high caused the strong pressure gradient which extends from Alberta, Canada, to central Colorado. This pressure gradient is reflected in the very intense surface winds which were blowing along the leeside of the Rockies. A fictitious pressure gradient will sometimes result when surface pressure at mountain stations is reduced to sea level. The high wind speeds mentioned above show that most of this gradient was real.

By 0600 GMT, 14 December (see Figure 10 d) the Great Basin high center had moved southwestward to a position over Grand Junction, Colorado, and the arctic cold front had moved into Montana. The intense pressure gradient and strong leeside winds over the Rocky Mountains were still in evidence. This general pattern maintained itself until 16 December when the high pressure cell had weakened and allowed the arctic cold front to progress slowly southward, ending the chinook conditions in Montana, Wyoming, and Colorado.

In the early part of the period the 500 mb flow pattern was marked by an unusually sharp trough over the central United States (see Figure 11 a). As this trough moved eastward, it weakened and by 0000 GMT, 12 December a strong wind band had formed to the north of the trough position. A smaller depression which was situated over the west coast of Canada during the earlier part of the period deepened

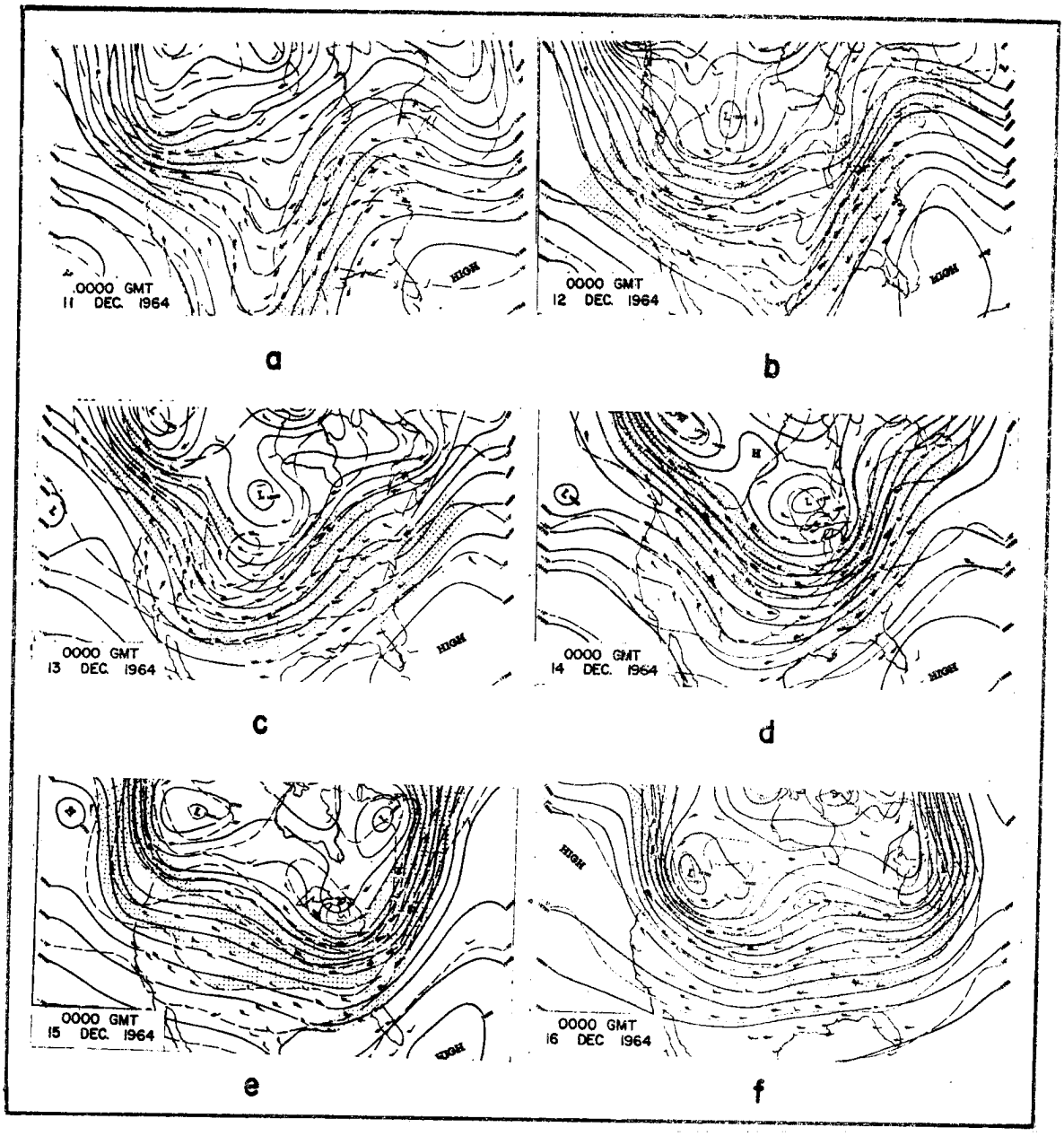

Figure 11. 500-mb height contours (solid lines, ft) for times shown. Dashed lines are isotherms (°C). Arrows show wind direction and speed. Shaded portions denote wind speeds greater than 50 knots. (Reproduced from U.S. Weather Bureau daily weather map series)

to form a closed low and moved eastward bringing very strong winds over the United States at the 500 mb level (see Figure 11 c). On the 14th this new low center progressed eastward over southern Canada where it became stationary near 70°W longitude. Meanwhile another disturbance had moved down the west coast of Canada into a position over British Columbia. The relative location of these two low centers shown in Figures 11 e and 11 f created strong, nearly zonal, flow over the United States. This pattern persisted for the remainder of the period. Therefore, the surface pressure disturbances which were moving to the north of the Great Basin high did not progress southward.

Again, to exhibit the effect of the synoptic scale patterns on a leeside station a time section of the surface parameters at Denver, Colorado, for 12 December 1964 to 17 December 1964 is shown in Figure 12. It is immediately apparent that this chinook was much stronger than those which occurred during the April case. The maximum wind speeds are much greater and more persistent. The most important difference, however, is that the December chinook was a continuous phenomenon not interrupted by diurnal effects. From its inception on 12 December to its end on 16 December only slight pauses can be noted, the largest of which occurred on 15 December. There are indications that this pause was a local phenomenon confined only to the immediate area of Denver. Referring to Figure 10 e, which shows the surface map for 0600 GMT, 15 December, it can be seen that the wind at Denver has shifted to the south while the stations on either side of Denver are maintaining their strong westerly winds. A possible explanation for this local effect may be found in the isobaric pattern over the region at that time. The greater spacing of isobars between Denver, Colorado, and Cheyenne, Wyoming, indicated that a meso-scale low may have formed to the west of Denver causing the wind to have a southerly component. This hypothesis has not been investigated and is offered only as a possible explanation for the break in the otherwise continuous chinook conditions at Denver.

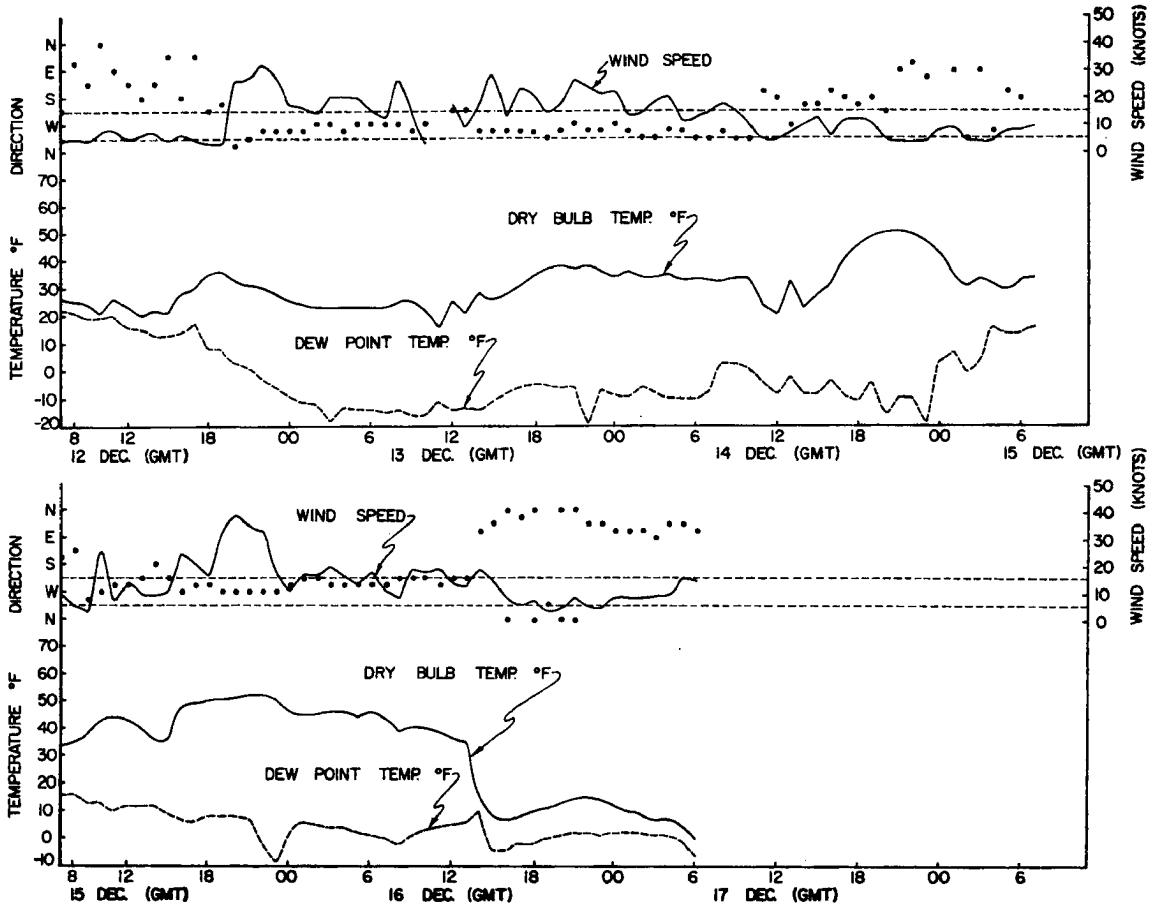

Figure 12. Time section of hourly surface observation at Denver, Colorado, from 12 December 1964 to 17 December 1964. Upper solid line is surface wind speed (knots), lower solid line is dry bulb temperature (°F). Dashed line is dew point temperature (°F) and dots indicate wind direction. All dots between the two horizontal dashed lines are for winds having a westerly component.

CHAPTER IV

ANALYSIS AND RESULTS FOR CHINOOK CASES

The area covered by these cases is much larger and topographically more complex than the one studied by Lockwood (1962). For this reason a different approach was used in determining the value of π/ℓ and its relation to the mountain height. Radiosonde stations located in and near the mountain complex to be investigated were selected and values of π/ℓ were calculated for the surface inversion when it occurred. In the first case, it should be noted that only surface inversions produced by nocturnal cooling were stable enough to be of significance, supporting the speculation that there was a diurnal control on these chinooks. The calculated value of π/ℓ for each station in the area was then added to the station elevation. In this manner π/ℓ could be related to terrain in the area under consideration. It was then possible to analyze a field of $(\pi/\ell) + Z_{sta}$ where Z_{sta} is the elevation of the station, and to superimpose this analysis on a topographic map of the region. Noting points where the isolines of $(\pi/\ell) + Z_{sta}$ intersected a mountain contour of equal height and then connecting these points, areas having a height $\geq (\pi/\ell) + Z_{sta}$ were defined. The streamline patterns for the 700 mb pressure surface were then analyzed to determine if the mountains were properly oriented to block low level flow and cause the necessary subsidence on the leeward side.

Findings for April case

Figure 13 shows the field of $(\pi/\ell) + Z_{sta}$ for 1200 GMT, 15 April superimposed on a map of terrain contours. The cross hatched portion is the region where the mountains are higher than

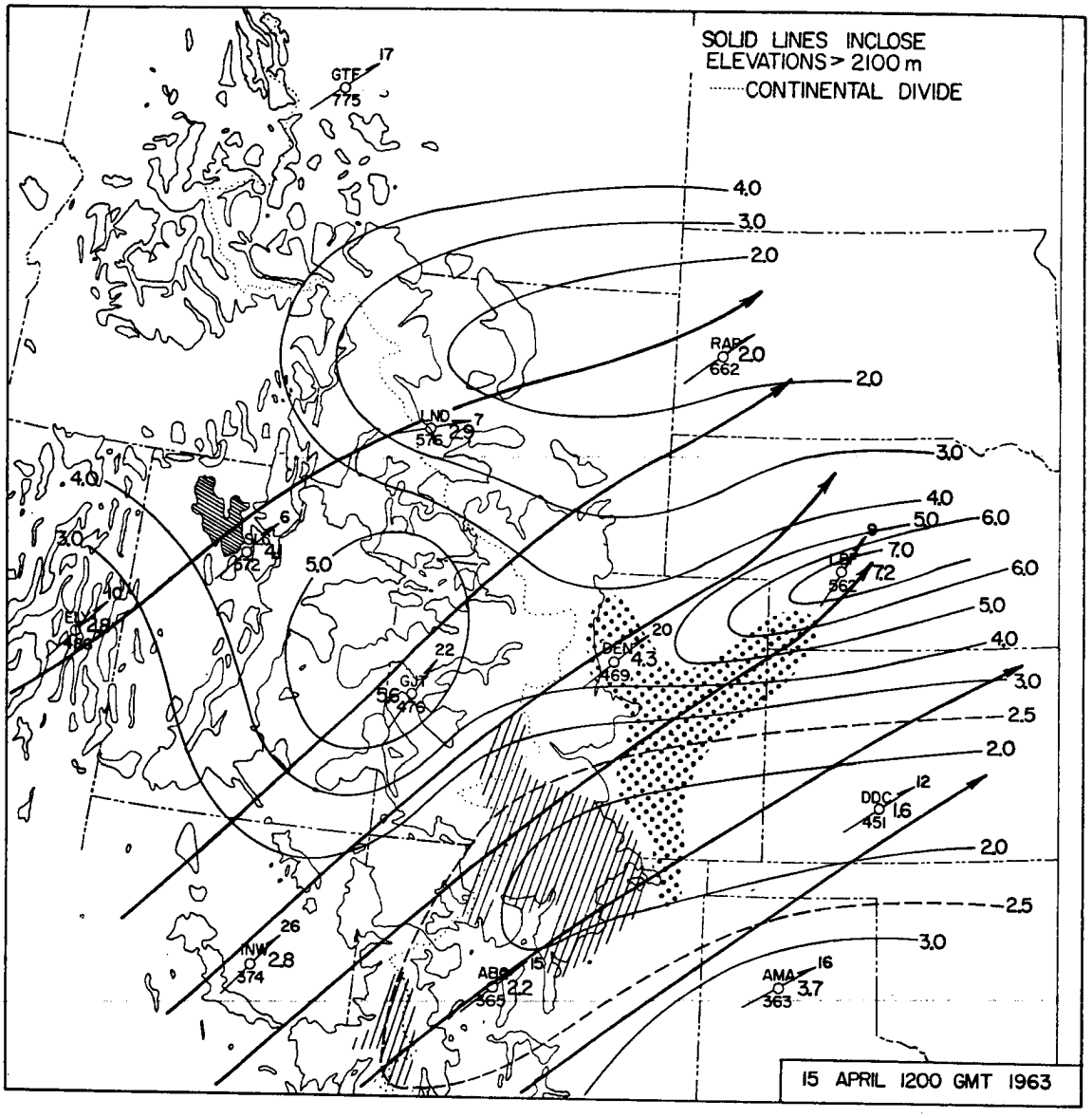

Figure 13. Field of $(\pi/\ell) + Z_{sta}$ (solid lines, km) for time shown superimposed on map of terrain contours. Area where mountains are higher than $(\pi/\ell) + Z_{sta}$ field is cross hatched. Heavy lines are 700 mb streamline pattern. Dotted portion shows area affected by chinook at 15 April 1800 GMT. 700 mb wind speed (mps) and direction (arrow) shown at station. Number shown by stations is the value of $(\pi/\ell) + Z_{sta}$ (km).

the analyzed values of $(\pi/\ell) + Z_{sta}$. The surface map for 1800 GMT, 15 April is shown in Figure 14. Foehn areas were defined by regions having large temperature-dew point temperature ($T - T_d$) spreads. From this it is apparent that the area northeast of the cross hatched region and along the 700 mb streamlines is being influenced by a chinook.

The area enclosed by the 60°F temperature dew point spread line from the 1800 GMT, 15 April surface map is denoted in Figure 13 by the dotted area. The juxtaposition of the terrain height $\geq (\pi/\ell) + Z_{sta}$ and the temperature dew point spread > 60°F is indeed striking and certainly lends credence to Scorer and Klieforth's suggestion.

A six-hour lag between the $(\pi/\ell) + Z_{sta}$ analysis and the chinook area analysis was applied to compensate for the time it took an air parcel to descend from the controlling mountain region to the leeward station. This value was computed by taking an average wind speed of 20 knots at 700 mb and using 120 nautical miles as a representative distance between the controlling mountains and the leeward stations.

The reason for the lack of chinook conditions in Colorado and Wyoming on 17 April (see Figures 9 and 15) is apparent from the 700 mb streamline analysis in Figure 16. Although the $(\pi/\ell) + Z_{sta}$ field (see Figure 16) shows a large portion of the region capable of producing downslope motion, the 700 mb streamlines are nearly parallel to the main ridge of the Rockies; thus producing only a very small component of the wind normal to the mountain ranges. Unless this component is fairly strong, no chinook will occur regardless of the height of the mountains. From this it follows that π/ℓ criteria is a necessary, but not a sufficient, condition for predicting leeward subsidence.

The analysis for the next important chinook appears in Figure 17. Critical mountain regions and the area affected by a chinook are not as well correlated in this case. The critical mountain heights extend from northern New Mexico to southern Montana while the chinook only covers an area from the Oklahoma panhandle to northern Colorado.

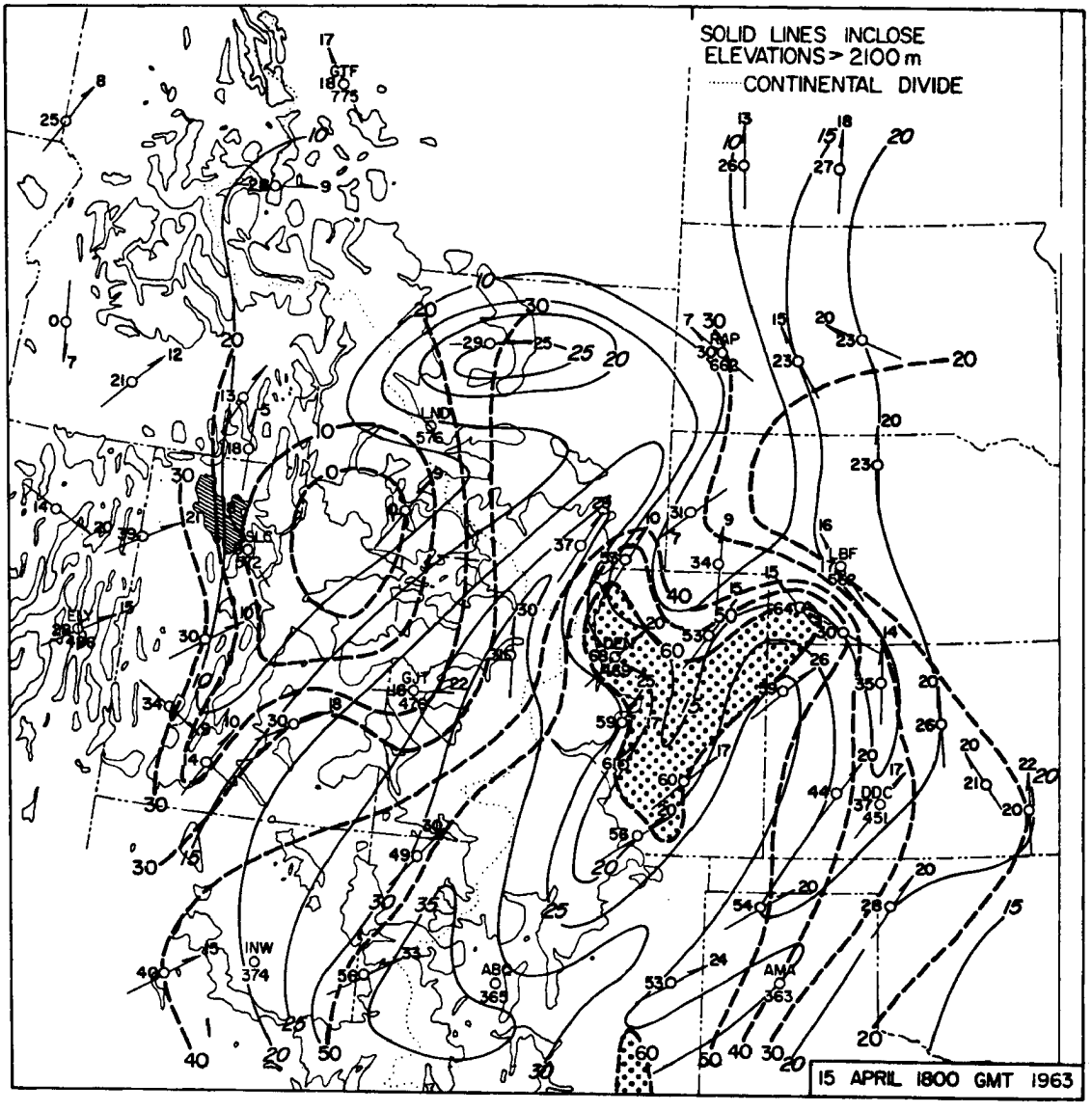

Figure 14. Surface analysis for time shown. Dashed lines show field of dry bulb temperature minus dew point temperature (^{o}F), areas > 60^{o}F are shaded. Isotachs (knots) are shown by light solid lines. Dotted portion shows chinook area.

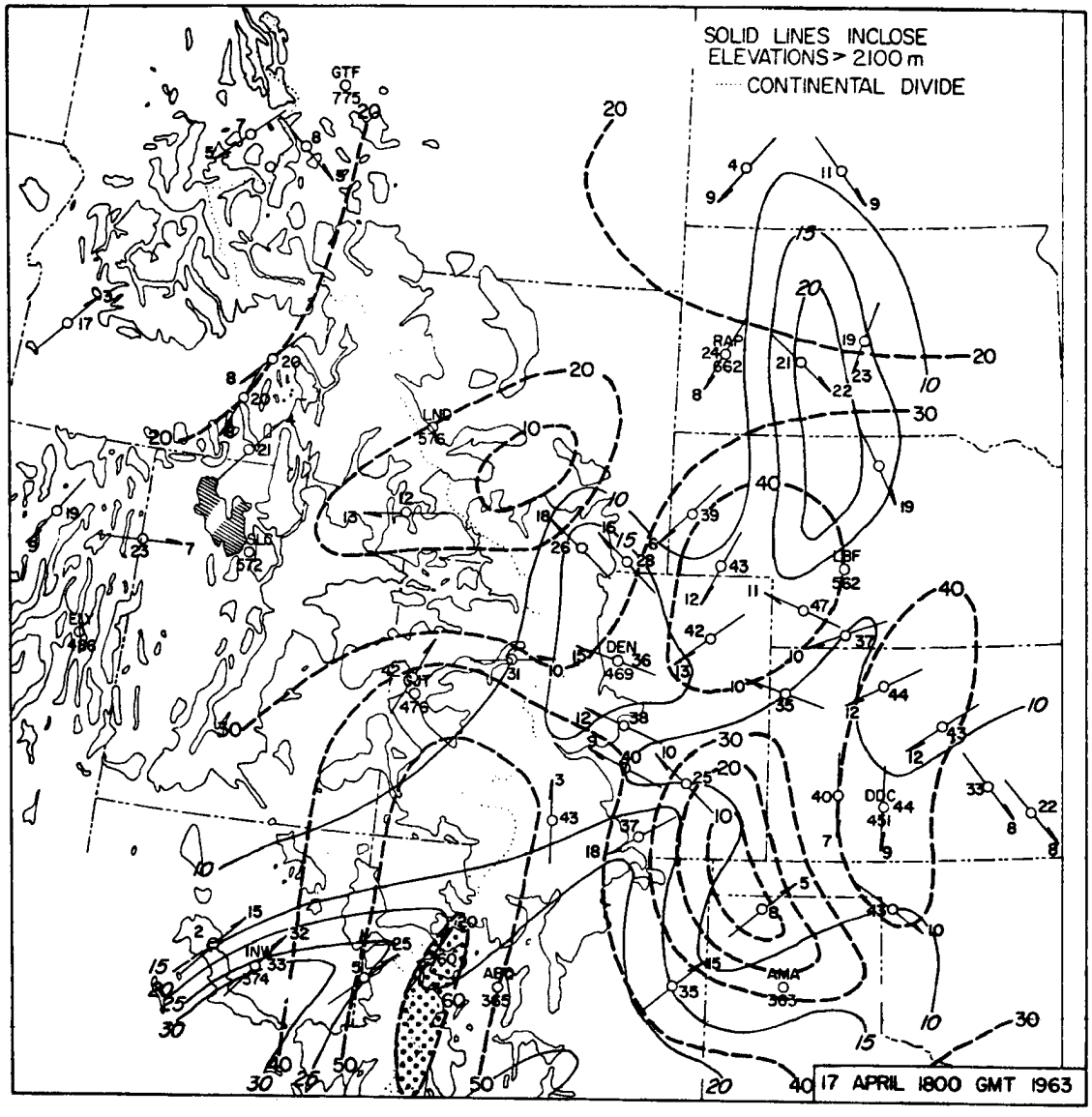

Figure 15. Surface analysis for time shown. Dashed lines show field of dry bulb temperature minus dew point temperature (^{o}F). Isotachs (knots) are shown by light solid lines.

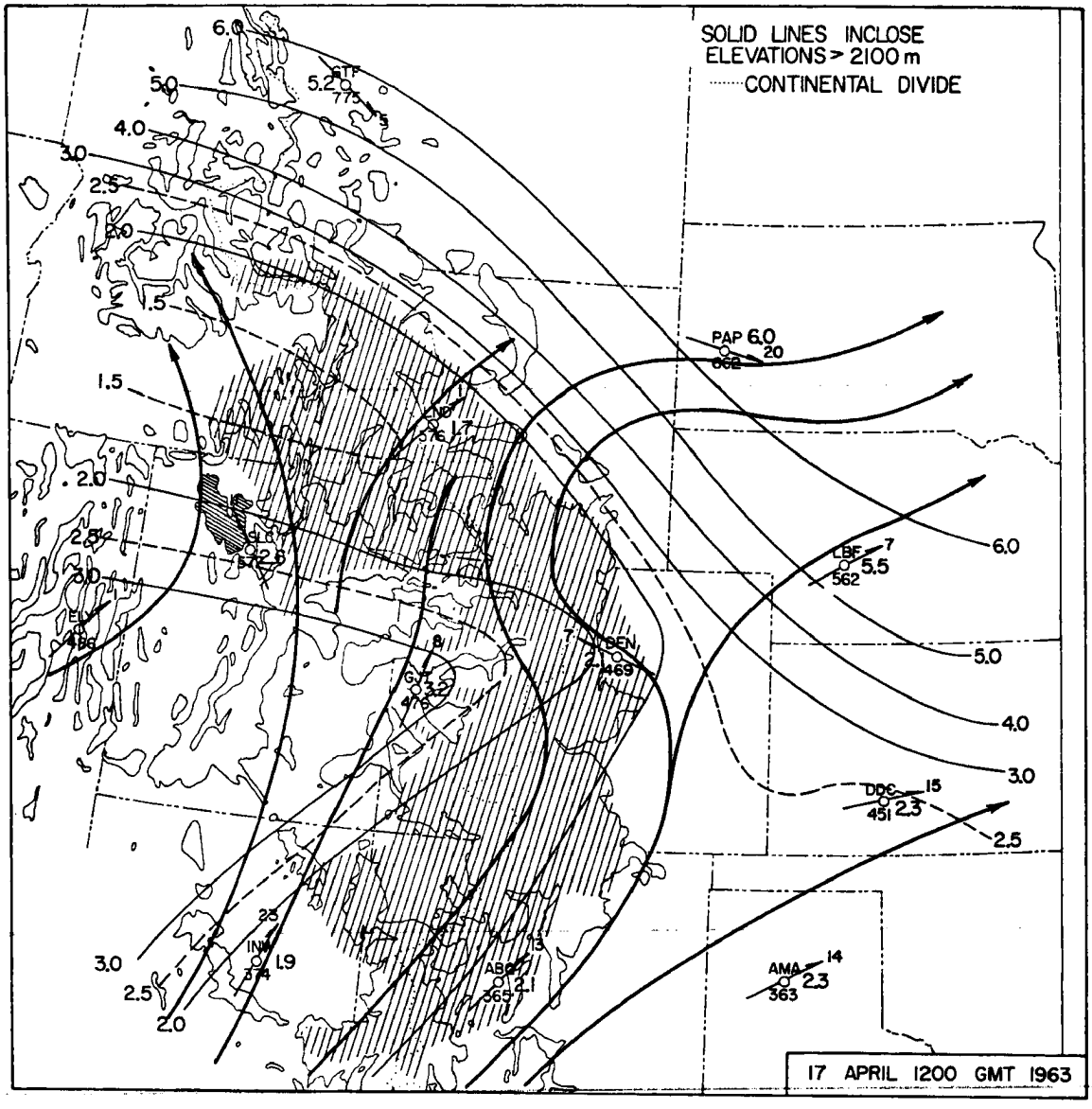

Figure 16. Field of $(\pi/\ell) + Z_{sta}$ (solid lines, km) for time shown superimposed on map of terrain contours. Area where mountains are higher than $(\pi/\ell) + Z_{sta}$ field is cross hatched. Heavy lines are 700 mb streamline pattern. 700 mb wind speed (mps) and direction (arrow) shown at station. Number by station is the value of $(\pi/\ell) + Z_{sta}$ (km).

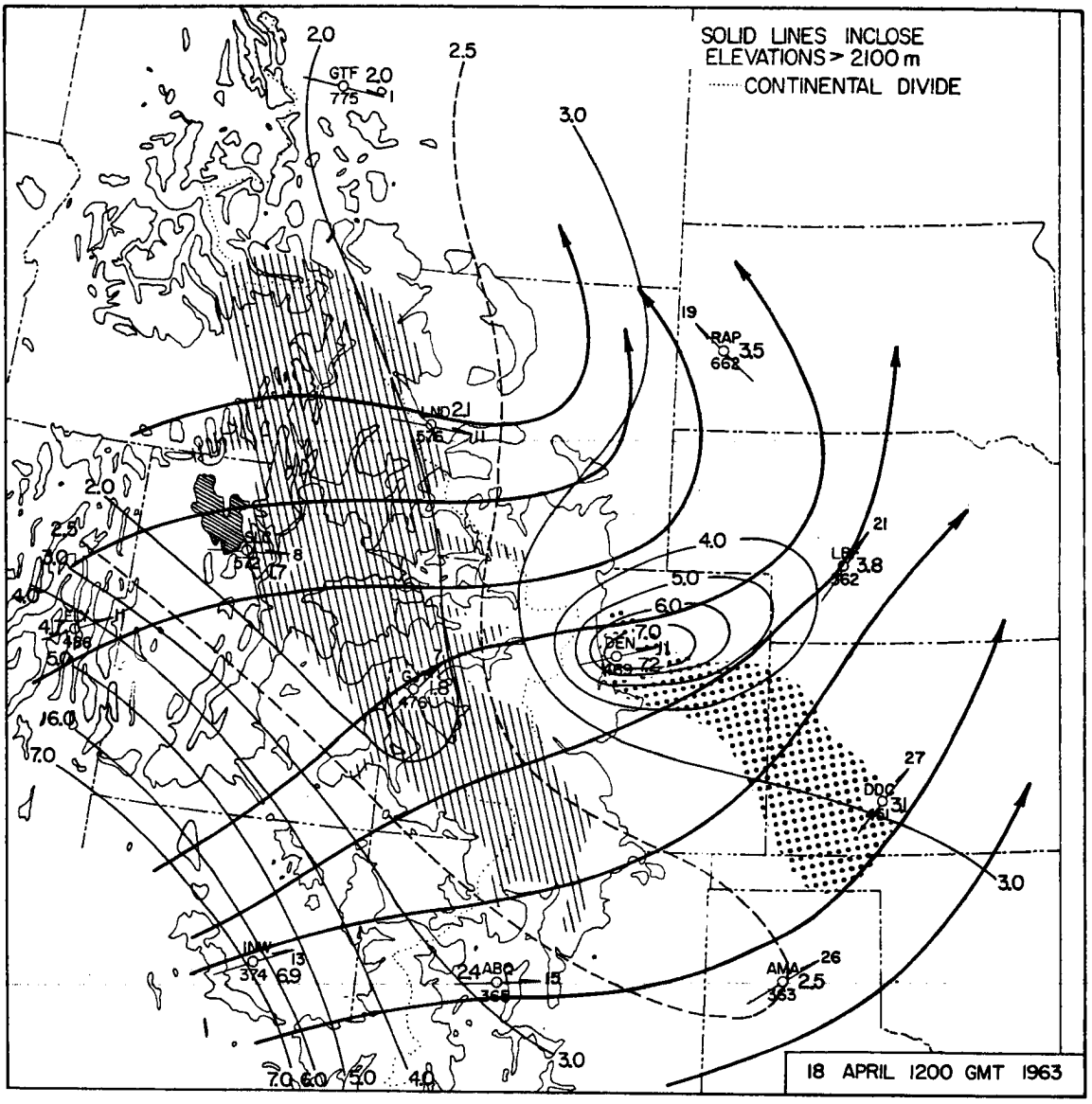

Figure 17. Field of $(\pi/\ell) + Z_{sta}$ (solid lines, km) for time shown superimposed on map of terrain contours. Area where mountains are higher than $(\pi/\ell) + Z_{sta}$ field is cross hatched. Heavy lines are 700 mb streamline pattern. Dotted portion shows area affected by chinook 18 April 18 GMT. 700 mb wind speed (mps) and direction (arrow) shown at station. Number by station is the value of $(\pi/\ell) + Z_{sta}$ (km).

Surface reports and TIROS photographs indicate that the northern portion of this chinook was at least partially caused by precipitation to the windward side of the mountains. Figure 6 shows frame 14 from TIROS V orbit 4349 (tape) taken 1955 GMT, 18 April 1963. The cloud pattern defines a sharp line running along 105°W longitude from 35°N latitude to the top of the picture. The edge of this cloud bank is parallel to the crest of the Rocky Mountains suggesting the "wall cloud" formation usually associated with the release of latent heat on the windward side of the mountains. The TIROS picture and the streamlines in Figure 17 indicate a low pressure center over Wyoming. This depression produced clouds and precipitation (see Figure 18) from northern Colorado to southern Montana. The moisture associated with this convergence area caused dew point spreads, the primary indicator used to define chinook areas, to be much smaller than the dryer areas to the south (see Figure 19). This low pressure area and its associated moisture to the lee of the mountain helps to explain why the chinook area in Figure 17 does not extend through northern Colorado into Wyoming.

Findings for December case

The December 1964 case did not show the diurnal variation which typified the period in April 1963. The surface inversion layer on the windward side of the mountains was not eliminated by diurnal heating, and the analyzed field of $(\pi/\ell) + Z_{sta}$ indicated mountain areas high enough to produce the necessary downslope motion on both 0000 GMT and 1200 GMT map times. Figures 20 and 21 show the $(\pi/\ell) + Z_{sta}$ analysis for 1200 GMT, 14 December 1964 and 0000 GMT, 15 December 1964. These figures are typical of all map times during the second period. As in the April case,

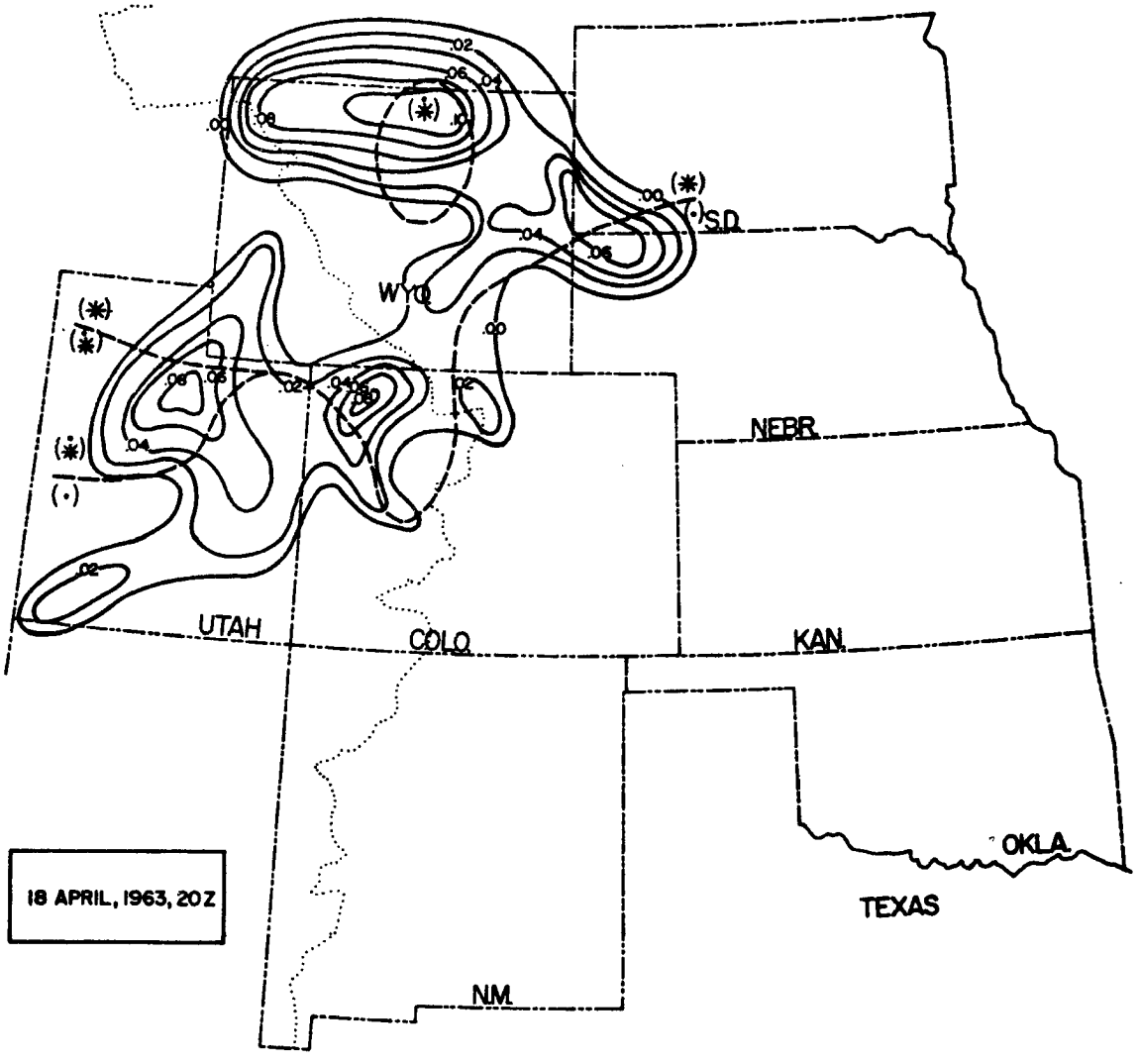

Figure 18. Precipitation (inches) within four hours prior to time shown. Dashed lines indicate boundaries between snow, rain and snow mixed, and rain. Dotted line indicates Continental Divide.

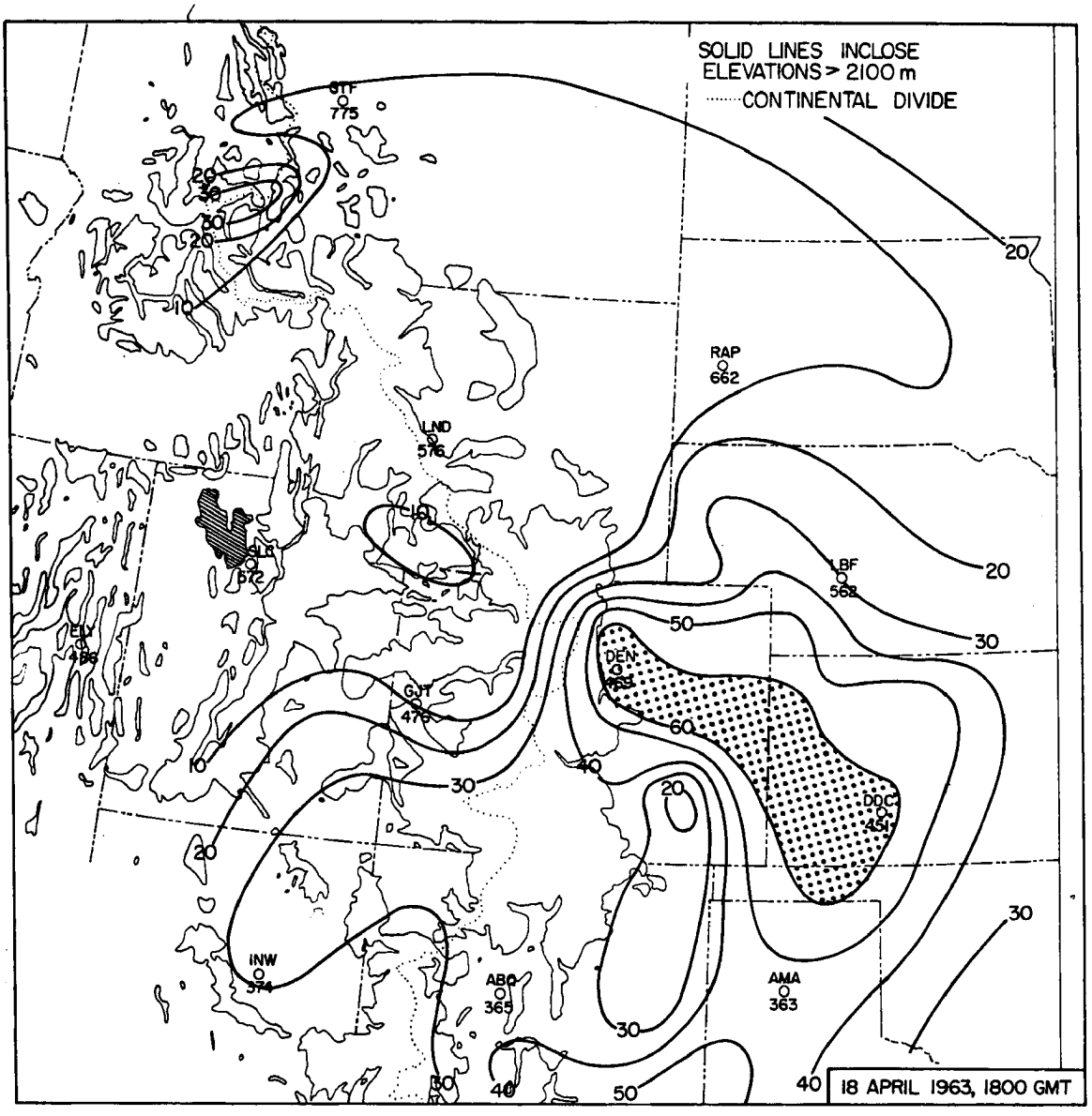

Figure 19. Temperature-dew point temperature ($T - T_d$) spread (^{o}F) for time shown. Chinook winds are causing dry region (dotted portion). Moist area to northwest of Colorado is under the influence of a low pressure system and corresponds to the precipitation region shown in Figure 18.

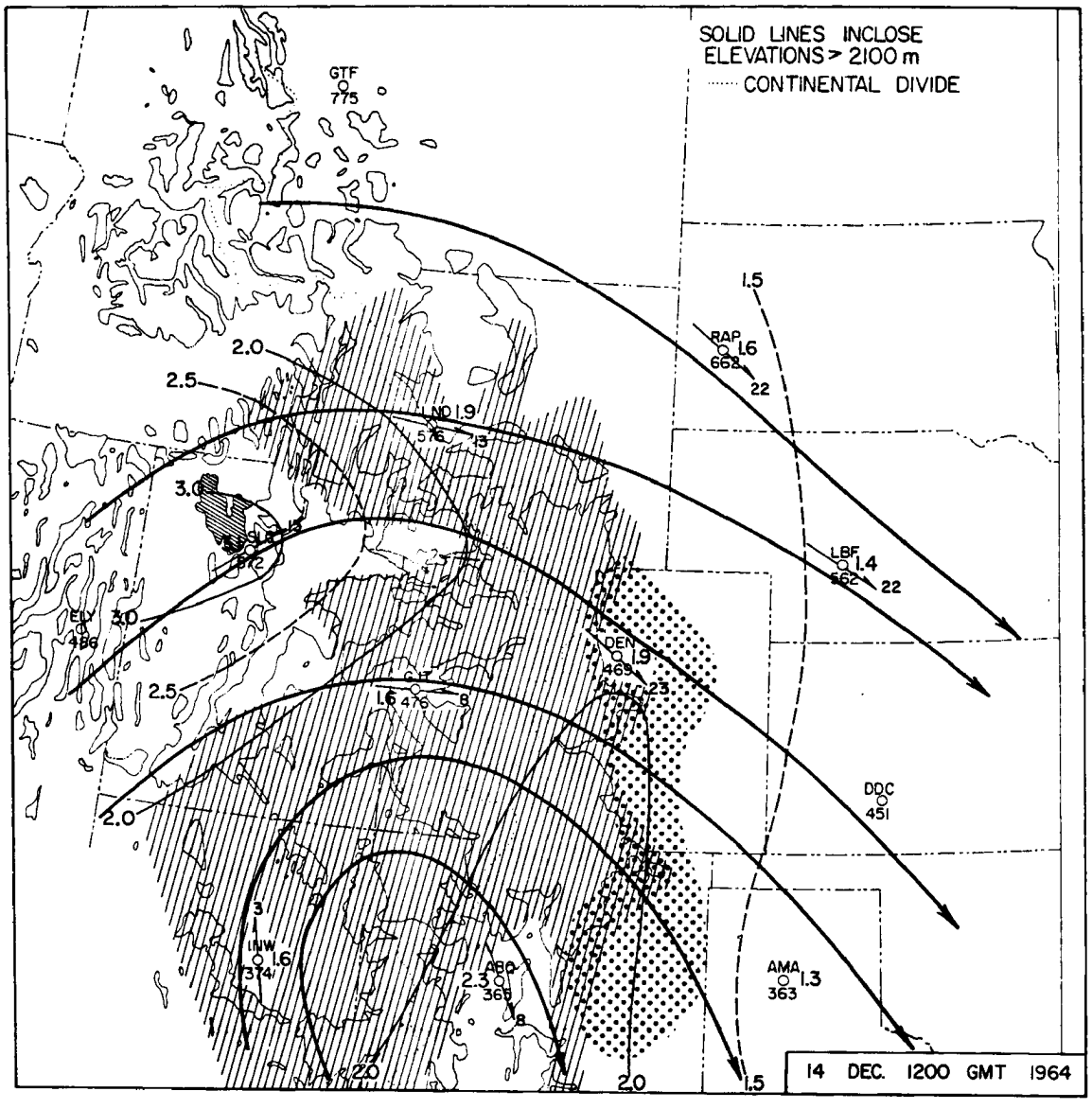

Figure 20. Field of $(\pi/\ell) + Z_{sta}$ (solid lines, km) for time shown superimposed on map of terrain contours. Area where mountains are higher than $(\pi/\ell) + Z_{sta}$ field is cross hatched. Heavy lines are 700 mb streamline patterns. Dotted portion shows area affected by chinook at 14 December 1800 GMT. 700 mb wind speed (mps) and direction (arrow) shown at station. Number shown by stations is the value of $(\pi/\ell) + Z_{sta}$ (km).

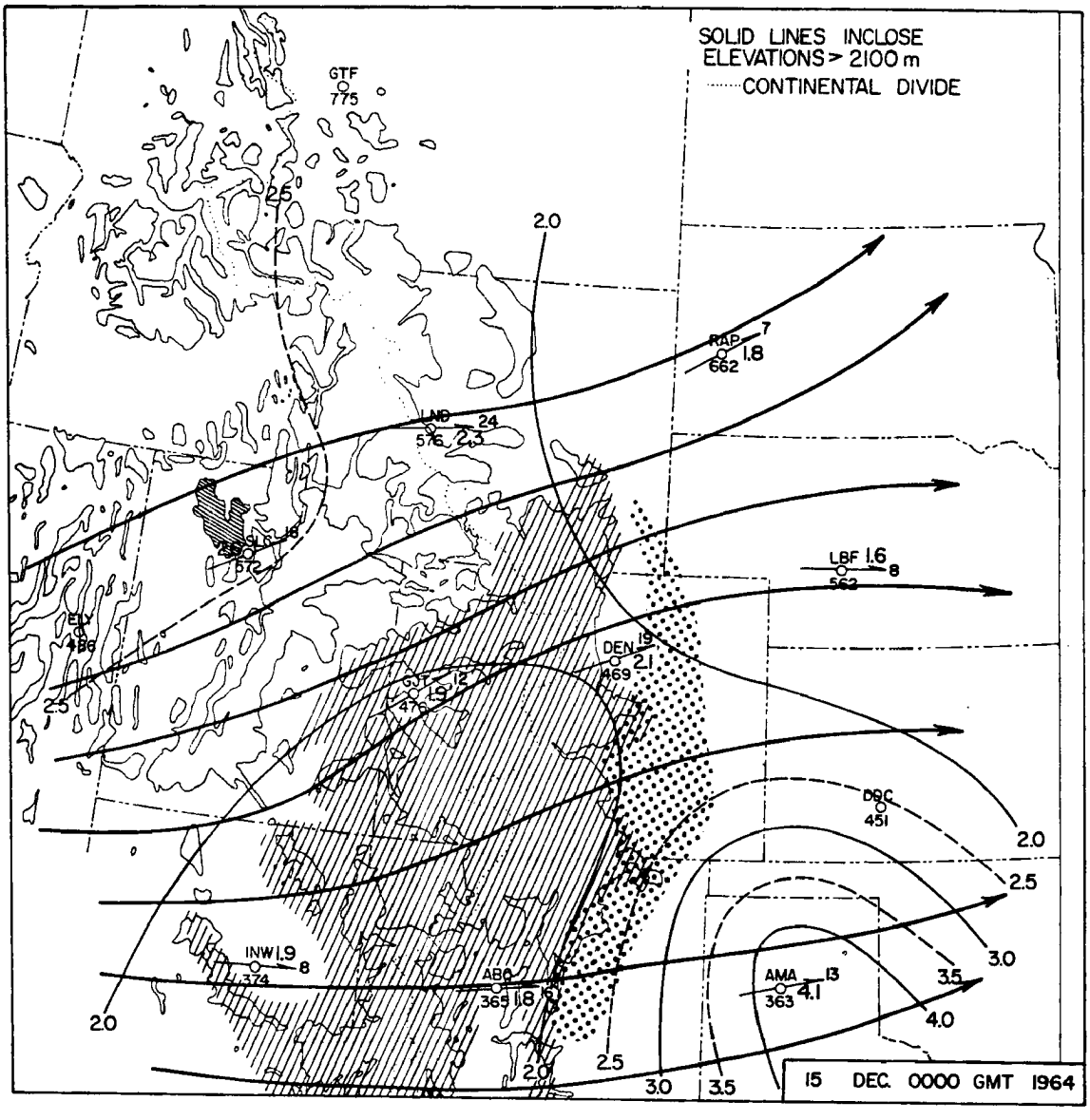

Figure 21. Field of $(\pi/\ell) + Z_{sta}$ (solid lines, km) for time shown superimposed on map of terrain contours. Area where mountains are higher than $(\pi/\ell) + Z_{sta}$ field is cross hatched. Heavy lines are 700 mb streamline pattern. Dotted portion shows area affected by chinook at 15 December 0600 GMT. 700 mb wind speed (mps) and direction (arrow) shown at station. Number shown by stations is the value of $(\pi/\ell) + Z_{sta}$ (km).

the cross hatched portion depicts mountain areas high enough to create chinook conditions, and the dots indicate where the strongest chinooks actually occurred.

The intense pressure gradient formed between the Great Basin high and the migratory lows moving across Montana produced strong leeside winds in Wyoming and Colorado. Comparison of Figures 20 and 21 with Figure 10 shows that chinook conditions were not associated with the leeside winds in Wyoming. There are two possible reasons for the lack of warming and of large dew point spread in this region. First, the wind direction, shown by the 700 mb streamlines in Figure 20 tends to be nearly parallel to the northwest-southeast oriented mountains in Wyoming. Second, the windward inversion over Idaho and Utah was not stable enough to produce critical values of π/ℓ .

Diurnal Control

If the 700 mb wind direction had been normal to the mountains on 17 April, Denver would probably have experienced at least one chinook period on each day of the April case (see Figure 9). The low level inversion layers on the windward side, already established as an important factor, are controlled to a large extent by the daily changes in surface temperature. This seems to support the hypothesis that diurnal fluctuations of the windward surface inversion exert a similar periodic influence on leeward chinooks.

To establish a possible correlation between the onset time of surface inversions on the windward side of a mountain and the beginning of a chinook on the leeward side, it was necessary to determine the path of an air parcel over the mountains. Petterssen's (1956) trajectory computations were applied to air parcels originating to the windward side of the mountains on the 700 mb surface (see Figure 22). Trajectories from Winslow, Arizona, were reasonably close (see Figure 25) to Denver for each map time during the case. Therefore,

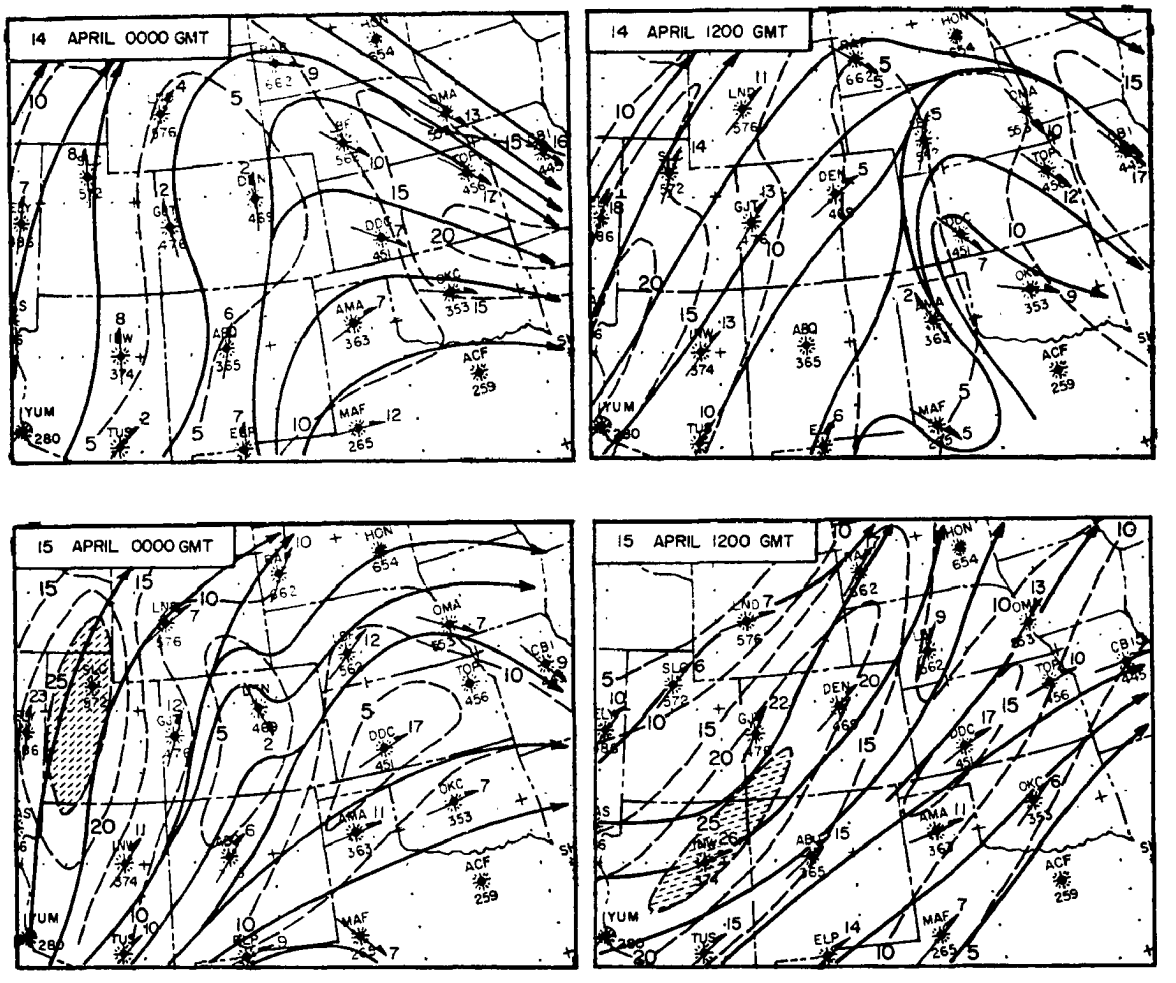

Figure 22. 700-mb streamlines (solid lines) and isotachs (dashed lines, mps) for times shown. Areas with wind speed greater than 25 mps are shaded.

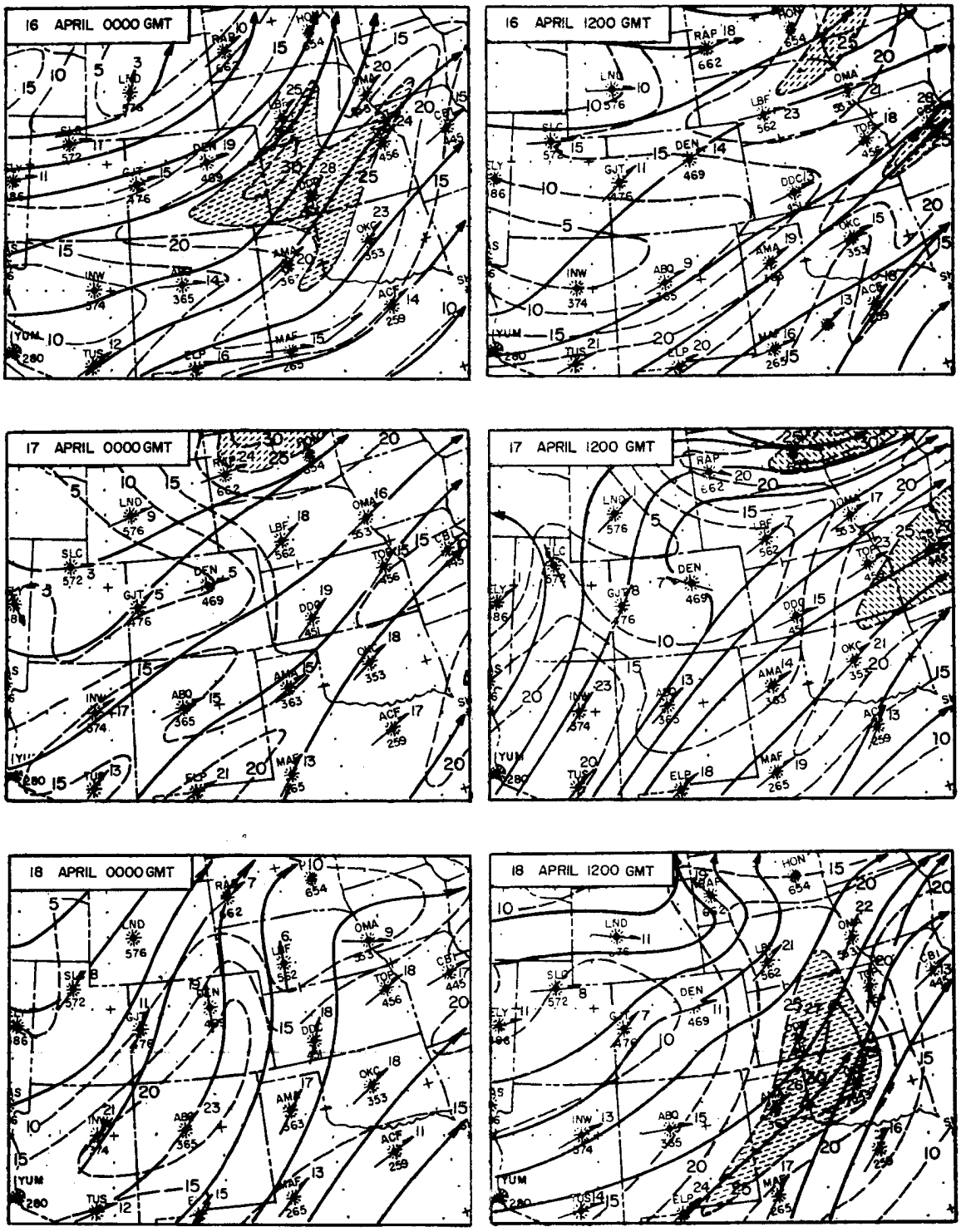

Figure 22. Continued.

the Winslow soundings and surface temperatures appeared to be the most logical choice for determining onset times of the windward inversion.

Plots of temperature versus height for the standard radiosonde ascents at Winslow are shown on the left side of Figure 23. According to these soundings, the nocturnal inversion was removed daily by surface heating. The 12-hour interval between soundings makes it impossible to determine exactly when they started. A reasonable estimate for the time of these occurrences was established by defining a critical lapse rate and then determining when the surface temperature reached the required value.

The critical lapse rate was estimated by using Scorer's simplified equation (neglecting the shear term, $-\frac{1}{U}\frac{\partial^2 U}{\partial z^2}$)

$$\ell^2 = \frac{g\beta}{U^2} \quad . \tag{7}$$

Solving this equation for β and replacing β by $\frac{1}{\theta}\frac{\partial \theta}{\partial z}$, we obtain for the lapse rate

$$\frac{\partial \theta}{\partial z} = \theta \frac{\ell^2 U^2}{g} \quad . \tag{8}$$

Using Scorer and Klieforth's value for chinook occurrence of π/ℓ = mountain height (mtn. ht.), and solving for ℓ, we can substitute into equation (8) and arrive at

$$\frac{\partial \theta}{\partial z} = \theta \frac{\left(\frac{\pi}{\text{mtn. ht.}}\right)^2 (U)^2}{g} \quad . \tag{9}$$

By substituting a typical value of U for the inversion layer and a mountain height determined from a topographic map into equation (9), the critical lapse rate was found to be very nearly isothermal. Using this lapse rate and the Winslow soundings, the time range within which the onset of a critical lapse rate could have occurred

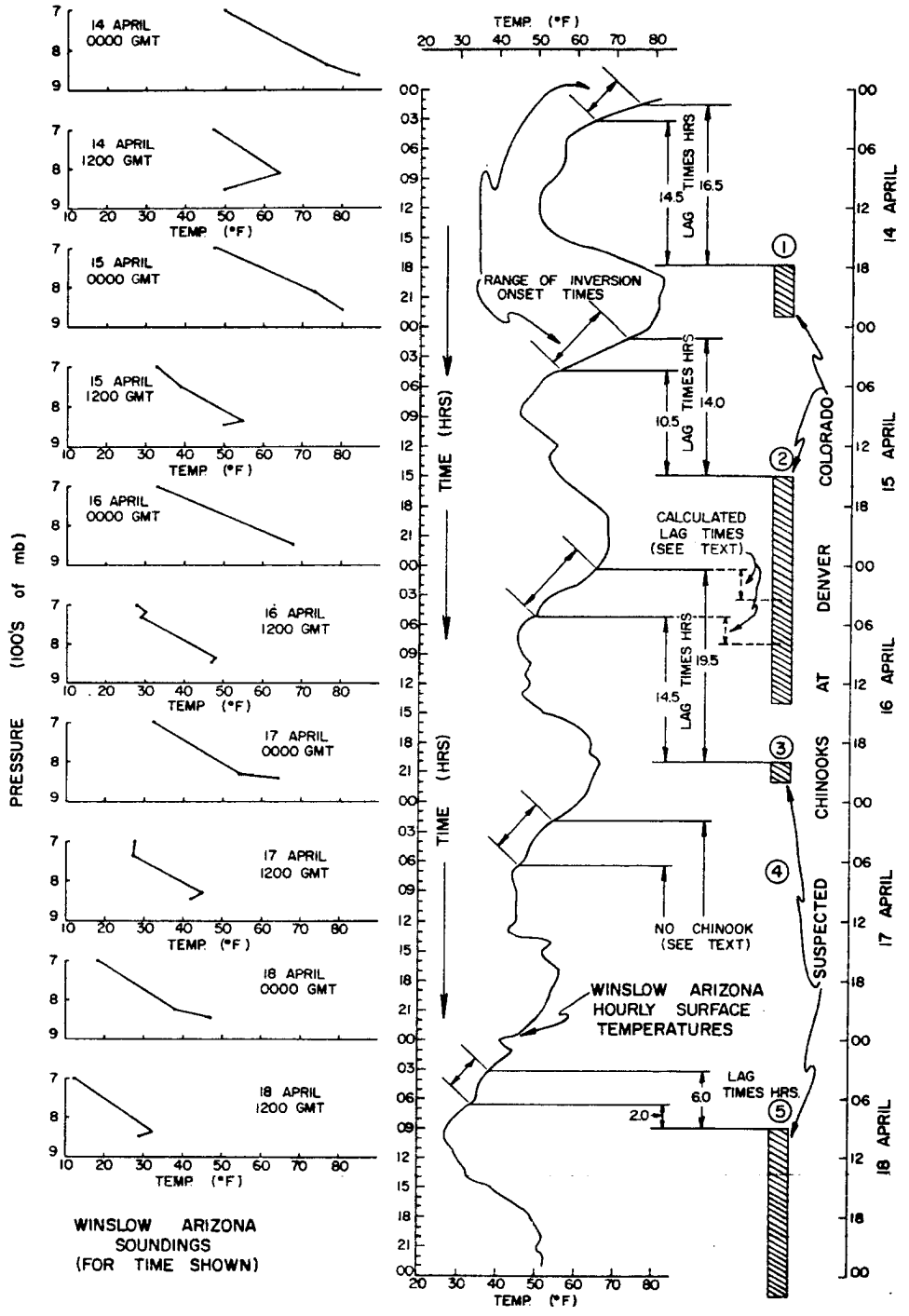

Figure 23. Chart used to determine inversion onset times. Winslow, Arizona, soundings on left side of diagram. Trace of Winslow surface temperatures in center of diagram. Chinook occurrences, from Figure 9, are on right side of diagram, plotted along same time scale as the surface temperatures. The observed lag times between inversion and chinook onset are to the right of surface temperature.

was determined as follows: Figure 24 shows two soundings, 12 hours apart, which were taken during the period under study. The sounding on the right was taken during daytime, the one on the left during the following night. Clearly the lower levels experienced an isothermal lapse rate between the two soundings. Looking first at the daytime sounding and assuming that the air mass above the surface layer (portion of curve above the first significant level) did not change, the earliest possible time at which an isothermal lapse rate could have occurred was when the surface temperature reached 76°F (shown by the right hand dashed line in Figure 24). Next, referring to the nighttime curve and assuming that air above the surface layer had cooled until it reached the slope shown in the diagram, the latest time at which an isothermal lapse rate could have appeared was when the surface temperature reached 64°F (shown by the left hand dashed line in Figure 24).

A similar procedure was used to determine the range of surface temperatures for each set of soundings shown on the left in Figure 23. These values were noted on the curve of hourly surface temperature, shown as a function of time in the center of Figure 23. A range of inversion onset times could then be found. These are shown by the distance between the straight lines running from the center curve. This method reduces the possible times when the critical inversion could have started to a few hours, depending on the slope of the surface temperature curve.

The chinooks at Denver (see Figure 9), were plotted along the same time scale used for the surface temperature at Winslow in Figure 23. The lag between the inversion onset times and the beginning of the chinooks was graphically determined from Figure 23 to the right of the surface temperature trace. These times are a function of wind speed, and distance traveled by the

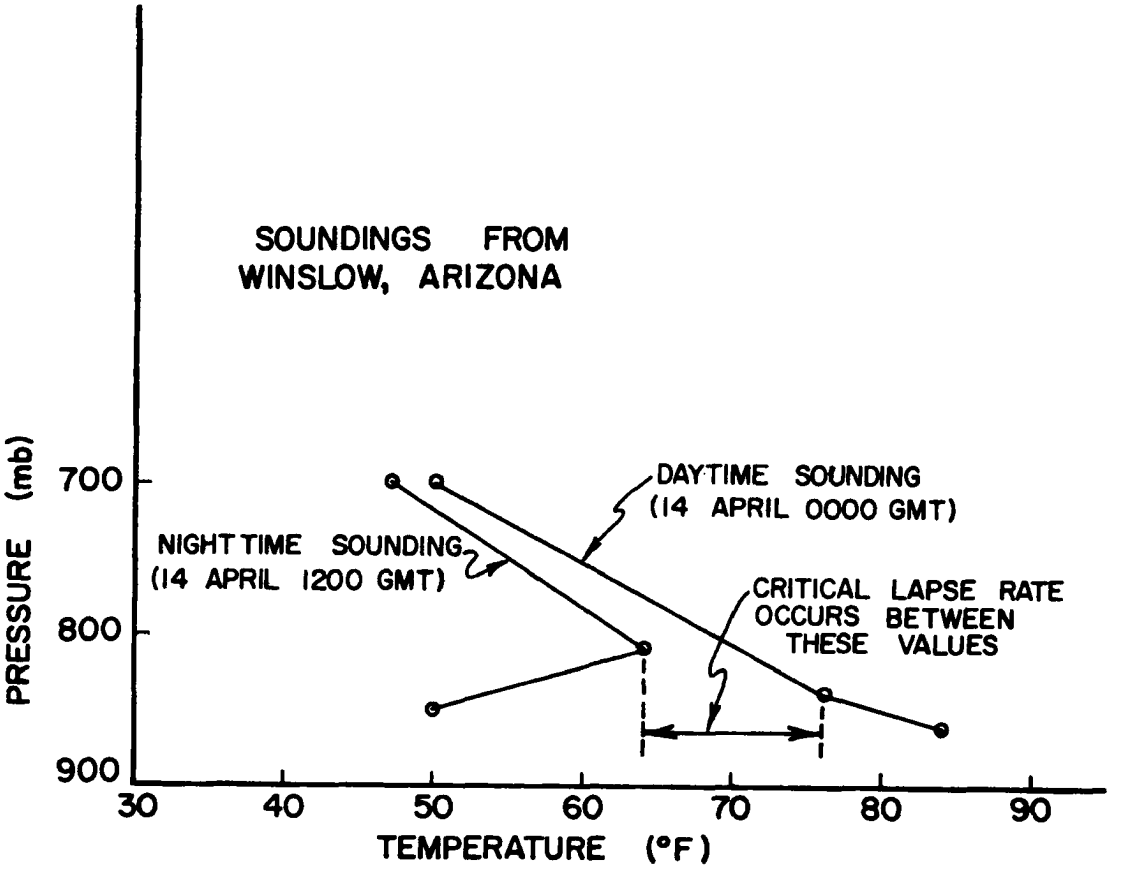

Figure 24. Winslow, Arizona, soundings showing method of determining the range of surface temperatures between which an isothermal lapse rate could occur. For this example, the critical lapse rate occurred between the times when the surface temperature went from 76°F to 64°F.

parcel. A calculated lag time was arrived at by estimating the wind speed from the isotach pattern in Figure 22 and by measuring the distance between the center of the mountain region greater than π/ℓ and Denver. Table I shows a comparison of the observed lag times taken from Figure 23 and the calculated lag times.

TABLE I

COMPARISON OF OBSERVED AND CALCULATED LAG TIMES

Chinook No. *	Observed lag time (hrs)*	700 mb wind speed (mps)**	Distance traveled (deg lat)	Calculated lag time (hrs)
1	14.5 to 16.5	5	2.5	15
2	10.5 to 14.0	6	2.1	11
3	14.5 to 19.5	20	2.1	3
4	-	No Chinook	-	-
5	2.0 to 6.0	20	2.5	4

*Values taken from Figure 23
**Values taken from Figure 22

The observed values for chinook numbers 1, 2, and 5 are well within the limit of the calculated lag times for these periods. The large difference between observed and calculated values in row 3 of Table I suggests this particular chinook occurrence was not associated with the inversion formation on the windward side to which it has been linked in Figure 23. Rather, it appears that the onset of any chinook associated with this inversion formation occurred while the chinook from the previous day was still active (see dashed lines leading from chinook number 2, Figure 23). The longer duration of this chinook is probably due to the frontal passage during this time. Therefore, if the real onset of chinook number 3 was masked by the activity

extending from the previous day, the "observed" values in row 3 must be disregarded.

The 700 mb wind speeds and the inversion onset times used in the above development leave much to be desired; however, they are the best available using present observation networks. Keeping this in mind, it appears that there is justification for the hypothesis that moderate or weak chinook winds are controlled by diurnal influences on the windward side of the mountains.

CHAPTER V

UPPER LEVEL FLOW DURING CHINOOK

In the previous sections we have investigated the effect of low level atmospheric structure and meso-scale flow on the generation of chinook winds in the Rocky Mountain region. In the following, the correlation of chinook cases with large scale characteristics of flow patterns, such as vorticity and divergences and with cloud distributions as shown by TIROS, will be described. The analyzed maps showing these flow characteristics are compared with TIROS photographs taken during the period of interest to see what inferences on orographic effects could be drawn from cloud patterns on meteorological satellite pictures. Two levels, 250 and 700 mb, were selected for detailed analysis. The 250 mb surface was used because it gives the best horizontal description of the jet stream, while 700 mb was close enough to the ground to show parameters influencing cloud distribution, such as moisture and low level disturbances. The first chinook case, 16 April 1963 to 19 April 1963, was selected for detailed analysis because of the TIROS coverage during this time.

Analysis of Wind and Mixing Ratio Fields

The 700 mb streamlines and isotachs (see Figure 22) describe the low level flow pattern during the April case. A wind maximum was present on the leeward side of the Rocky Mountains in Colorado and the states immediately to the east of this region. This strong wind zone undoubtedly played a role in the chinook-producing mechanism during the April period. Large amplitude lee waves induced by the mountains caused these strong winds at the 700 mb level to descend and impinge on the high plains region of eastern Colorado, Kansas, and Nebraska.

Air parcel trajectories at the 700 mb level were constructed using the Petterssen (1956) method. These trajectories (see Figure 25) indicate that the flow originating from stations as far south as Winslow, Arizona

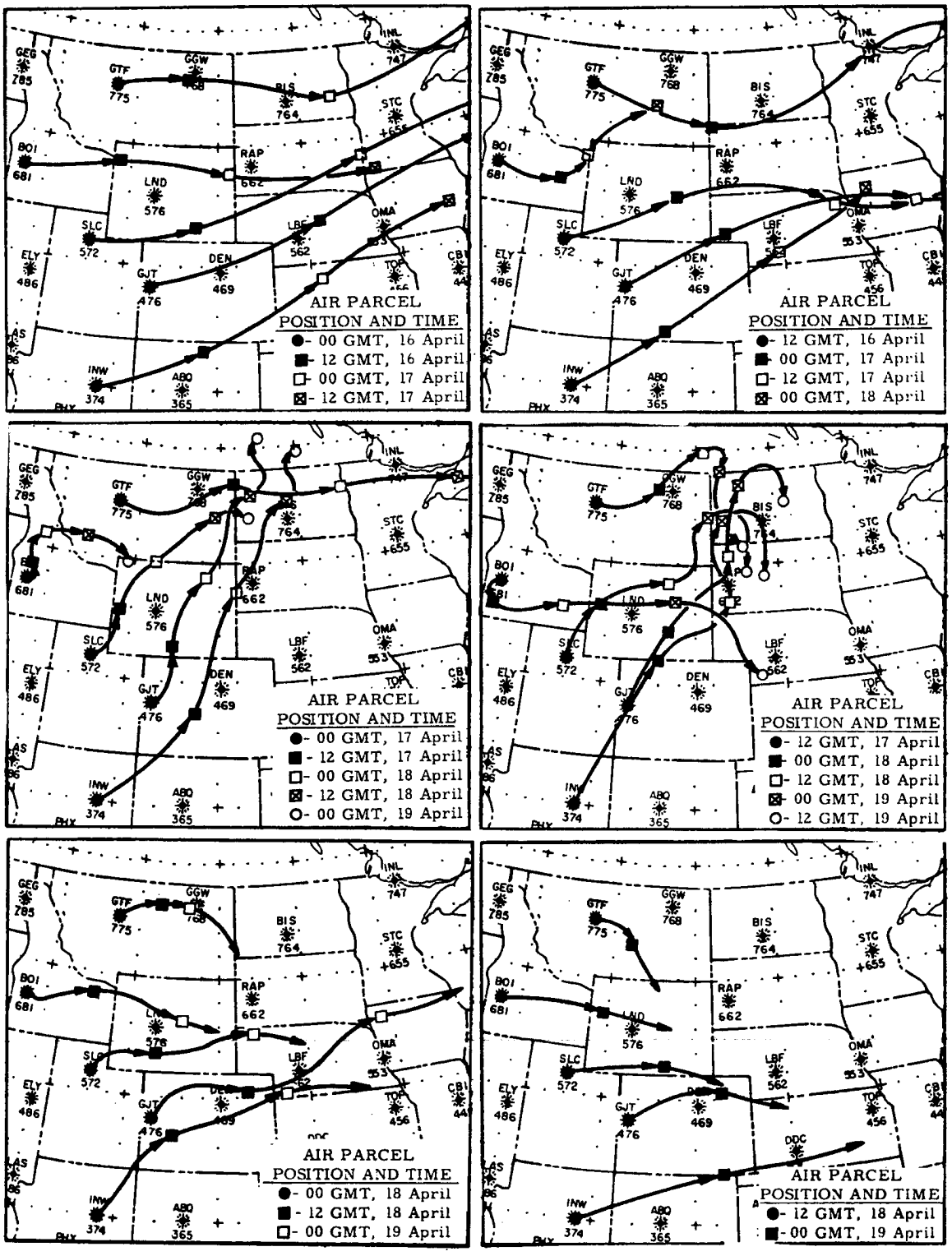

Figure 25. Air parcel trajectories. Calculated 12-hour positions of parcels are shown by the symbols in the legend of each map. The time of origin for each trajectory is the first time given in the legend.

to as far north as Great Falls, Montana, crossed at right angles to the main axis of the Rocky Mountains on all days except 17 April. The trajectories calculated for this day followed a path nearly parallel to the main mountain ridge, as was pointed out earlier in this report, and eventually were entrained in a low pressure system which was moving across Montana. These trajectories represent close approximations to the actual paths followed by air parcels.

Cloud producing moisture contained in the lower levels of the atmosphere is depicted in Figure 26 by the fields of mixing ratio (w) for 700 mb. Comparison of the air parcel trajectories in Figure 25 with the mixing ratio field in Figure 26 gives a good indication of the moisture transport during the period under investigation. On 17 April the air over Montana and Arizona was fairly moist. The moisture advection by the air parcels which originated over Arizona on this day is reflected in the reorientation of the mixing ratio field on 0000 GMT, 18 April. The elongated moisture maximum extending from Arizona into Montana and North Dakota indicates that the air parcels carried the moisture northward across the Great Basin where it merged with a second humid area already existing over Montana. Later on 18 April the flow shifted back to a direction normal to the mountain range and the distribution of mixing ratios over the mountain states closely resembles the one of 17 April. The dryness of the air over Colorado and New Mexico, evident on the 19th, is a reflection of the blocking action of the mountains on low level moisture transport.

Streamlines and isotachs at the 250 mb level for this period are shown in Figure 27. The wind field at the upper level was dominated by a major jet core blowing from west-southwest over Colorado and New Mexico. Secondary wind maxima were also associated with cyclonic flow over the northwestern United States. On 0000 GMT, 16 April the streamline pattern shows the winds crossing normal to the mountains and then turning northward over the Great Plains. Later, as the long wave trough progressed

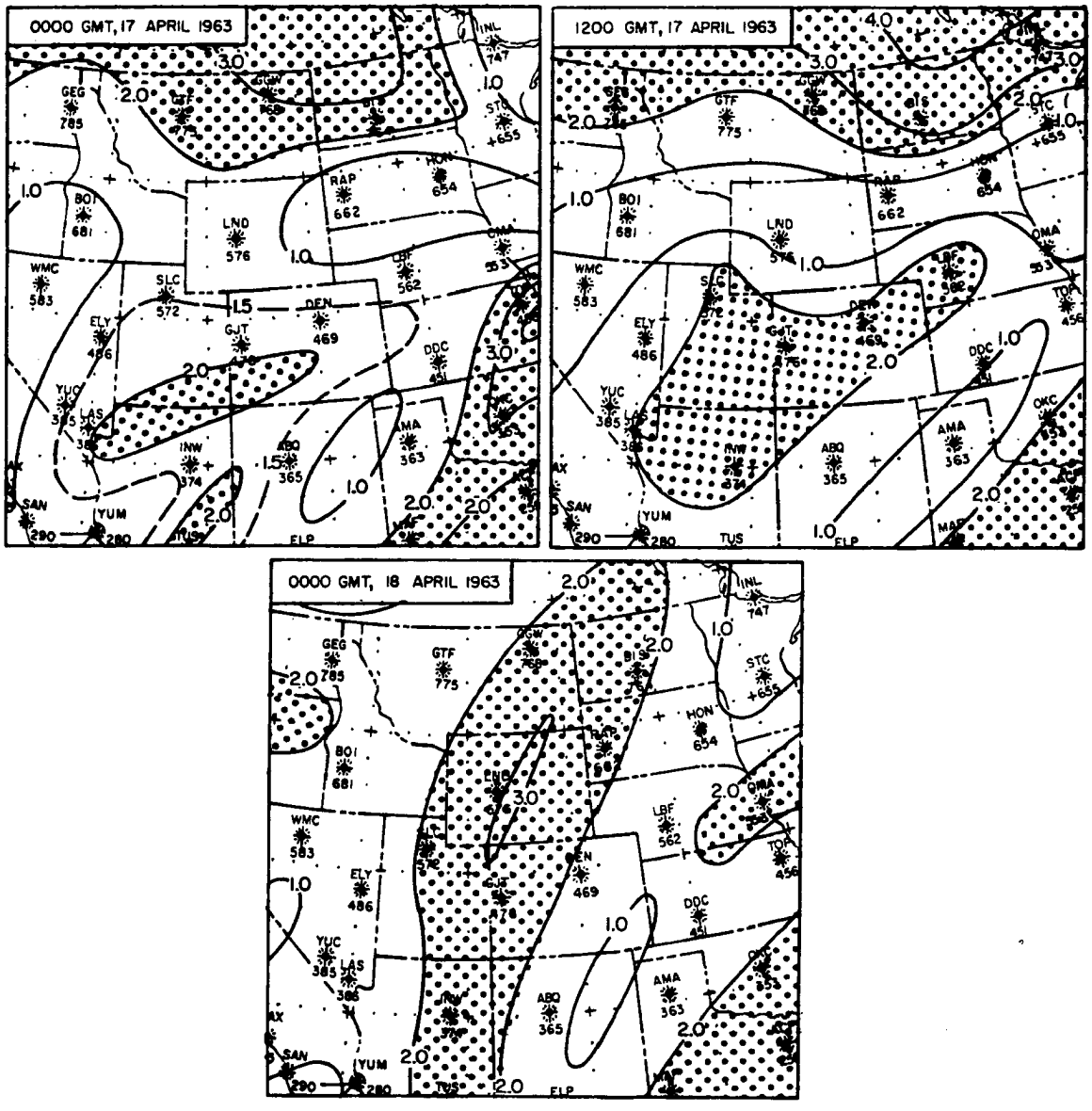

Figure 26. 700 mb mixing ratio (w), (g/kg) for times shown. Dotted areas show mixing ratios > 2 g/kg.

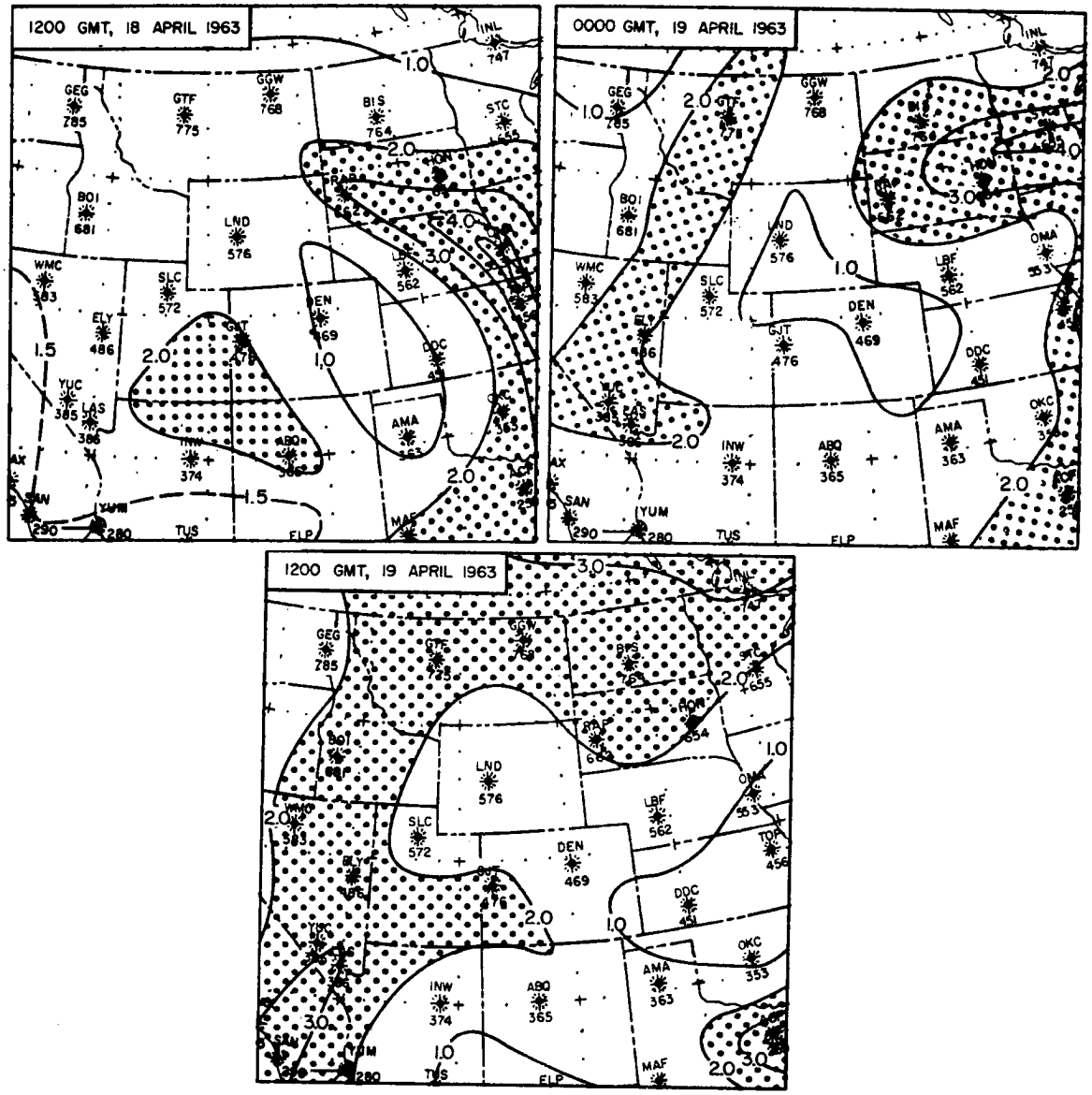

Figure 26. Continued.

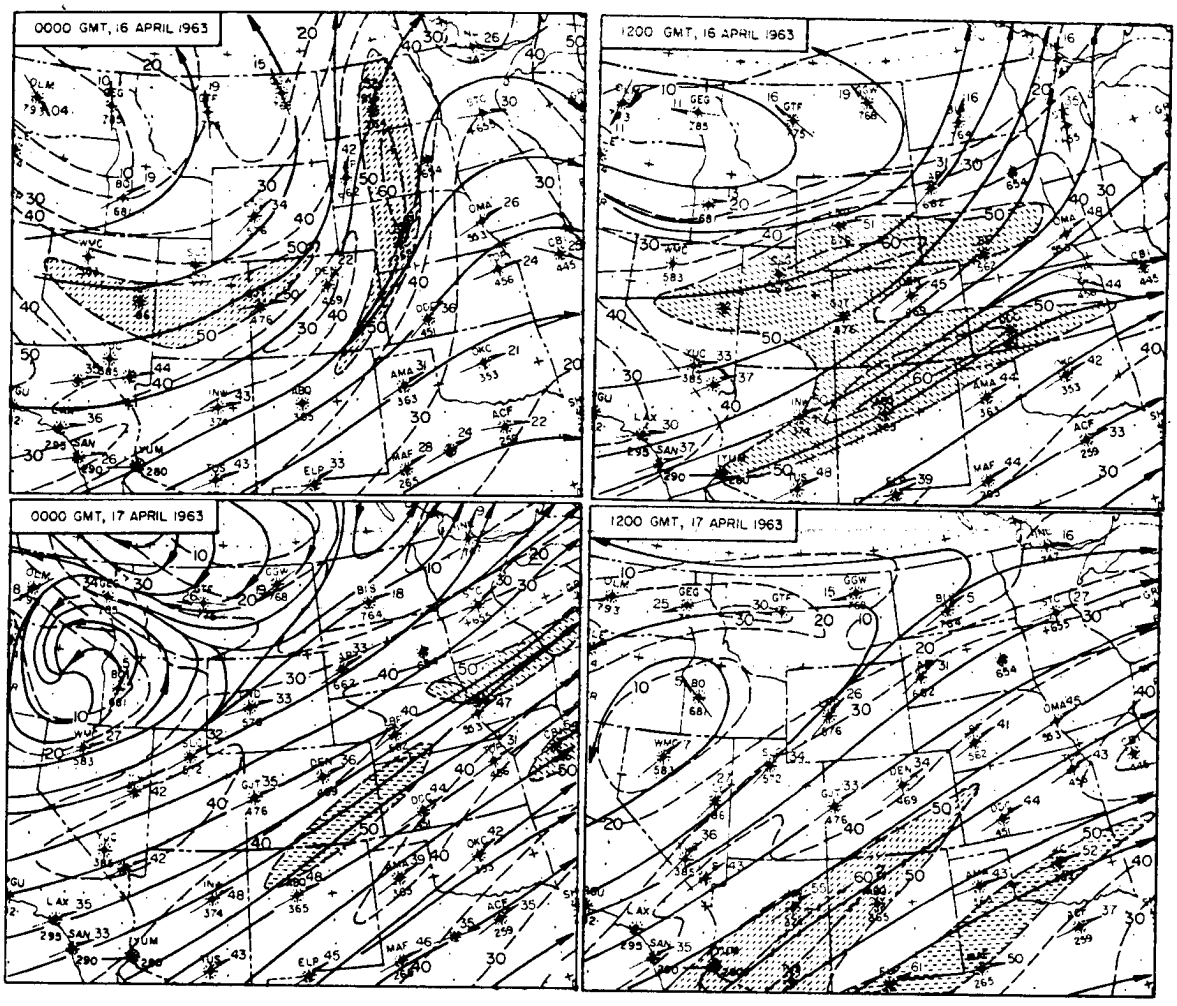

Figure 27. 250 mb streamlines (solid arrows) and isotachs (dashed lines, meters per second) for the times shown. The shaded areas denote wind speeds > 50 mps. The observed wind direction and speed (mps) are shown at the stations.

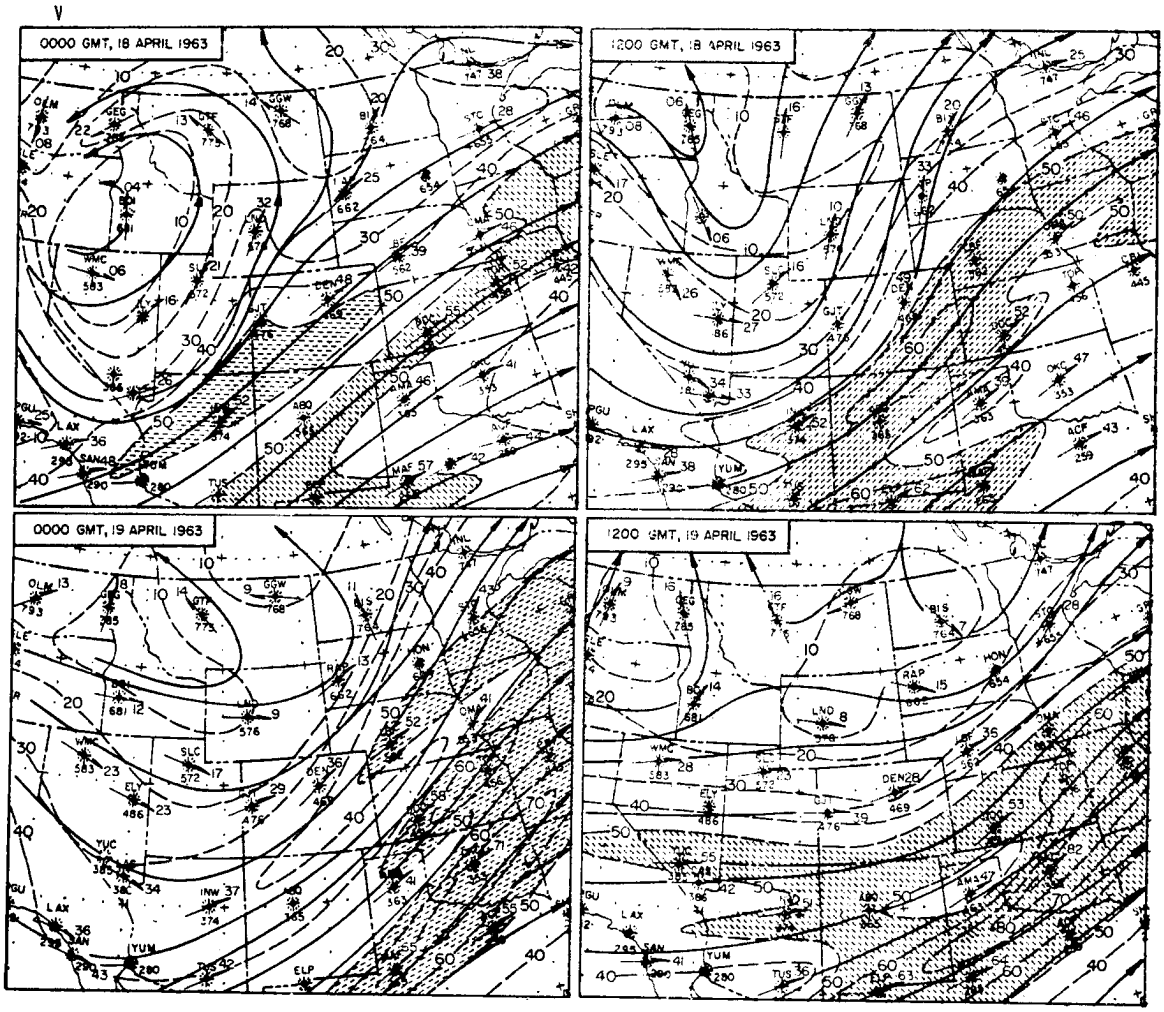

Figure 27. Continued.

eastward, the winds were reoriented into a west-south-westerly direction with a maximum remaining over southern Colorado.

Vorticity and Divergence

Using the isotach analyses and the streamlines from the 700 mb and the 250 mb levels, vorticity and divergence were calculated for the chinook region and a large portion of the surrounding area. To do this a grid network was designed which consisted of points located on 2.5 degree intersections of longitude and latitude, covering an area 20 degrees longitude wide and 17.5 degrees latitude high and centered approximately on Denver, Colorado.

The computation scheme using,

$$D = \nabla_h \cdot \vec{V} = \frac{\partial u}{\partial x} + \frac{\partial v}{\partial y} \qquad (10)$$

for divergence,

$$q = \vec{k} \cdot (\nabla \times \vec{V}) = \frac{\partial v}{\partial x} - \frac{\partial u}{\partial y} \qquad (11)$$

for relative vorticity, and

$$Q = \vec{k} \cdot (\nabla \times \vec{V}) + f = (\frac{\partial v}{\partial x} - \frac{\partial u}{\partial y}) + f \ . \qquad (12)$$

for absolute vorticity was programmed for an IBM 1620 computer. ∇_h is the horizontal Nabla operator, x and y are cartesian coordinates positive east and north respectively, $\vec{V}$ is the total wind vector with the components u and v along the x and y axes; f is the Coriolis parameter. Appendix A gives a complete description of the program and correction factors used to perform the computations.

Figure 28 shows the absolute vorticity (Q) patterns of the 250 mb surface with the maximum wind bands superimposed. In general these patterns are controlled by the distribution of shear and of streamline curvature. The presence of "jet fingers" complicates the vorticity distribution. The Q field produced by the major jet core is shown on 16 April (see Figure 28) where the highest values occur to the cyclonic

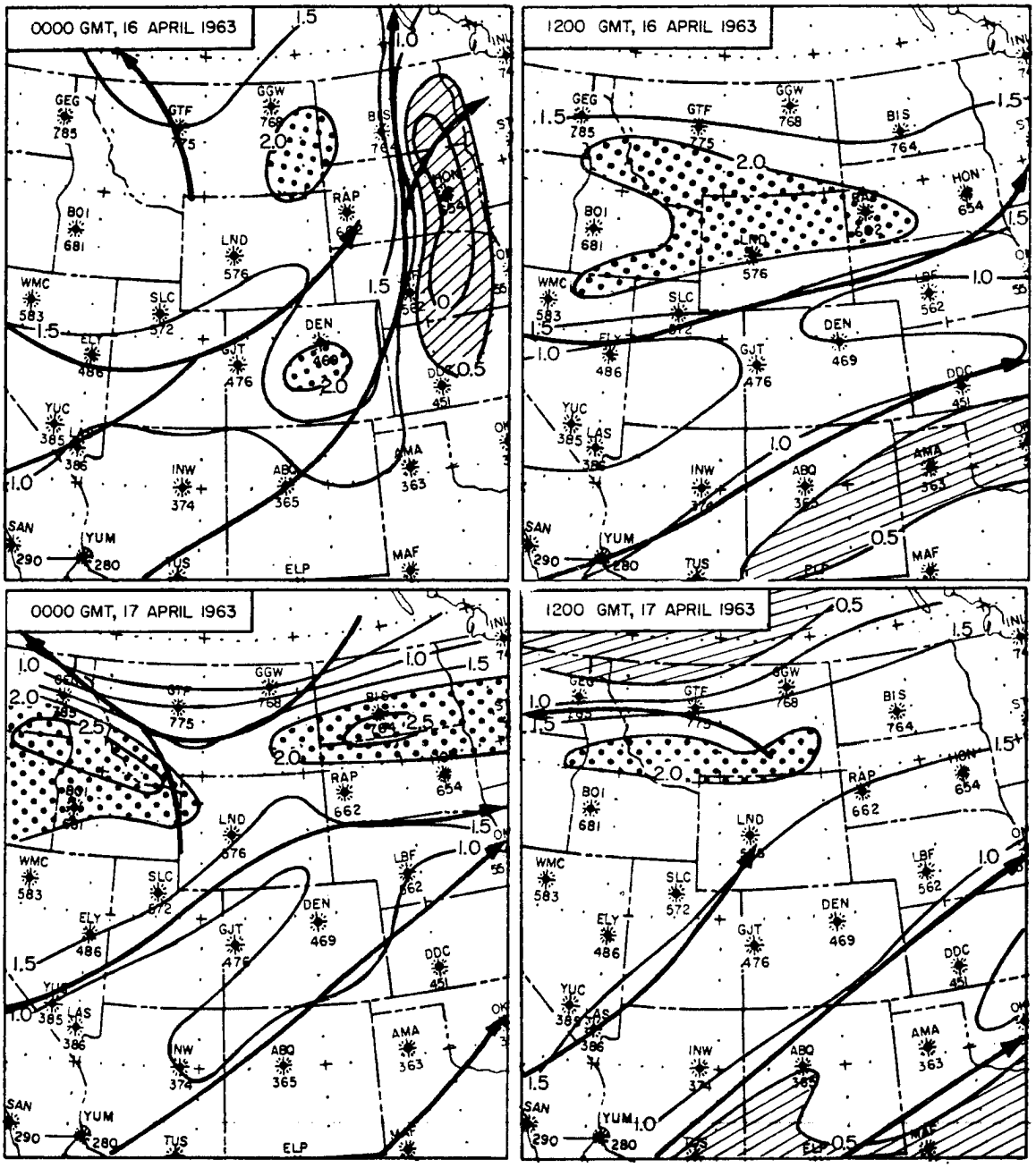

Figure 28. 250 mb absolute vorticity (10^{-4} sec^{-1}) for times shown. Dotted areas show absolute vorticity greater than 2 x 10^{-4} sec^{-1}, cross hatched areas show absolute vorticity less than .5 x 10^{-4} sec^{-1}. The solid arrows are the positions of the jet stream cores.

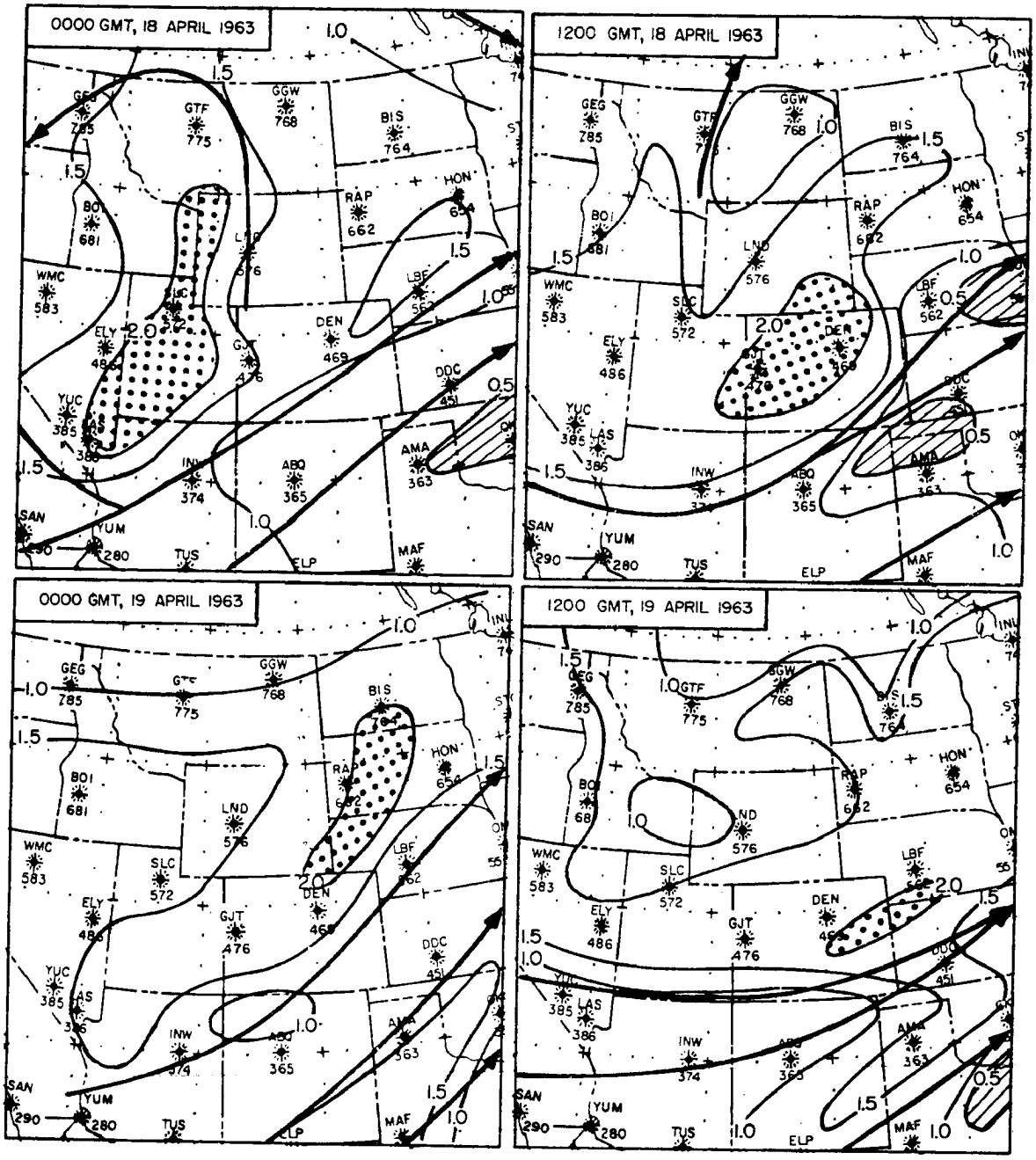

Figure 28. Continued.

side of the northward flowing wind band. Secondary "jet fingers" seem to have little effect on the predominant pattern created by the stronger core. The eastern portion of the area shown in the first chart of Figure 28 contains a small region with $Q < 0$, indicating very strong anti-cyclonic shear associated with the jet stream. On the map of 1200 GMT, 16 April two wind maxima appear. The main Q maximum is associated with the northern branch and the main minimum occurs on the anti-cyclonic side of the southern branch.

The flow pattern becomes more complex on 17 April with an easterly jet appearing over southern Canada. Predominant regions of maximum Q are now shifted northward and appear between the westerly jet to the south and the easterly jet to the north. The juxta-position of the cyclonic sides of these two opposing currents strengthens the values of Q between them. A major region of low Q now appears north of the easterly jet stream where its curvature and shear are anit-cyclonic. On 18 April the presence of an upper level cyclone is indicated by the large area of maximum Q appearing between the two wind bands curving around the low. The area of low Q was again to the south of the main jet axis. On the last day of the period under consideration, the main jet axis is producing a fairly simple Q pattern with maximum values on the cyclonic side and minimum values to the anticylonic side.

Determinations of horizontal mass divergence ($\nabla_h \cdot \vec{V}$) are very sensitive to slight inconsistencies in streamline and isotach analyses, making a field representation of divergence much more difficult than of vorticity. The machine calculations of $\nabla_h \cdot \vec{V}$ gave extreme values of $9 \times 10^{-5} \text{sec}^{-1}$ which appear to be too large for a synoptic-scale pattern. Because of this the analyses in Figure 29 shows areas of divergence and convergence based on sign and not magnitude.

On 0000 GMT, 16 April vorticity advection, represented mathe-matically by

$$- \vec{V} \cdot \nabla_h Q \qquad (13)$$

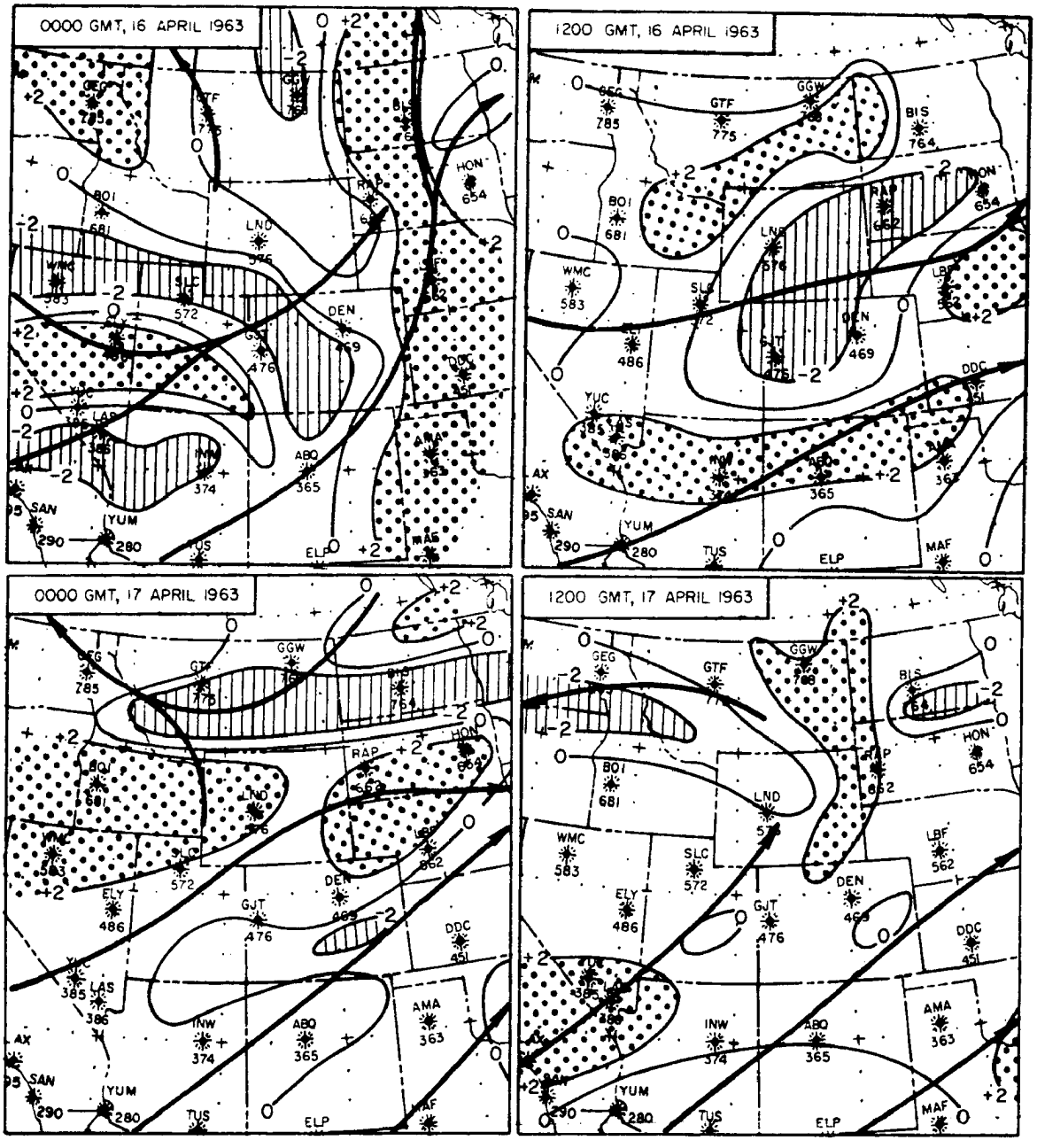

Figure 29. 250 mb mass divergence ($\nabla_h \cdot \vec{V} \times 10^{-5}$ sec^{-1}) for times shown. Dotted areas show divergence > 2×10^{-5} sec^{-1}, cross hatched areas show convergence < -2×10^{-5} sec^{-1}. Solid arrows represent jet stream cores.

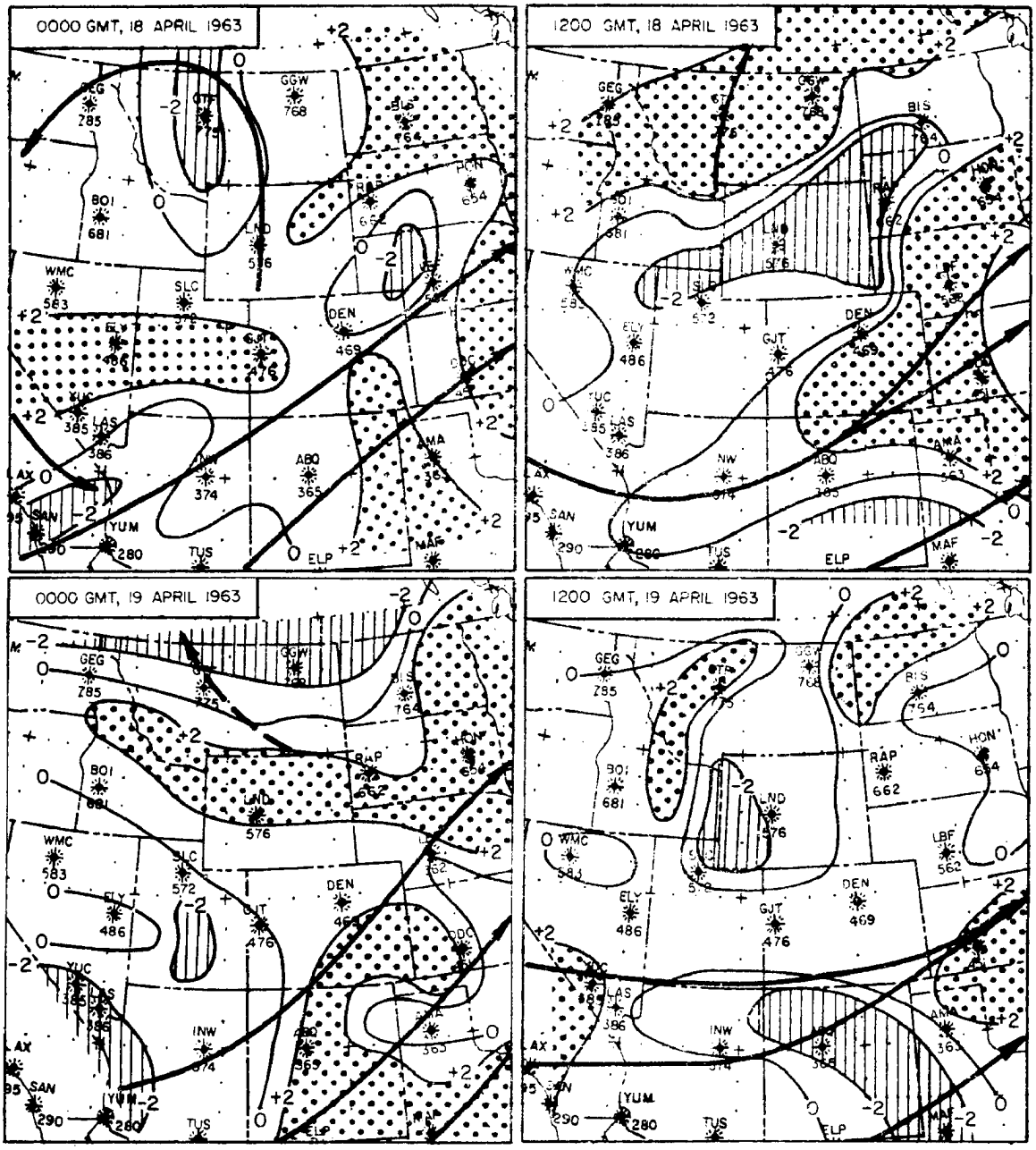

Figure 29. Continued.

has produced a strong divergence region on the front left quadrant and the rear right quadrant of the wind maximum associated with the major jet stream. This pattern is shown on the right side of the first chart in Figure 29. The region of strong divergence near the confluence of the two wind bands on the left side of the map for 0000 GMT, 16 April is caused by a marked increase in velocity in this area. On 0000 GMT, 17 April the major areas with divergence are still associated with the strong jet which is crossing the Rockies from southwest to northeast. At this time the merging of the easterly jet with a southerly branch originating over California produces convergence over Montana. At 1200 GMT, 18 April another strong divergence region appears over eastern Colorado and Nebraska, probably produced by vorticity advection on the north side of the major jet axis. The $\nabla_h \cdot \vec{V}$ fields at 250 mb during the remainder of the investigated period are less pronounced.

The absolute vorticity distributions (Q) at the 700 mb level are shown in Figure 30. The 16 April maps reveal a region of strong Q to the cyclonic side of the major wind band and a large area of weak Q located to the anticyclonic side. The only complicating influence during this time is the existence of a double wind maximum flowing along parallel paths. The minimum Q area which is shown at 1200 GMT, 16 April is interrupted by a small area of stronger Q just north of the southernmost wind band. The vorticity pattern becomes still more complex later in the period when clearly defined regions of maximum velocity are difficult to identify.

The low pressure area over Wyoming on 18 April, described in a previous chapter, coincides with a region of strong Q shown in Figure 30. It was suggested earlier that this low may have been partially formed by conservation of potential vorticity in the flow over the mountains. The shape of the maximum Q field shown on the map for 1200 GMT, 18 April follows the general outline of the Continental Divide, lending further support to the suggestion that this strong Q area was caused by the orientation of the mountains and the strong wind band which crossed the Rockies.

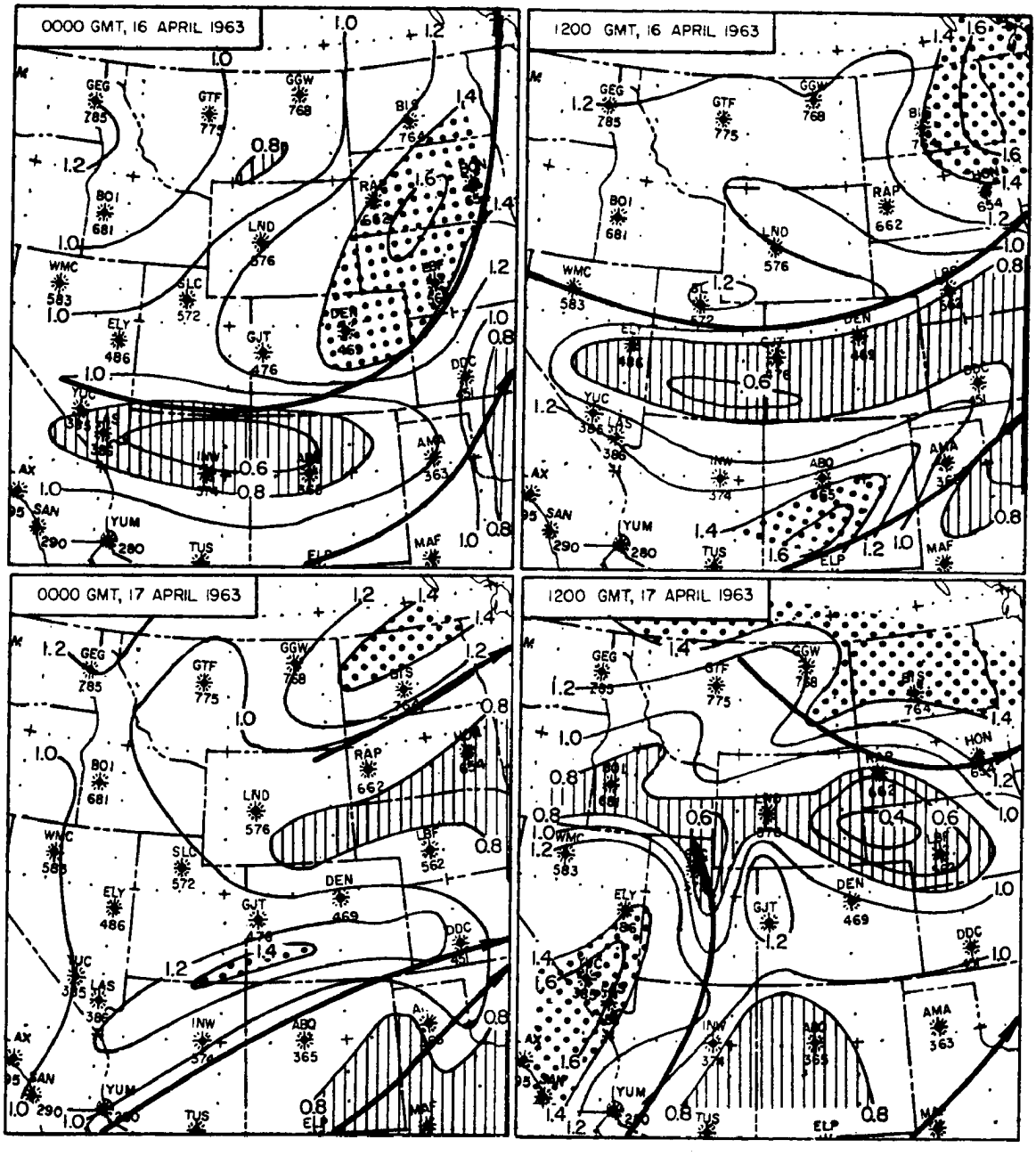

Figure 30. 700 mb absolute vorticity (Q, 10^{-5} sec^{-1}, solid lines) for times shown. Dotted areas show $Q > 1.4 \times 10^{-5}$ sec^{-1}, cross hatched areas show $Q < 0.8 \times 10^{-5}$ sec^{-1}. Heavy arrows are 700 mb wind maximum cores.

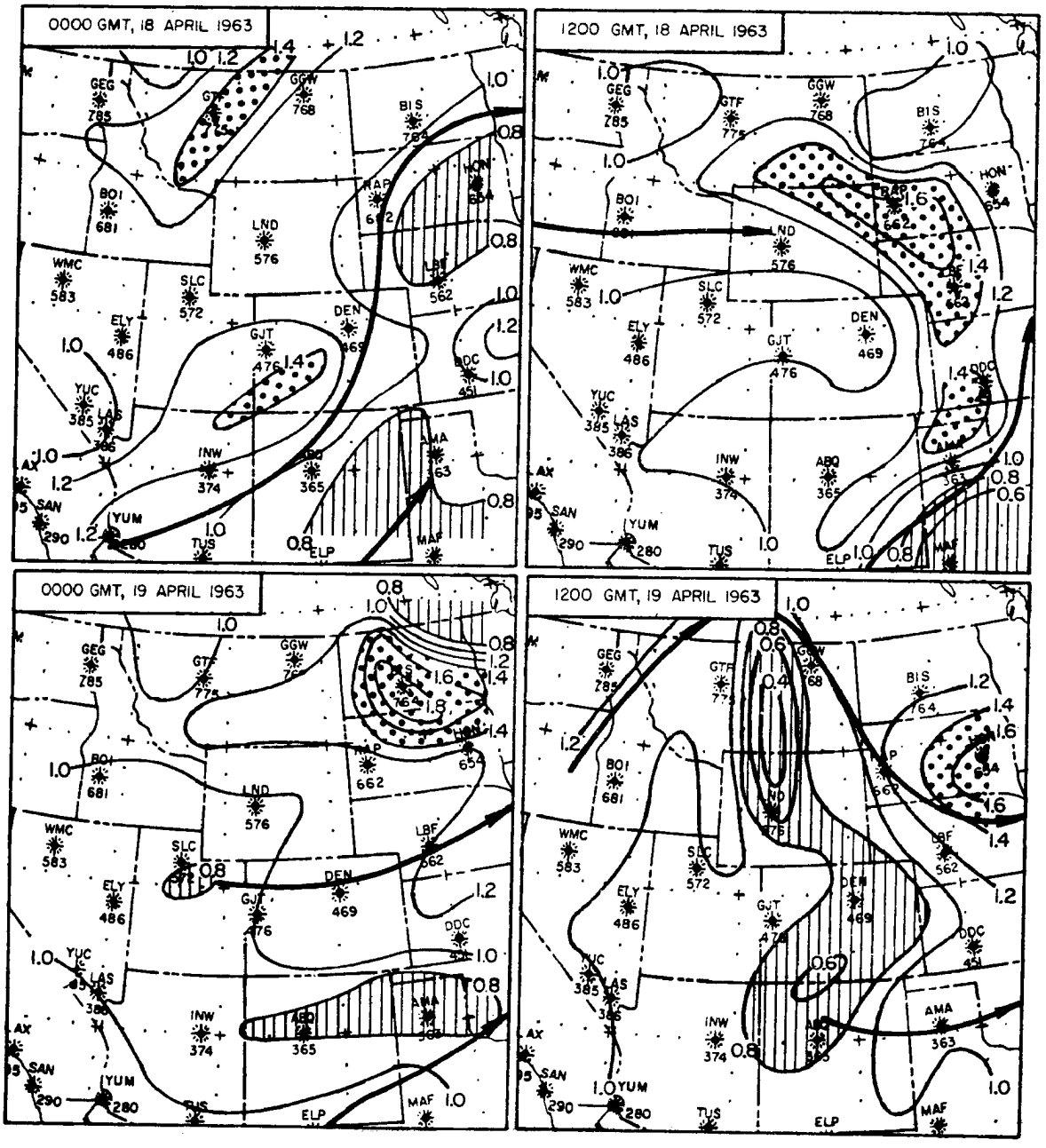

Figure 30. Continued.

On 1200 GMT, 19 April the same area was dominated by a weak Q field resulting from anticyclonic curvature.

The divergence patterns at the 700 mb level (see Figure 31) were less pronounced than those which occurred at 250 mb. This is to be expected as $\nabla_h \cdot \vec{V}$ at lower levels in this region was influenced by the mountainous terrain. Early on 16 April the parallel wind bands were merging over the great plains region of eastern Colorado creating an area of convergence (see Figure 31). Later on that same day the wind bands were further apart and the convergence, appearing on the cyclonic side of the northern wind band, intensified and moved south. By 17 April vorticity advection again was controlling the $\nabla_h \cdot \vec{V}$ pattern. The area of divergence located over the Great Basin and extending into southeastern Colorado was associated with the rear right quadrant of the northern wind band and the front left quadrant of the southern wind maximum.

The sequence of events which occurred on 18 April cannot be described by the wind field alone. At 0000 GMT, 18 April a small ridge was present just to the lee of the Rocky Mountains. There was a large concentration of convergence centered on the inflection point of the streamlines. As the ridge was displaced eastward, the area of convergence was replaced by an equally strong divergence field. This rapid change of pattern might have its cause in the blocking effect of the high mountains. Vorticity advection associated with the ridge in its 0000 GMT position should produce divergence; however, the general upward slope of the mountains in this area would produce orographic lifting and convergence. The effect of topography may thus have been predominant in the observed vergence pattern. After the ridge progressed eastward over the Great Plains, the underlying terrain had a general downward slope which caused mass divergence. The combination of vorticity advection and orographically induced divergence then complemented each other and a region of strong divergence appeared. The analyzed patterns of 18 April in Figure 31 support this hypothesis.

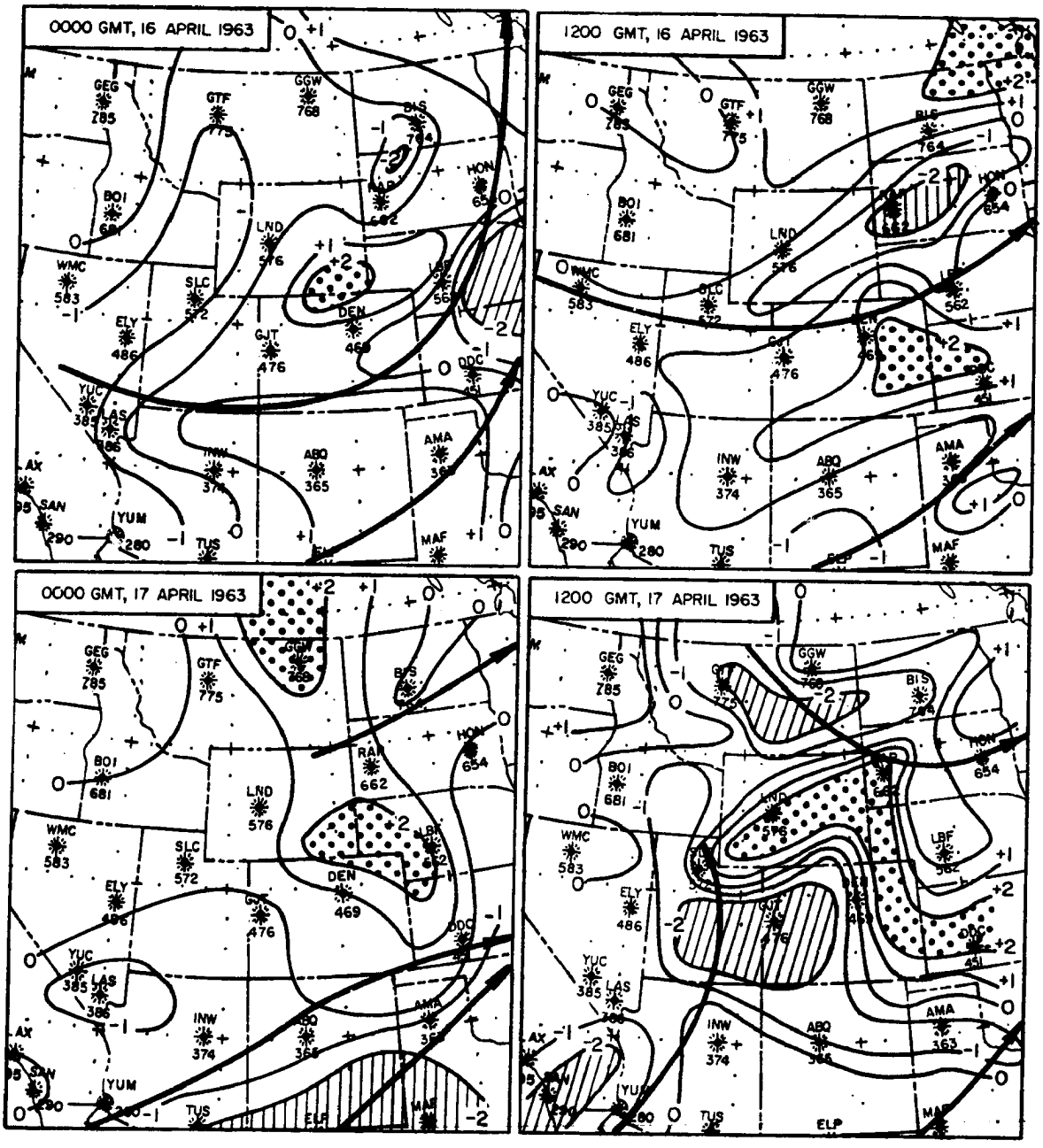

Figure 31. 700 mb mass divergence ($\nabla_h \cdot \vec{V} \times 10^{-5}$ sec^{-1}, solid lines) for times shown. Dotted areas show divergence > 2×10^{-5} sec^{-1}, cross hatched areas show convergence < -2×10^{-5} sec^{-1}. Heavy arrows are 700 mb maximum wind cores.

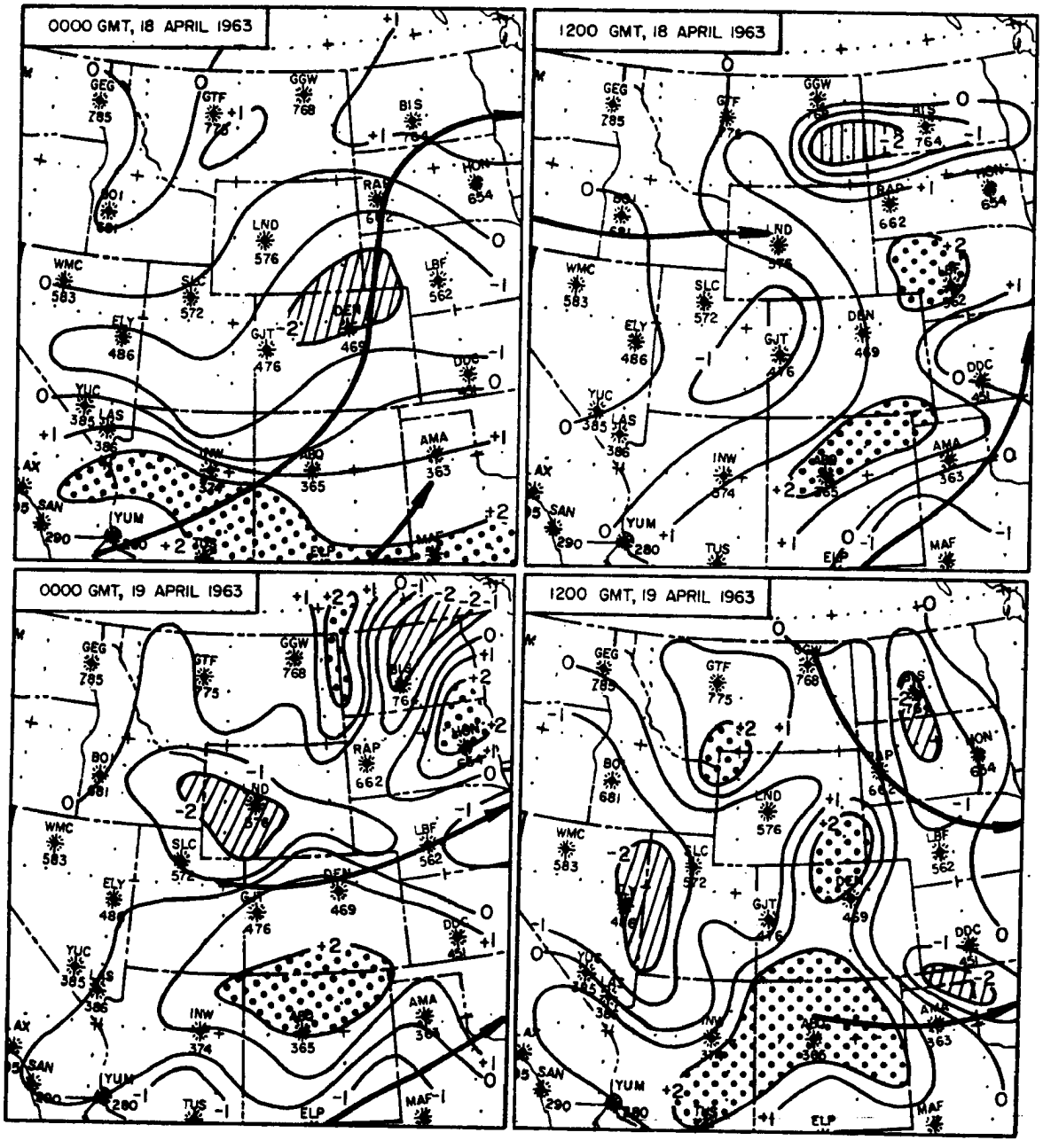

Figure 31. Continued.

To gain a more complete picture of flow over the mountains, and in particular to assess the parameters producing cloudiness as observed by TIROS, divergence of moisture flux given by

$$\nabla_h \cdot \vec{V} w = w \nabla_h \cdot \vec{V} + \vec{V} \cdot \nabla_h w = \frac{\partial uw}{\partial x} + \frac{\partial vw}{\partial y} \qquad (14)$$

was calculated. The same grid network used for the previous calculation was applied and a program for the IBM 1620 computer prepared. Details of the calculations appear in Appendix A of this report. The patterns of moisture flux which were obtained from these calculations are shown in Figure 32. A comparison with Figure 31 shows that the moisture divergence is essentially controlled by the field of velocity divergence, and only to a lesser degree by variations in mixing ratio (w).

Vertical Structure

The jet stream and the strong baroclinic zone beneath it control the surface weather and cloud patterns appearing in TIROS photographs. A correlation of vergence patterns at the jet stream level with those at low levels was, therefore, sought.

Dines' compensation principle states that the divergence must change its sign at least once in any air column extending from sea level to the top of the atmosphere in such a manner that the net divergence is small. A level of non-divergence is usually found near 500 or 600 mb; therefore, if the compensation principle holds, divergence at the 250 mb level should be compensated by convergence near 700 mb. This, of course, is a rather simplified assumption, applying only to strongly developed weather situations. Comparing the derived quantities of divergence for 250 mb (see Figure 29) with those at the 700 mb level (see Figure 31), fairly good relationships are evident despite the orographic effects. At 0000 GMT, 16 April the divergence regions associated with the strong jet stream on the right side of the 250 mb map overlie a small center of low level convergence near Bismarck, North Dakota, and a more intense convergence area centered over Omaha, Nebraska. Vertical compensation

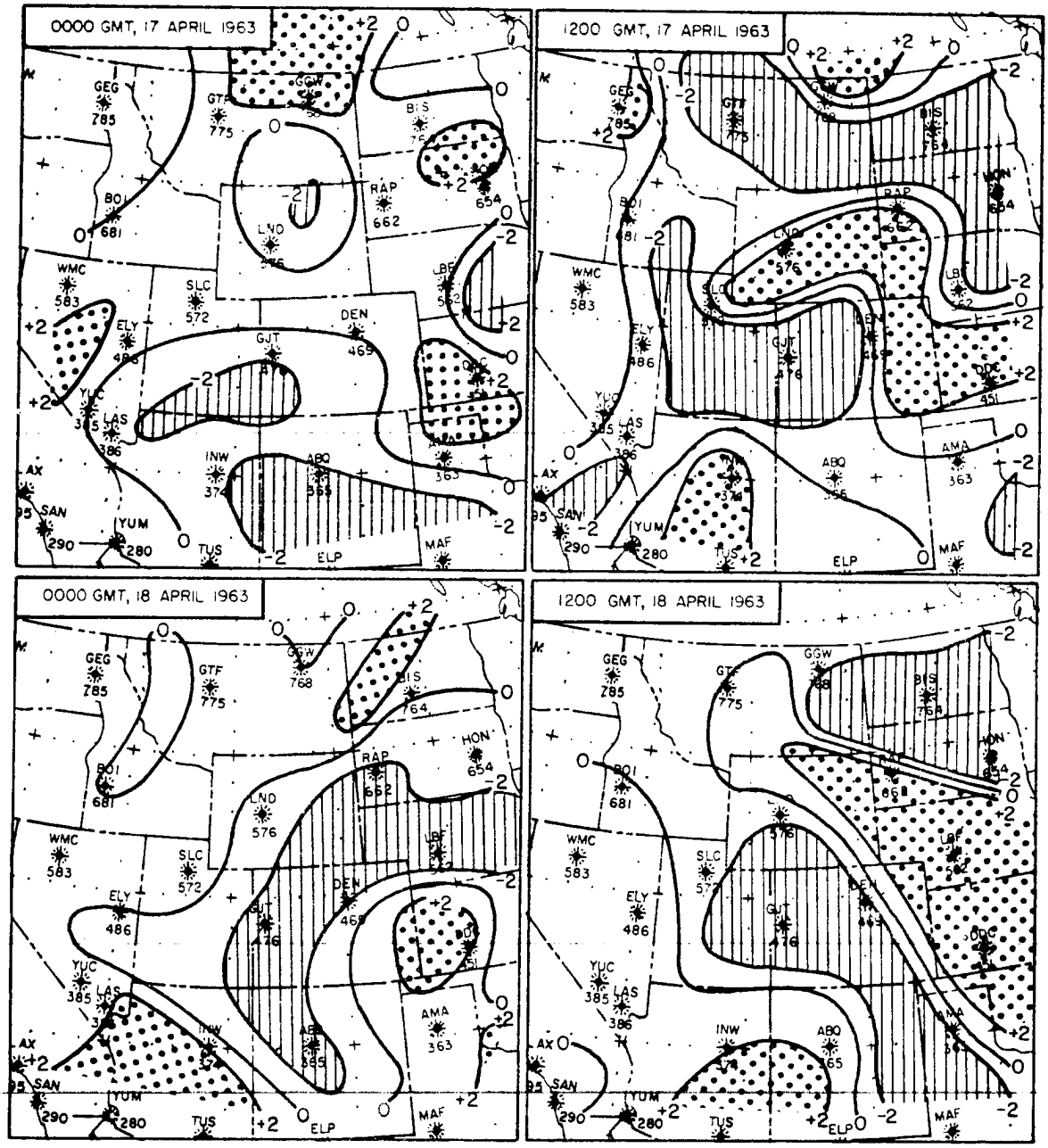

Figure 32. 700 mb divergence of moisture flux ($\nabla_h \cdot \bar{\bar{V}} w \times 10^{-8}$ sec^{-1}) for times shown. Dotted area shows divergence > 2×10^{-8} sec^{-1}, cross hatched area shows convergence < -2×10^{-8} sec^{-1}.

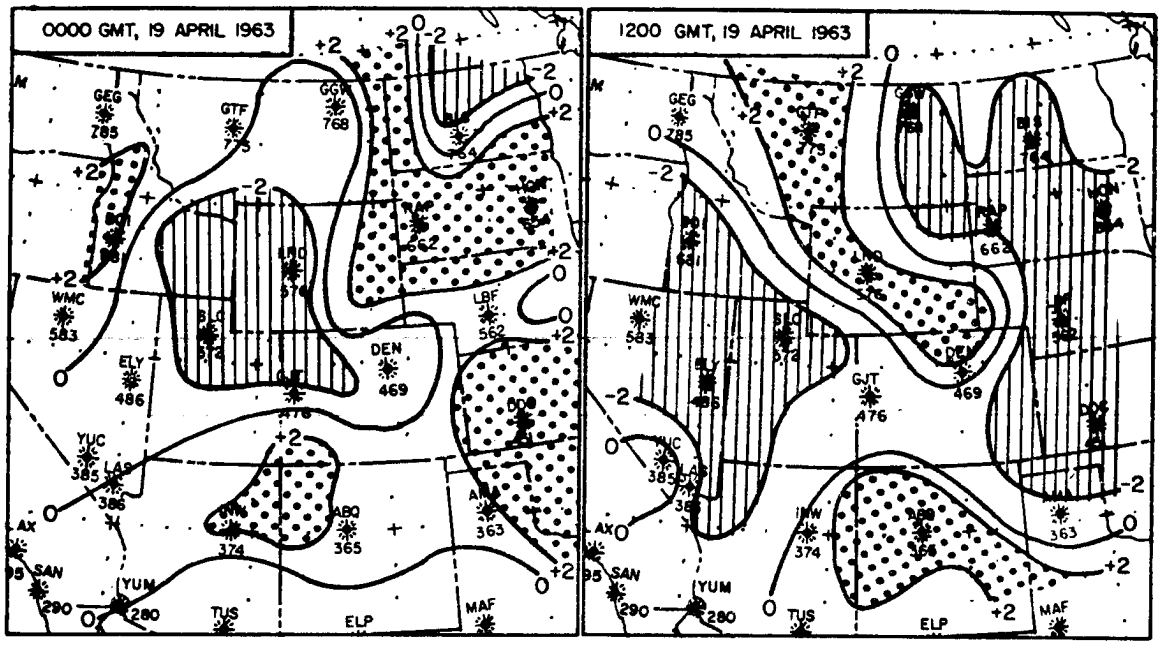

Figure 32. Continued.

of divergence over the mountains is not as well established at this time. However, the upper level convergence over Denver, Colorado, seems to be superimposed upon the two areas of divergence north and south of Denver at the 700 mb level. Later on 16 April the patterns shift and two divergent layers seem to overlie each other. This case and others where divergence or convergence occur at both levels in the same area are probably due to the limited vertical resolution of the computations.

The effect of the mountains on the divergence patterns at 700 mb on 18 April was discussed earlier. This same effect could be responsible for the poor correlation between patterns at 250 mb and 700 mb. The seemingly disorganized centers at 250 mb show convergence occurring between Denver, Colorado, and North Platte, Nebraska. At 700 mb in the same region, there is a zone of strong convergence which has previously been explained by mountain effects. Again, more complete analyses including several pressure levels would be necessary to determine where the compensation for this strong convergence occurred.

Cloud Patterns and Derived Quantities

In order to estimate the effect of mass and moisture divergence on cloud formation as observed by TIROS, the analyses described earlier were superimposed upon TIROS photographs. This procedure eliminated prospective distortion in the TIROS pictures. Unfortunately, most of the orbit times for the pictures used in this study occurred midway between standard radiosonde ascents. If the field which was to be correlated with the TIROS picture were changing rapidly with time, a composite of the two map times which were nearest the picture was prepared by averaging the analyzed fields. On the other hand, if the flow were reasonably steady and there were no large changes between the maps on either side of the TIROS picture, the nearest standard observation time was used for the comparison.

Figure 33 a shows a picture from orbit 3084 D of TIROS VI taken over the central Rocky Mountains. The bright region in this photograph

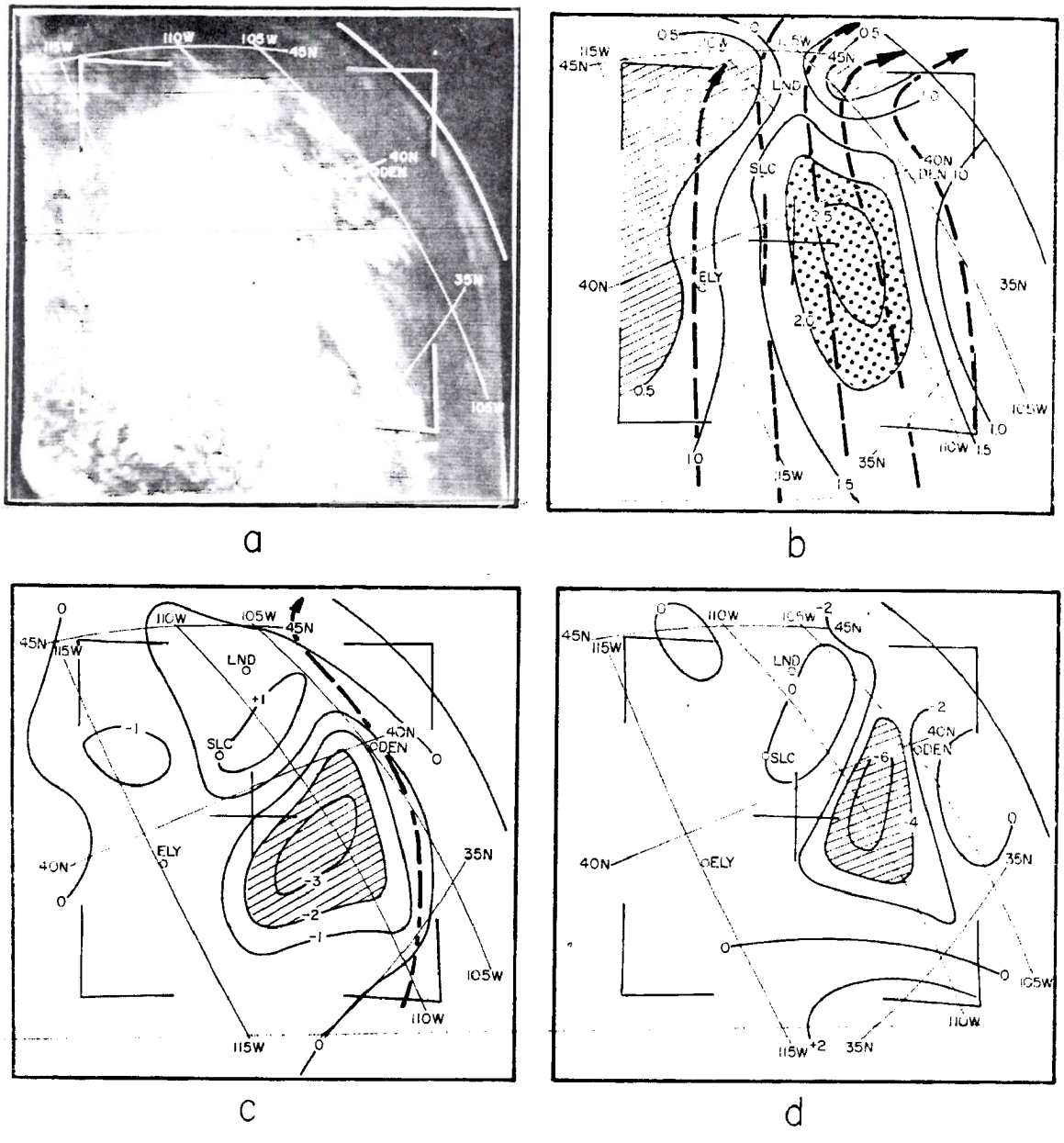

Figure 33. (a) TIROS VI orbit 3084 D frame 15 valid at 1900 GMT, 17 April 1963. (b) 700 mb mixing ratio (w, g/kg, solid lines) superimposed on rectified TIROS grid. Dotted area shows w > 2.0 g/kg, cross hatched area shows w < 0.5 g/kg. Dashed arrows are 700 mb streamlines. (c) 700 mb mass divergence (10^{-5}/sec, solid lines). Dotted area shows divergence > 2 x 10^{-5}/sec, cross hatched area shows divergence < -2 x 10^{-5}/sec. Dashed line is core of maximum 700 mb wind. (d) 700 mb divergence of moisture flux (10^{-8}/sec). Dotted area shows divergence > 4 x 10^{-8}/sec, cross hatched area shows convergence < -4 x 10^{-8}/sec. Charts b, c and d are a composite of the analyses valid at 1200 GMT, 17 April and 0000 GMT, 18 April 1963.

could be classified as cloud, although during April the possibility of snow cover on the mountains must be kept in mind. The field of mixing ratio (w) shown in Figure 33 b agress well with this bright area and thus supports the possibility of cloud formation. Orographic lifting can be discounted as a dominant mechanism, except in isolated areas, since the streamlines in Figure 33 are parallel to the main ridge of the mountains. The 700 mb $\nabla_h \cdot \vec{V}$ field (see Figure 33 c) suggests a lifting mechanism by low level convergence which may be held responsible for cloud production. There is a small divergence center east of Salt Lake City, Utah (SLC). Referring again to the TIROS picture, there appears a clear area south of Lander, Wyoming (LND), and west of SLC which is associated with this divergence area shown on the analysis. The divergence of moisture flux ($\nabla_h \cdot \vec{V} w$) shown in Figure 33 d also agress well with the cloud distribution seen by TIROS. This pattern is very similar to the one just discussed, the differences being caused by areas of high humidity. In both the mass divergence field and the moisture flux field, the strongest convergence is shifted slightly to the east of the densest cloud area. Since these fields were prepared by averaging the two synoptic maps nearest to the picture time, such a small discrepancy is not surprising.

Figure 34 shows a portion of the same cloud pattern from a different angle taken seconds later and farther to the east. The distortion caused by viewing at a new angle is apparent when the area around Lander, Wyoming (LND), is compared in Figures 33 and 34. The dendritic shape of the bright area at 45° N latitude and 110° W longitude is good evidence that we are seeing the mountain snow fields in northwestern Wyoming. Further to the east there is a crescent shaped band near the intersection of the cold front and 45° N latitude. This band is easily identified as snow cover on the Big Horn Mountains of Wyoming. Again, the high values of mixing ratio are associated with the cloudy regions south of LND. There is a second concentration of moisture north of the

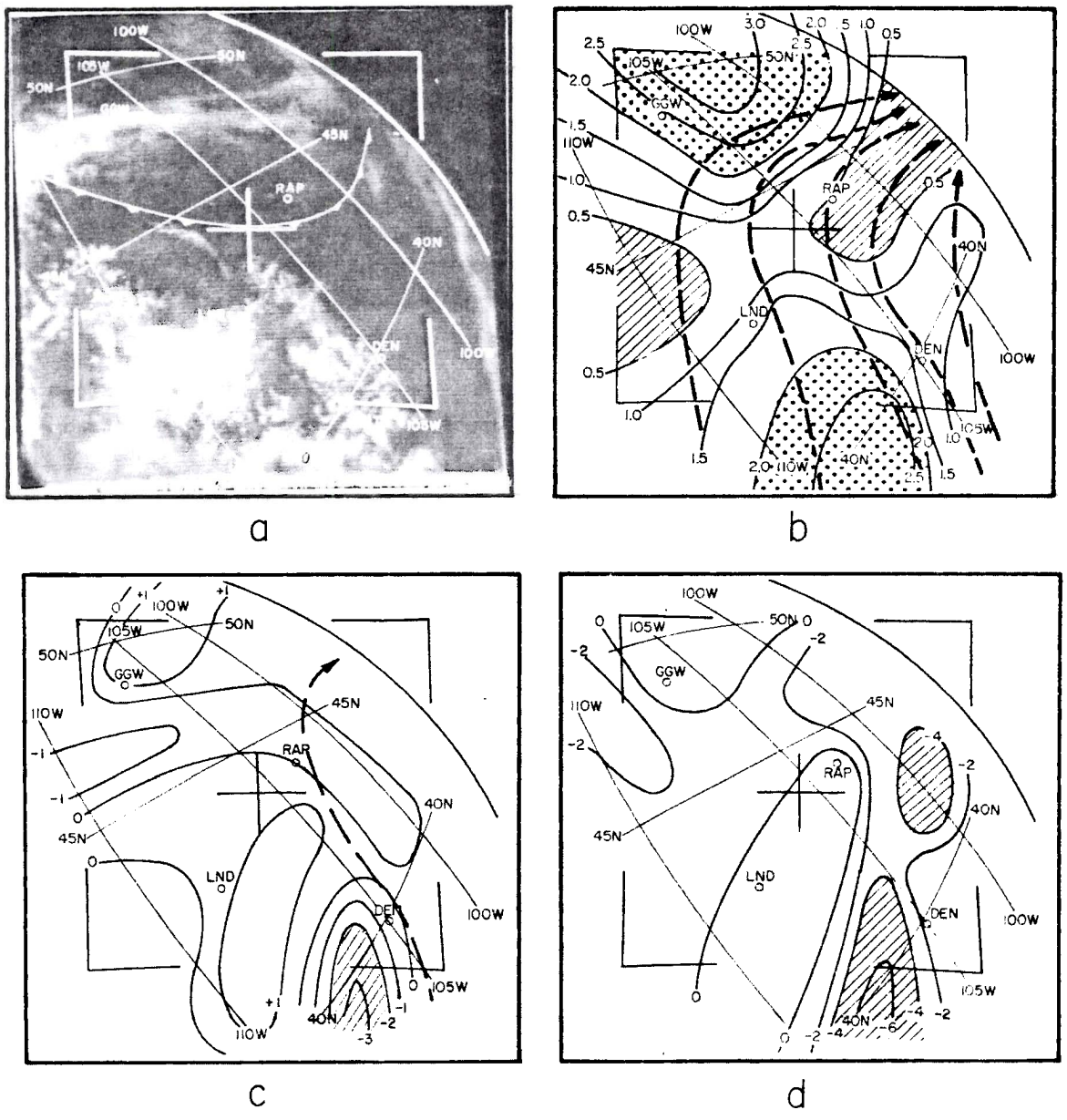

Figure 34. (a) TIROS VI orbit 3084 D frame 25 valid at 1902 GMT, 17 April 1963. (b) 700 mb mixing ratio (w, g/kg, solid lines) superimposed on rectified TIROS grid. Dotted area shows w > 2.0 g/kg, cross hatched area shows w < 0.5 g/kg. Dashed arrows are 700 mb streamlines. (c) 700 mb mass divergence (10^{-5}/sec, solid lines). Dotted area shows divergence > 2 x 10^{-5}/sec, cross hatched area shows convergence < -2 x 10^{-5}/sec. Dashed line is core of maximum 700 mb wind. (d) 700 mb divergence of moisture flux (10^{-8}/sec). Dotted area shows divergence > 4 x 10^{-8}/sec, cross hatched area shows convergence < -4 x 10^{-8}/sec. Charts b , c , and d are a composite of the analyses valid at 1200 GMT, 17 April and 0000 GMT, 18 April 1963.

cold front. The clouds to the north and parallel to the front are probably caused by lifting motions over the cold air mass. There is also a good correlation between the direction of this northern cloud band and the streamline pattern shown in Figure 34 b . The 700 mb divergence and moisture flux shown in Figures 34 c and 34 d do not agree very well with the cloud formations associated with the front. This may be due to the averaging method used to derive the fields which are superimposed on the TIROS grid.

Frame 18 from TIROS V orbit 4349 T (Figure 35) was taken over the southwestern United States and shows only the southern portion of the mountain region of interest. The brigh area north of Albuquerque, New Mexico (ABQ), may signify clouds, although the broken pattern bears resemblance to snow covered mountains and open valleys. The analysis of mixing ratio at 700 mb (see Figure 35 b) lends inconclusive evidence for this. A dry tongue extends from north of Grand Junction, Colorado (GJT), to Denver, Colorado (DEN); however, the air over the remaining bright area in the TIROS photograph contains enough moisture to produce clouds if the proper lifting mechanism were present. The streamlines (see Figure 35 b) indicate that the flow was normal to the main ridge of the mountains which would bring about orographic lifting. The divergence pattern at 700 mb (see Figure 35 c) suggests that there would be very little support for cloud production from the upper flow as a strong divergence center appears over the bright area in the Picture. The moisture flux shown in Figure 35 d also reveals the large center of divergence just mentioned; however, there was a small center of moisture convergence further to the north which did not appear in the $-\nabla_h \cdot \vec{V}Q$ pattern. Unfortunately, this area of moisture convergence was near the edge of the picture. Therefore, it was difficult to draw meaningful conclusions about the cloud pattern with which it might be associated. If the brigh area were produced by clouds and not snow, then the generating force could only be orographic lifting. The predominance of terrain effects on cloud formation, if indeed the brigh area in the photograph is caused by clouds and not snow, may explain the detailed structure of this pattern which could be revealing the mountain valleys.

A later frame from TIROS V orbit 4349 T is shown in Figure 36. Here we get a much clearer picture of what was occurring near the surface. The

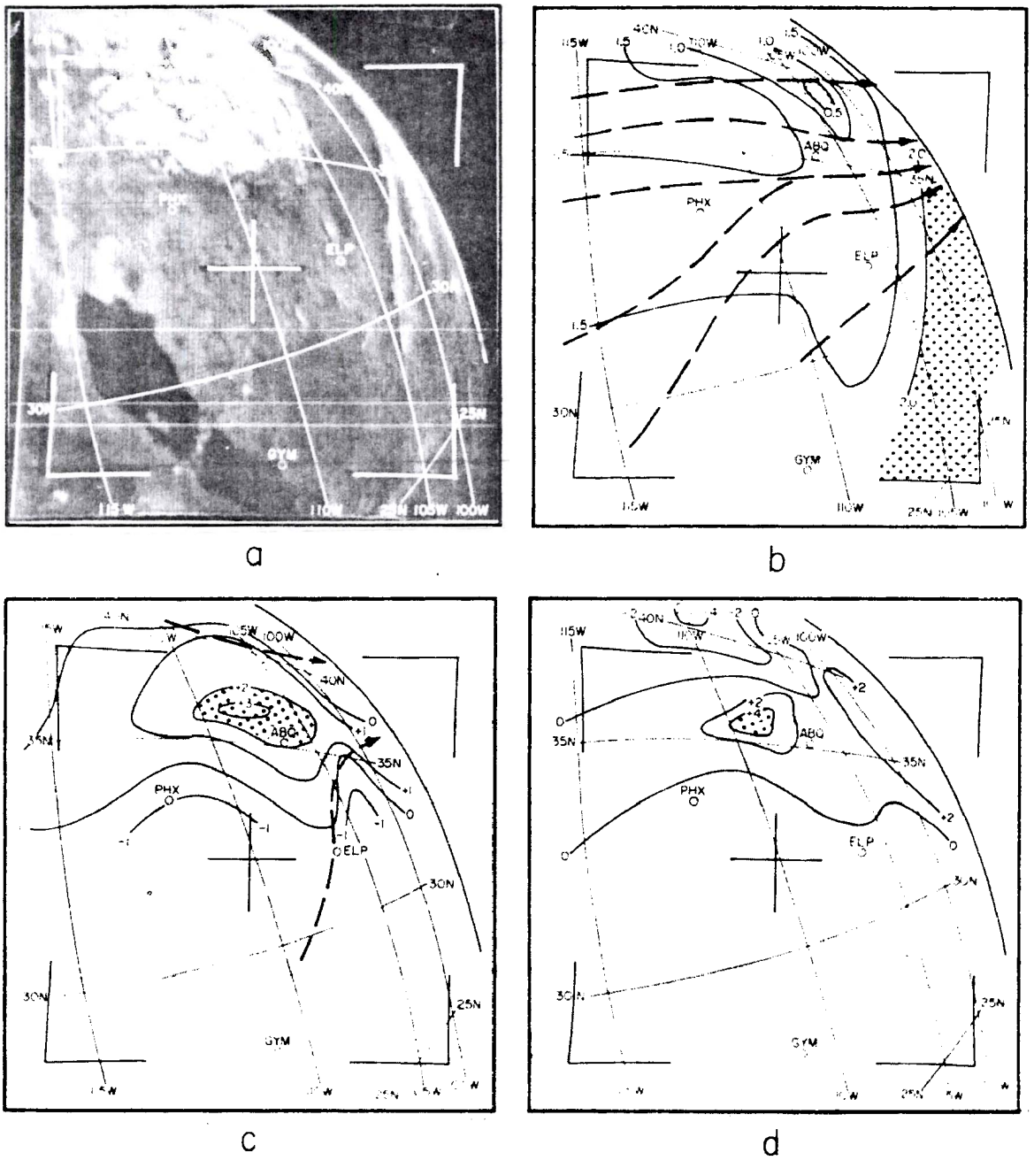

Figure 35. (a) TIROS V orbit 4349 T frame 18 valid at 1953 GMT, 18 April 1963. (b) 700 mb mixing ratio (w, g/kg, solid lines) superimposed on rectified TIROS grid. Dotted area shows w > 2.0 g/kg, cross hatched area shows w < 0.5 g/kg. Dashed arrows are 700 mb streamlines. (c) 700 mb mass divergence (10^{-5}/sec, solid lines). Dotted area shows divergence >-2 x 10^{-5}/sec. Dashed line is core of maximum 700 mb wind. (d) 700 mb divergence of moisture flux (10^{-8}/sec). Dotted area shows divergence > 4 x 10^{-8}/sec, cross hatched area shows convergence < -4 x 10^{-8}/sec. Charts b , c , and d are valid at 0000 GMT, 19 April 1963.

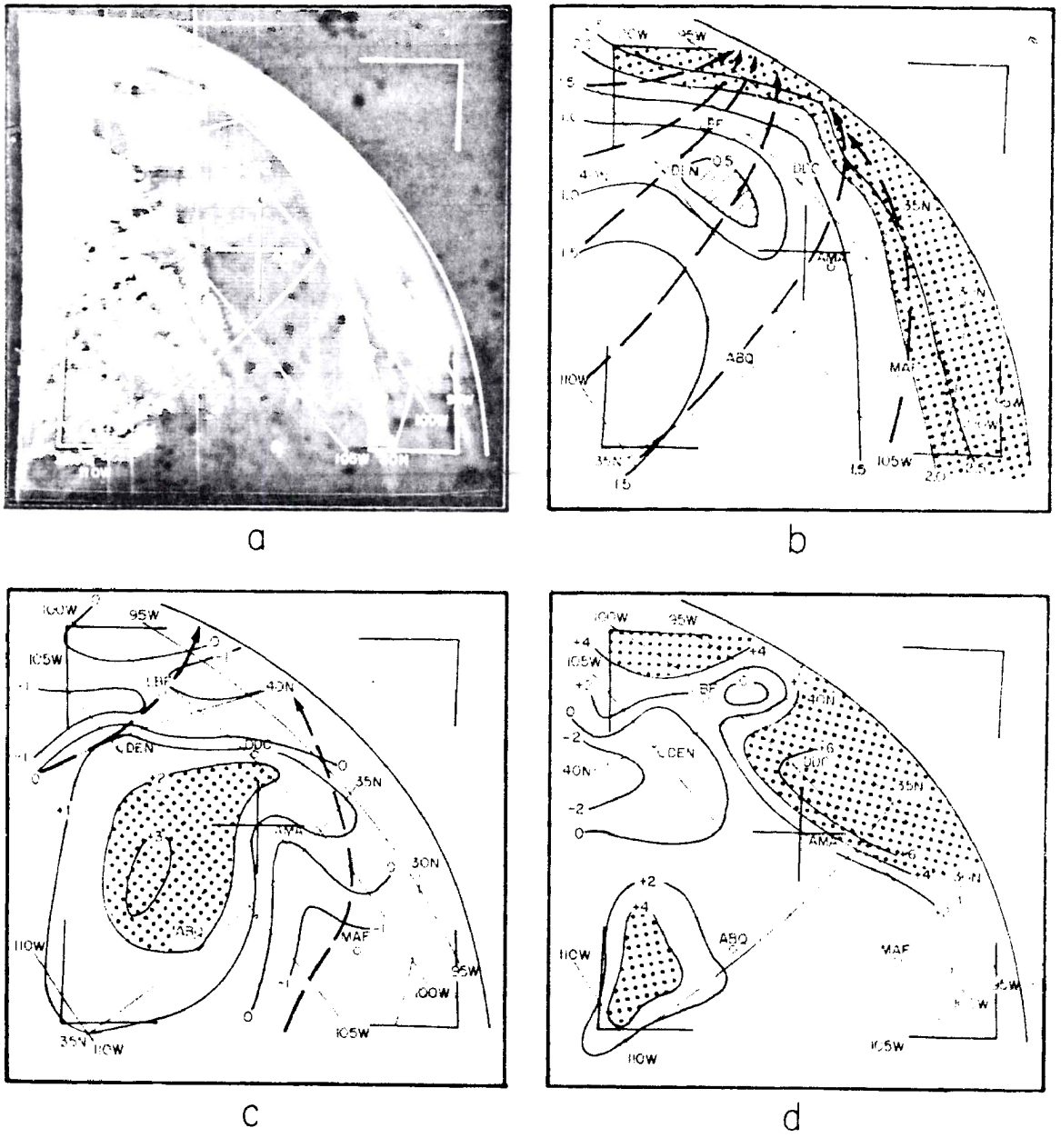

Figure 36. (a) TIROS V orbit 4349 T frame 14 valid at 1955 GMT, 18 April 1963. (b) 700 mb mixing ratio (w, g/kg, solid lines) superimposed on rectified TIROS grid. Dotted area shows w > 2.0 g/kg, cross hatched area shows w < 0.5 g/kg. Dashed arrows are 700 mb streamlines. (c) 700 mb mass divergence (10^{-5}/sec, solid lines). Dotted area shows divergence > 2 x 10^{-5}/sec, cross hatched area shows convergence < -2 x 10^{-5}/sec. Dashed line is core of maximum 700 mb wind. (d) 700 mb divergence of moisture flux (10^{-8}/sec). Dotted area shows divergence > 4 x 10^{-8}/sec, cross hatched area shows convergence < -4 x 10^{-8}/sec. Charts b, c, and d are valid at 0000 GMT, 19 April 1963.

streaky appearance of the clouds in the east-west direction and the broad bands in the north-south direction support the hypothesis that the bright areas over the mountains were orographically produced clouds. This picture was used earlier to identify the wall cloud formation, a definite orographic effect, which appears north of Denver, Colorado (DEN). The field of mixing ratio (see Figure 36 b) shows the drier air mass behind the cold front which had just passed over the mountains and into the Great Plains region. The concentration of moisture had been shifted eastward and was associated with the cloudy area along the front. Streamlines, also shown in Figure 36 b, indicate that the flow was normal to the mountains from 35° N latitude northward to the top of the picture. This orientation of mountains and streamlines would provide the necessary lifting to produce clouds in the drier air over the higher terrain. Figure 36 c again shows the strong divergence area at 700 mb straddling the Continental Divide south of Denver, Colorado (DEN). This divergence and the downslope motion over the Great Plains were responsible for the clear area between the eastern slope of the mountains and the front. Just north of 40° N latitude in southern Wyoming and Nebraska there was a weak band of convergence. The moisture flux pattern (Figure 36 d) also shows convergence south of North Platte, Nebraska (LBF), while the TIROS picture indicates clouds in the same area. Earlier in this paper and in a previous report (Reiter, 1965 a), it was pointed out that this area of clouds was possibly associated with inertia gravity waves induced by the mountains northwest of Denver, Colorado (DEN). The pattern of moisture flux gives a good definition of the horizontal extent of this wave cloud since the convergence of moisture flux is directly associated with the vertical motions in the wave.

The last TIROS picture (see Figure 37) which pertained to this case covered the northwestern United States. The bright patterns in this picture were rather disorganized and are probably a combination of snow cover, orographically induced clouds, and condensation produced by large scale dynamic lifting. The field of mixing ratio (see Figure 37 b) indicates that there was enough moisture present for cloudiness over most of the region, with the exception of a relatively dry tongue which extended from Lander,

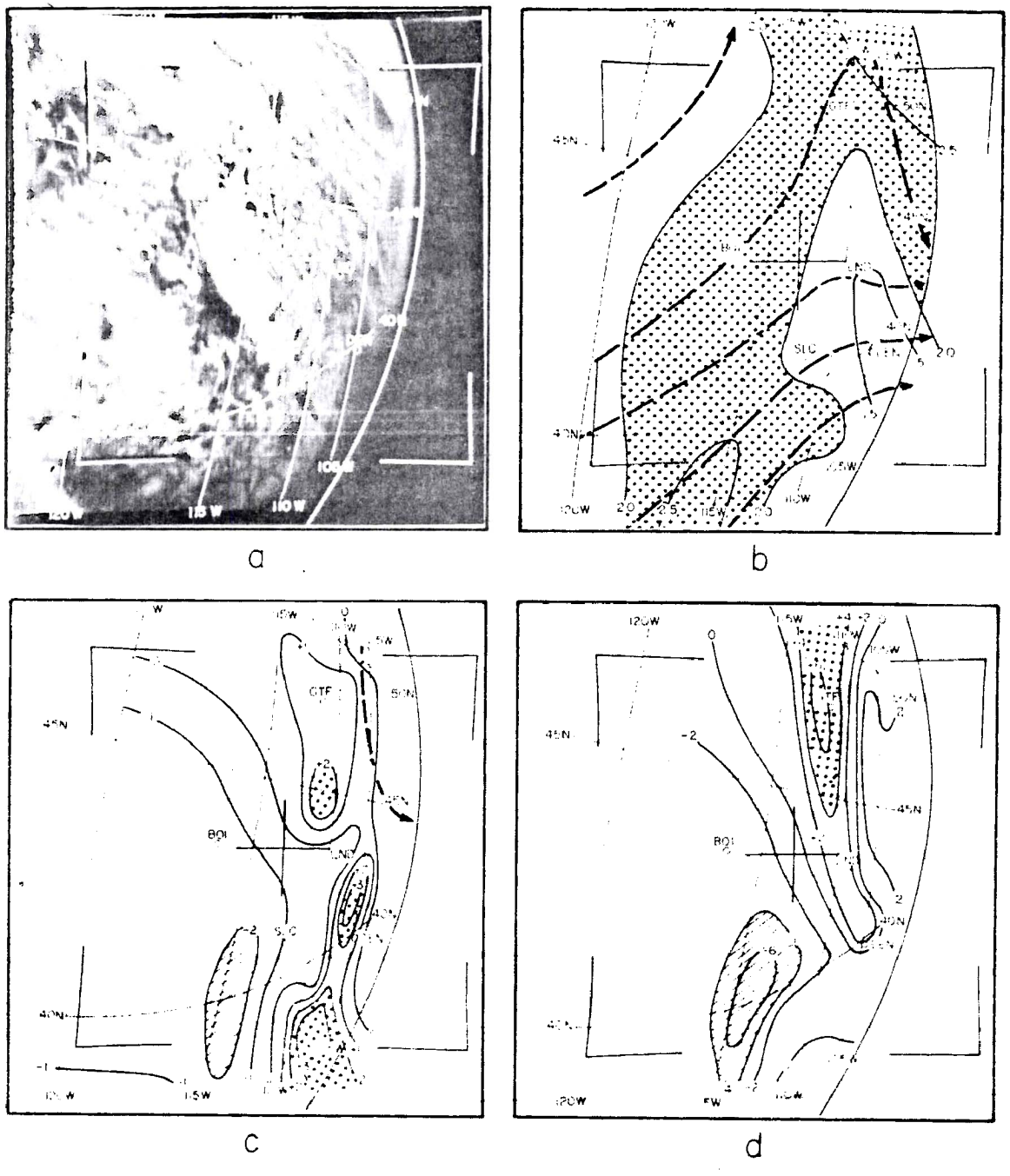

Figure 37. (a) TIROS V orbit 4363 D frame 28 valid at 2105 GMT, 19 April 1963. (b) 700 mb mixing ratio (w, g/kg, solid lines) superimposed on rectified TIROS grid. Dotted area shows w > 2.0 g/kg, dashed arrows are 700 mb streamlines. (c) 700 mb mass divergence (10^{-5}/sec, solid lines). Dotted area shows divergence > 2 x 10^{-5}/sec, cross hatched area shows convergence < -2 x 10^{-5}/sec. Dashed line is core of maximum 700 mb wind. (d) 700 mb divergence of moisture flux (10^{-8}/sec). Dotted area shows divergence > 4 x 10^{-8}/sec, cross hatched area shows convergence < -4 x 10^{-8}/sec. Charts b, c, and d are valid at 1200 GMT, 19 April 1963.

Wyoming (LND), southeastward to Denver, Colorado (DEN). The TIROS patterns show a clear area in this region; however, this part of the picture was very near the horizon where resolution is poor. The field of 700 mb $\nabla_h \cdot \vec{V}$ (see Figure 37 c) also supports the possibility of cloud formation since there was convergence over most of the picture area with the exception of divergence centers over Montana and southeastern Wyoming, both near the horizon and badly distorted. The moisture flux does not disagree with the patterns discussed above, nor does it significantly add information on a cloud producing mechanism to explain the distribution in this picture.

CHAPTER IV

SUMMARY

Scorer and Klieforth's suggestion that chinook winds can be caused by the blocking of low level inversion layers and by large amplitude lee waves appears to be valid for chinooks of the Rocky Mountains. The cases studied in this paper strongly suggest that the criteria of $\pi/\ell \leq$ mountain height is a necessary, but not a sufficient, condition for chinooks of the subsidence type.

It would seem, from the cases studied, that diurnal changes in lapse rate to the windward side of the mountains exert a strong influence on the onset and cessation of chinooks. The April 1963 case exemplified this diurnal control. Lag time between the proper conditions in the windward surface layer and the onset of chinooks on the leeward side correspond well with the time necessary for a parcel of air to traverse this distance. The only diurnal effect which can be noted during the December 1964 case is the larger dew point spread caused by higher afternoon temperatures on the leeward side of the mountain. These higher temperatures are also effective in increasing the surface wind speeds due to turbulent exchange of momentum from aloft.

The processes responsible for the second and third types of chinooks described in Chapter I are independent of the windward inversion and would not be controlled by the π/ℓ criteria. Nocturnal chinook winds can be associated with a subsidence type foehn and are, therefore, indirectly influenced by Scorer and Klieforth's hypothesis.

The winds associated with the April case do not follow the classic pattern normally attributed to chinooks. Referring to Figure 9, it will be noted that the strong surface winds are not coincidental with

the onset of the chinook. It is generally thought that the warm temperatures and associated drop in dew point are caused by strong downslope winds. While it is certainly true that these anomalies are caused by downslope flow, it does not follow that the leeside winds must be strong. Postulating a more likely sequence of events, the chinook begins with light downslope winds which cause the surface temperature to increase until a dry-adiabatic lapse rate is reached or exceeded. These lapse rate conditions allow turbulence and mixing through a deep layer of the atmosphere, transporting momentum of stronger winds aloft downward. This momentum transport continues to strengthen the surface winds, while exerting a damping influence on maximum surface temperatures, until the generating forces on the windward side of the mountain are negated by a wind shift or by the removal of the windward surface inversion.

The flow pattern aloft during the April case was dominated by a strong southwesterly jet stream. Low level wind maxima detected at the 700 mb surface were undoubtedly part of the mechanism which produced the chinook conditions and strong surface winds on the Great Plains.

Details shown on TIROS pictures during the first chinook can be correlated with the wind field and derived quantities. The analysis of 700 mb mass divergence and moisture flux is in good agreement with cloud areas seen by TIROS.

BIBLIOGRAPHY

Ashwell, I. Y. (1964) Meteorological work at the University of Alberta, Calgary: Weather, vol. 19, p. 55.

Bolin, B. (1950) On the influence of the earth's orography on the general character of the westerlies, Tellus, vol. 2, pp. 184 - 195.

_____, (ed.) (1959) The Atmosphere and the Sea in Motion (Rossby Memorial Volume). Rockefeller Institute Press in association with Oxford University Press, New York, 509 pp.

Burman, E. A. (1958) On a theory of anticyclonic foehns: Akademia Nauk SSSR, Bulletin of the Academy of Science USSR Geophysics Series, No. 3, 1958, pp. 235 - 237.

Cook, A. W. and A. G. Topil (1952) Some examples of chinooks east of the mountains in Colorado: Bulletin of the American Meteorological Society, vol. 33, pp. 42 - 47.

Corby, G. A. and C. E. Wallington (1956) Airflow over mountains: the lee wave amplitude: Quarterly Journal of the Royal Meteorological Society, vol. 82, pp. 266 - 274.

Cressman, G. P. (1960) Improved terrain effects in barotropic forecasts: Monthly Weather Review, vol. 88, pp. 327 - 342.

Danielsen, E. F. (1961) Trajectories: isobaric, isentropic and actual: Journal of Meteorology, vol. 18, pp. 479 - 486.

Glenn, C. L. (1961) The chinook: Weatherwise, vol. 14, pp. 175 - 182.

Godske, C. L. et al. (1957) Dynamic Meteorology and Weather Forecasting, American Meteorological Society and Carnegie Institution, Boston and Washington, 800 pp.

Gutmann, L. N. and D. I. Tebuev (1961) Contribution to the theory of a foehn: Akademia Nauk SSSR, Bulletin of the Academy of Science USSR Geophysics Series, No. 1, 1963, pp. 786 - 789.

Haltiner, G. J. and F. L. Martin (1957) Dynamical and Physical Meteorology, McGraw-Hill Book Co., Inc., New York, 470 pp.

Hann, J. (1903) Handbook of Climatology, translated by R. de C. Ward, The Macmillan Co., London, 437 pp.

Hazen, H. A. (1888) Chinook winds: Monthly Weather Review, vol. 16, p. 19.

Ives, R. L. (1950) Frequency and physical effects of chinook winds in the Colorado high plains region: Annals of the Association of American Geographers, vol. 40, pp. 293 - 327.

Johnson, H. N. (1936) The dry chinook wind: American Meteorological Society, Bulletin, vol. 17, pp. 23 - 27.

Lockwood, J. G. (1962) Occurrence of foehn winds in the British Isles: The Meteorological Magazine, vol. 91, pp. 57 - 65.

Long, R. R. (1955) Some aspects of the flow of stratified fluids. III. Continuous density gradients: Tellus, vol. 7, pp. 342 - 357.

McClain, P. E. (1952) Synoptic investigation of a typical chinook situation in Montana: Bulletin of the American Meteorological Society, vol. 33, pp. 87 - 94.

_____, (1959) Some effects of the Western Cordillera of North America on cyclonic activity: Journal of Meteorology, vol. 17, pp. 104 - 115.

Mintz, Y. (1958) Design of some numerical general circulation experiments: The Bulletin of the Research Council of Israel, vol. 7G, pp. 67 - 113.

Panofsky, H. (1958) Introduction to Dynamic Meteorology, Pennsylvania State University, University Park, Pennsylvania, 243 pp.

Petterssen, S. (1956) Weather Analysis and Forecasting, 2nd ed., McGraw-Hill Book Company, Inc., New York, 2 vols.

Queney, P. (1947) Theory of perturbations in stratified currents with applications to air flow over mountain barriers: Department of Meteorology of the University of Chicago, Miscellaneous Reports No. 23, University of Chicago Press, Chicago, 81 pp.

Reiter, E. R. (1958) Klima von Inssbruck 1931 - 55, Stadtmagistrat Innsbruck, Statislisches Amt, p. 61.

Reiter, E. R., et al. (1965 a) Effect of large mountain ranges on atmospheric flow patterns as seen from TIROS satellites: WISP Project Report No. 2, Colorado State University, Technical Paper No. 69, 110 pp.

_____, (1965 b) The behavior of jet streams in potential fallout situations: Progress Report No. 2, Further Studies on Radioactive Fallout, Colorado State University, Technical Paper No. 70, pp. 111 - 115.

Scorer, R. S. (1949) Theory of waves in the lee of mountains: Quarterly Journal of the Royal Meteorological Society, vol. 75, pp. 41 - 56.

_____, (1955) Theory of non-horizontal adiabatic flow in the atmosphere: Quarterly Journal of the Royal Meteorological Society, vol. 81, pp. 551 - 560.

_____, (1958) Airflow over mountains: Indeterminacy of solution: Quarterly Journal of the Royal Meteorological Society, vol. 84, pp. 182 - 183.

_____, and H. Klieforth (1959) Theory of mountain waves of large amplitude: Quarterly Journal of the Royal Meteorological Society, vol. 85, pp. 131 - 143.

Sergius, A., G. R. Ellis, and R. M. Ogden (1962) The Santa Ana winds of southern California: Weatherwise, vol. 15, pp. 102 - 105.

Thomas, T. M. (1963) Some observations on the chinook "arch" in western Alberta and northwestern Montana: Weather, vol. 18, pp. 166 - 170.

APPENDIX A

DEVELOPMENT OF COMPUTER PROGRAM TO CALCULATE VORTICITY, DIVERGENCE, AND DIVERGENCE OF MOISTURE FLUX

by
W. D. Ehrman

Vorticity, divergence, and divergence of moisture flux were calculated by an IBM 1620 computer using data taken from analyses of isotachs, streamlines, and mixing ratio. A grid with 2.5 degree latitude increments along the y axis and 2.5 degree longitude increments along the x axis was designed for the calculations. (For a more complete description of the grid, see Text.)

The equations used were:

A) Relative vorticity -

$$\vec{k} \cdot (\nabla \times \vec{V}) = \frac{\partial v}{\partial x} - \frac{\partial u}{\partial y} \cong \frac{\Delta v}{\Delta x} - \frac{\Delta u}{\Delta y}$$

where $\vec{k} \cdot (\nabla \times \vec{V})$ is the relative vorticity,

$\vec{V}$ is the observed velocity,

$\vec{k}$ is the vertical unit vector,

u and v are zonal and meridional components of observed wind velocity,

and x and y are Cartesian coordinates with x positive to the east and y positive to the north.

B) Absolute vorticity -

$$\vec{k} \cdot (\nabla \times \vec{V}) + f = \frac{\partial v}{\partial x} - \frac{\partial u}{\partial y} + f \cong \frac{\Delta v}{\Delta x} - \frac{\Delta u}{\Delta y} + 2\Omega \sin\phi$$

where $\vec{k} \cdot (\nabla \times \vec{V}) + f$ is the absolute vorticity,

f is the Coriolus parameter,

Ω is the angular velocity of the earth,

and ϕ is latitude.

C) Divergence -

$$\nabla_h \cdot \vec{V} = \frac{\partial u}{\partial x} + \frac{\partial v}{\partial y} \cong \frac{\Delta u}{\Delta x} + \frac{\Delta v}{\Delta y}$$

where $\nabla_h \cdot \vec{V}$ is the horizontal divergence,

and ∇_h is the horizontal Del operator.

D) Divergence of moisture flux -

$$\nabla_h \cdot q\vec{V} = \frac{\partial (qu)}{\partial x} + \frac{\partial (qv)}{\partial y} \cong \frac{\Delta (qu)}{\Delta x} + \frac{\Delta (qv)}{\Delta y}$$

where $\nabla_h \cdot q\vec{V}$ is the horizontal divergence of moisture flux,

and q is the mixing ratio.

Figure 1 depicts an area subdivision of the main grid. The velocity values at original points A , B , C , and D were converted to u and v components. Values of u , v , and q at grid points North, South, East, and West were then linearly interpolated from the original grid points (A , B , C , and D). Using these new values, vorticity, divergence, and divergence of moisture flux were computed for the center point "0".

The Δy increment varied by less than one per cent over the entire grid; therefore, a mean value of Δy was used. The Δx increment varied by 25 per cent making it necessary to calculate each longitude (Δx) increment by hand before reading them into the program.

A symbol correspondence table, flow chart, and program listing appear at the end of this Appendix.

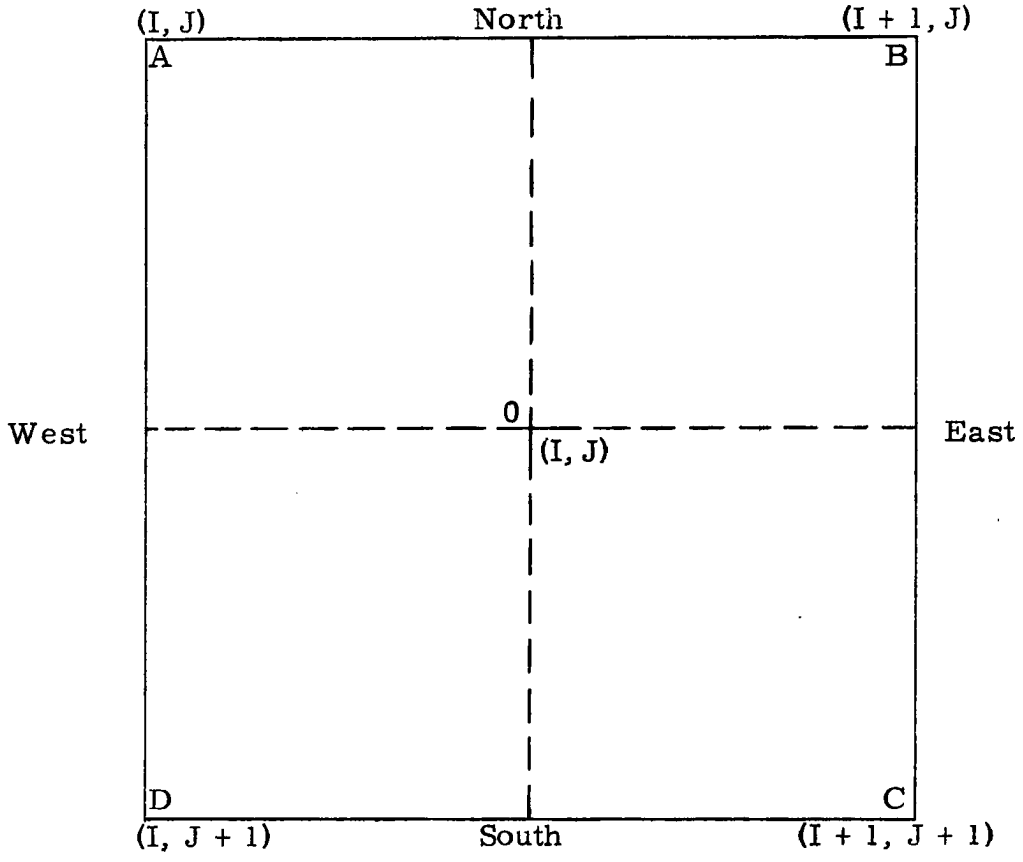

Figure 1: Points A , B , C , and D are the original points from velocity and mixing ratio analyses. The subscripts refer to these points as they are noted in the program listed at the end of this Appendix. North, South, East, and West refer to linearly interpolated points. The center point, "0", is the location of the final computed value (of vorticity, etc.).

SYMBOL CORRESPONDENCE TABLE

TEXT	PROGRAM	DESCRIPTION AND UNITS
-----	IP	Pressure level (mb)
-----	IDA	Day
t	ITM	Time
-----	FF	Wind Velocity (meters/sec)
-----	DO	Wind Direction
w	Q	Mixing ratio (g/kg)
dx	DX	Longitude increment along a latitude circle (meters)
dy	DY	Latitude increment along a meridian (meters)
u	U	Zonal component of wind (meters/sec)
v	V	Meridional component of wind (meters/sec)
-----	ALAT	Latitude of center point of grid
q	VORT	Relative vorticity ($\times 10^{-4}$/sec)
Q	AVORT	Absolute vorticity ($\times 10^{-4}$/sec)
D	DIV	Divergence ($\times 10^{-5}$/sec)
w	Q	Moisture flux ($\times 10^{-8}$/sec)

The following symbols, when added to a previously defined symbol indicate:

EST, WST, NOR, SOU, = Interpolated value at (east, west, north, south) point of intermediate grid. (See Figure 1.)

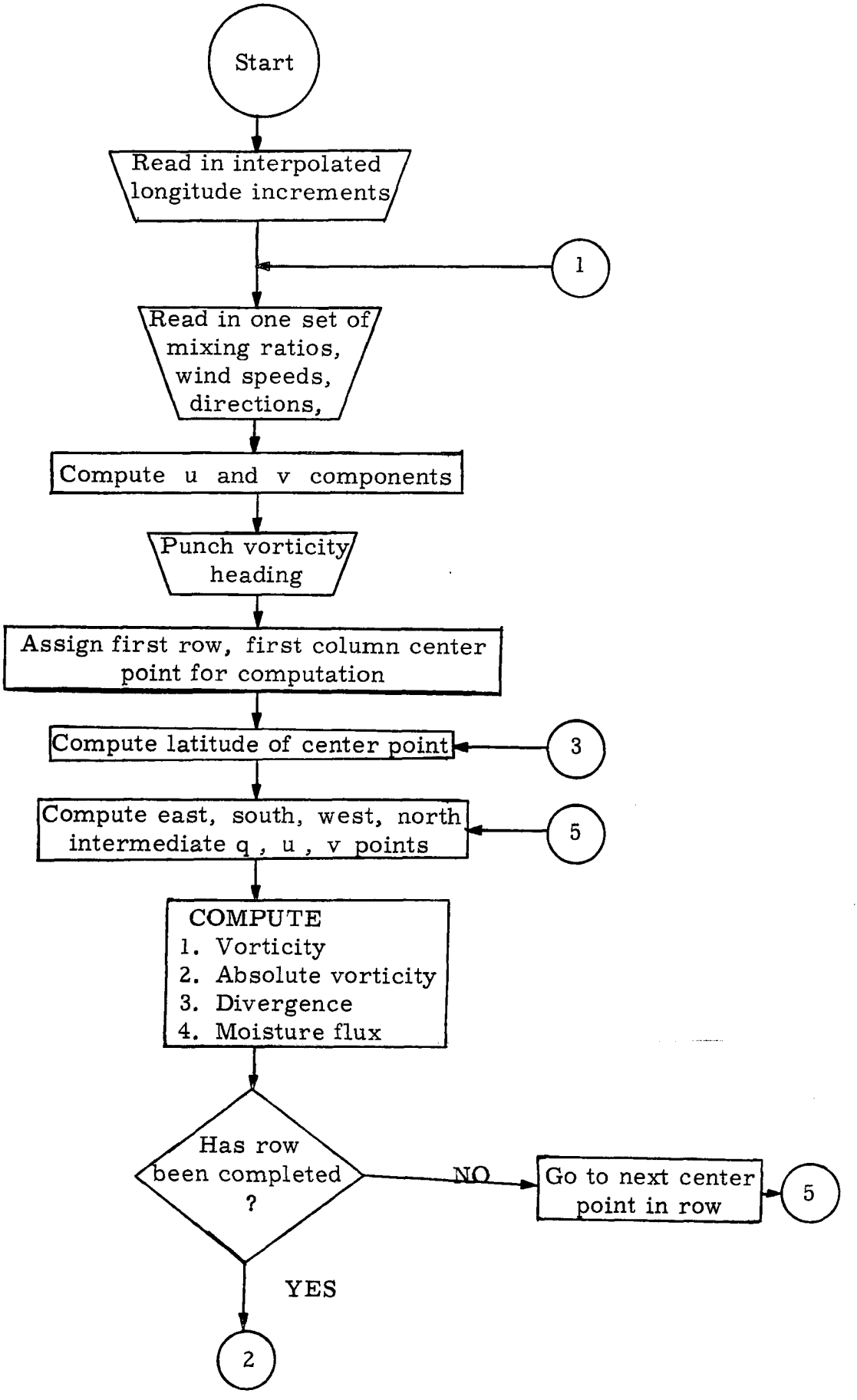
Start
Read in interpolated longitude increments
1
Read in one set of mixing ratios, wind speeds, directions,
Compute u and v components
Punch vorticity heading
Assign first row, first column center point for computation
Compute latitude of center point
3
Compute east, south, west, north intermediate q , u , v points
5
COMPUTE
1. Vorticity
2. Absolute vorticity
3. Divergence
4. Moisture flux
Has row been completed ?
NO
Go to next center point in row
5
YES
2

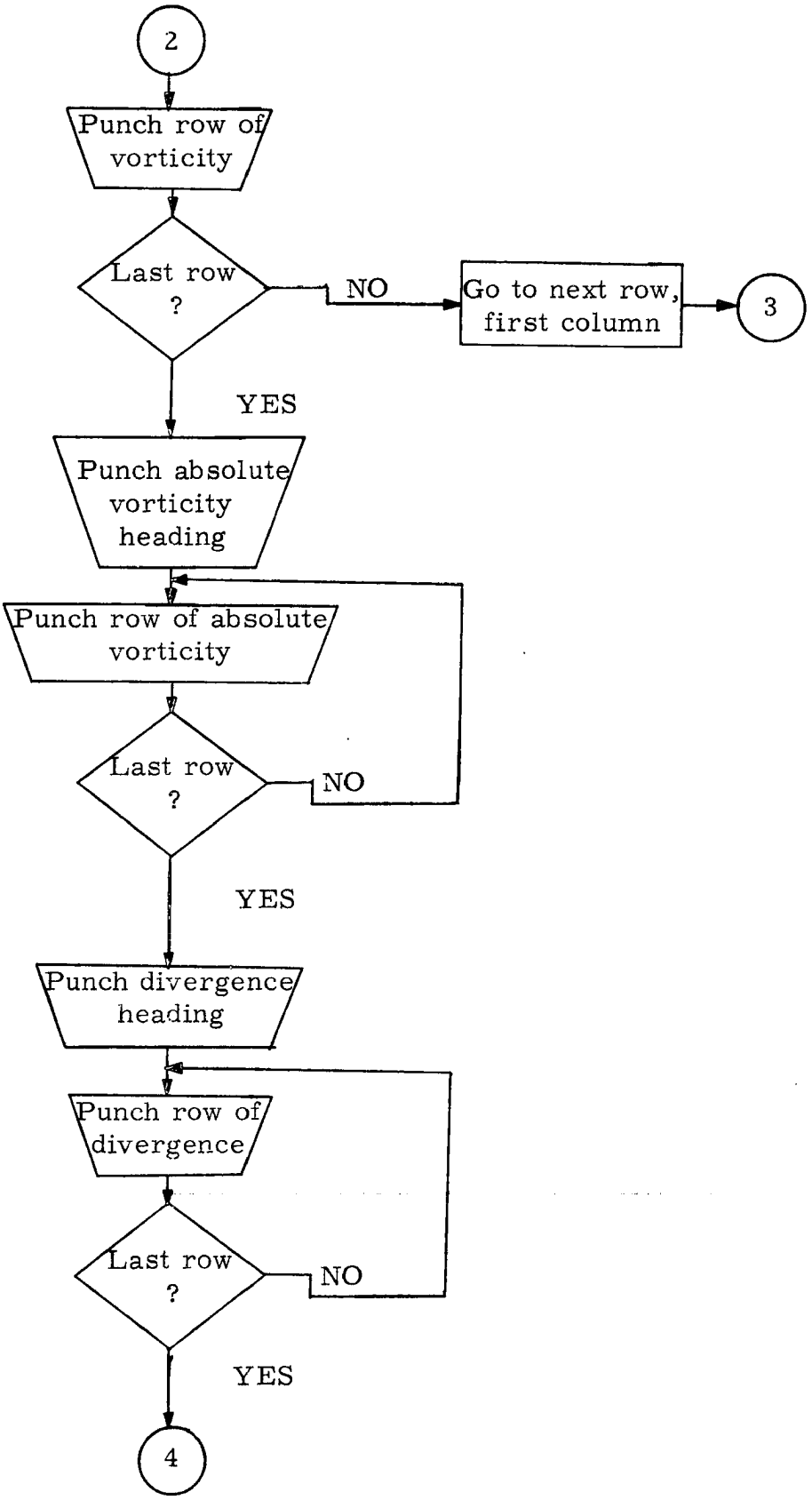
2
Punch row of vorticity
Last row ?
NO
Go to next row, first column
3
YES
Punch absolute vorticity heading
Punch row of absolute vorticity
Last row ?
NO
YES
Punch divergence heading
Punch row of divergence
Last row ?
NO
YES
4

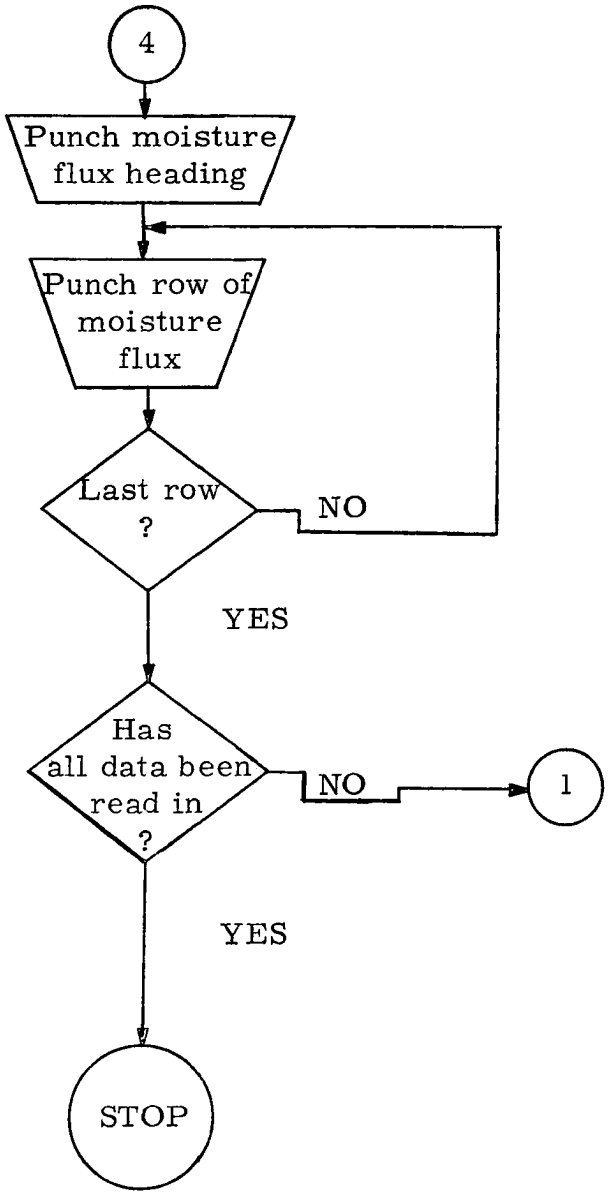
4
Punch moisture flux heading
Punch row of moisture flux
Last row ?
NO
YES
Has all data been read in ?
NO
1
YES
STOP

```
C       PROGRAM COMPUTE DEL (CROSS V, DOT V, DOT V*Q)
        DIMENSION DD(9,8),FF(9,8),U(9,8),V(9,8),VORT(8,7),AVORT(8,7),DIV(8
       1,7),DX(7),Q(9,8),QFLX(8,7)
C       THIS PROGRAM COMPUTES, USING FINITE DIFFERENCING TECHNIQUES, THE
C       DIVERGENCE (DU/DX+DV/DY), THE RELATIVE VORTICITY (DV/DX-DU/DY),
C       THE ABSOLUTE VORTICITY (DV/DX-DU/DY+CORIOLUS FORCE), AND THE
C       DIVERGENCE OF MOISTURE FLUX (DQU/DX+DQV/DY).
C       READ IN INTERPOLATED LONGITUDE  INCREMENTS IN METERS
  100 READ 101,(DX(I),I=1,7)
  101 FORMAT (7(F6.0,1X) )
    3 DO 10 I=1,9
C       READ IN WIND VELOCITY, DIRECTION, AND MIXING RATIOS FOR ONE TIME
C       AND PRESSURE LEVEL
        READ 5,IP,IDA,ITM,(FF(I,J),DD(I,J),Q(I,J),J=1,8)
C       I SUBSCRIPT REFERS TO + X DIRECTION, J SUBSCRIPT TO - Y DIRECTION
    5 FORMAT (3I2,2X,8(F2.0,F3.0,F2.1,1X))
        DO 10 J=1,8
C       COMPUTE U AND V COMPONENTS
        U(I,J)=-FF(I,J)*SINF(DD(I,J)/57.2958)
        V(I,J)=-FF(I,J)*COSF(DD(I,J)/57.2958)
   10 CONTINUE
        DY=111043.*2.5
        IP=10*IP
        PUNCH 15,IP,IDA,ITM
   15 FORMAT (8HPRESSURE,3X,I3,5X,3HDAY,3X,I2,5X,4HTIME,3X,I2,5X,18HRELA
      1TIVE VORTICITY)
        PUNCH 20
   20 FORMAT (8X,1H1,8X,1H2,8X,1H3,8X,1H4,8X,1H5,8X,1H6,8X,1H7,8X,1H8)
        DO 50 J=1,7
        AJ=J-1
C       COMPUTE LATITUDE OF CENTER POINT, AND Q,U, AND V MEANS FOR
C       PERIPHERAL POINTS
        ALAT=((46.75-AJ*2.5)/57.2958)
        DO 30 I=1,8
        VEST=(V(I+1,J)+V(I+1,J+1))/2.
        VWST=(V(I,J)+V(I,J+1))/2.
        VNOR=(V(I,J)+V(I+1,J))/2.
        VSOU=(V(I,J+1)+V(I+1,J+1))/2.
        UEST=(U(I+1,J)+U(I+1,J+1))/2.
        UWST=(U(I,J)+U(I,J+1))/2.
        UNOR=(U(I,J(+U(I+1,J))/2.
        USOU=(U(I,J+1)+U(I+1,J+1))/2.
        QEST=(Q(I+1,J)+Q(I+1,J+1))/2.
        QWST=(Q(I,J)+Q(I,J+1))/2.
        QNOR=(Q(I,J)+Q(I+1,J))/2.
        QSOU=(Q(I,J+1)+Q(I+1,J+1))/2.
C       COMPUTE VORTICITY, ABSOLUTE VORTICITY, DIVERGENCE, AND MOISTURE
C       FLUX FOR CENTER POINT
        VORT(I,J)=((VEST-VWST)/DX(J)-(UNOR)-USOU)/DY)*10000.
        AVORT(I,J)=VORT(I,J)+14.58*SINF(ALAT) *.1
        DIV(I,J)=((UEST-UWST)/DX(J)+(VNOR-VSOU)/DY)*100000.
   30 QFLX(I,J)=((QEST*UEST-QWST*UWST)/DX(J)+(QNOR*VNOR-QSOU*VSOU)/DY)*
      1100000.
        JJ=J
C       OUTPUT OF VORTICITY (*10.**-4.)
   33 PUNCH 35,JJ,(VORT(I,J),I=1,8)
```

```
   35 FORMAT (I1,2X,8F9.5)
   50 CONTINUE
      PUNCH 55, IP,IDA,ITM
   55 FORMAT (8HPRESSURE,3X,I3,5X,3HDAY,3X,I2,5X,4HTIME,3X,I2,5X,18HABSO
     1LUTE VORTICITY)
      PUNCH 20
      DO 65 J=1,7
      JJ=J
C     OUTPUT OF ABSOLUTE VORTICITY (*10.**-4.)
   65 PUNCH 35, JJ,(AVORT(I,J),I=1,8)
      PUNCH 70, IP,IDA,ITM
   70 FORMAT (8HPRESSURE,3X,I3,5X,3HDAY,3X,I2,5X,4HTIME,3X,I2,5X,10HDIVE
     1RGENCE
      PUNCH 20
      DO 80 J=1,7
      JJ=J
C     OUTPUT OF DIVERGENCE (*10.**-5.)
   80 PUNCH 35,JJ,(DIV(I,J),I=1,8)
      PUNCH 120, IP,IDA,ITM
  120 FORMAT (8HPRESSURE,3X,I3,5X,3HDAY,3X,I2,5X,4HTIME,3X,I2,5X,13HMOIS
     1TURE FLUX)
      PUNCH 20
      DO 130 J=1,7
      JJ=J
C     OUTPUT OF MOISTURE FLUX (*10.**-8)
  130 PUNCH 35,JJ,(QFLX(I,J),I=1,8)
C     CONTINUE TO NEXT SET OF DATA
      GO TO 3
      END
```